POLITECNICO DI MILANO

School of Industrial and Information Engineering

Department of Energy

Master of Science in Nuclear Engineering

Compact laser-driven neutron sources: a theoretical investigation

Advisor:
Prof. Matteo Passoni
Co-Advisor:
Ing. Arianna Formenti

Graduation Thesis of:
Francesca Arioli
872800

Academic Year 2017-2018

Contents

List of Figures

List of Tables

Abstract

This thesis reports on a theoretical investigation aimed at assessing the degree of reliability of methods for the simulation of laser-driven neutron sources. More precisely, neutron generation in a pitcher-catcher scheme is considered. The theoretical tools available for the study of such systems include analytical and numerical methods. As regards these latter, the dynamics of ion acceleration and the neutron generation processes are modelled, respectively, by means of the particle-in-cell code *Piccante* and of the Monte-Carlo-based *Geant4* toolkit. By properly combining the two above-mentioned codes, it is possible to obtain a comprehensive numerical tool able to perform multi-physics simulations of the whole system. Simulations are supported by analytical methods, which are employed for making simple estimates. After having ascertained, by means of a benchmark against experimental data suitably chosen from the literature, the possibility and the limits of the employment of theoretical methods, these have been used for the study of systems of actual interest,i.e. compact laser-driven neutron sources. This activity implied the necessity to introduce optimized features inside the system, especially concerning the pitcher and catcher architecture.

Sommario

Questo lavoro di tesi riporta un'indagine teorica volta ad appurare il grado di affidabilità di metodi per la simulazione di sorgenti di neutroni da laser. Più precisamente, viene considerata la generazione di neutroni per mezzo di uno schema *pitcher-catcher*. Gli strumenti teorici disponibili per lo studio di questi sistemi includono metodi analitici e numerici. Con riferimento a questi ultimi, la dinamica dell'accelerazione di ioni e il processo di generazione dei neutroni vengono modellati facendo uso, rispettivamente, del codice particle-in-cell *piccante* e del toolkit *Geant4*, basato sul metodo Monte Carlo. Combinando opportunamente tra loro i codici sopra citati, è possibile ottenere uno strumento numerico complessivo in grado di eseguire simulazioni dell'intero sistema. A questo strumento si affiancano metodi analitici, per stime semplificate di grandezze caratteristiche. Dopo aver accertato, mediante un benchmark con dati sperimentali opportunamente selezionati, la possibilità e i limiti nell'utilizzo di metodi teorici, questi sono stati impiegati per lo studio di sistemi di attuale interesse, ossia le sorgenti di neutroni da laser compatte. Ciò ha comportato la necessità di introdurre elementi di ottimizzazione nel sistema, in particolare per quanto riguarda il design del pitcher e del catcher.

Estratto

Questo lavoro di tesi si colloca nell'ambito degli studi teorici sulle sorgenti di neutroni da laser. In questi sistemi lo schema di produzione dei neutroni è generalmente il seguente: un laser super-intenso illumina un bersaglio solido sottile (detto *pitcher*) spesso pochi μ, ionizzandolo completamente e rendendolo un plasma; Parte degli ioni presenti come contaminanti atmosferici sulla superficie posteriore del bersaglio vengono accelerati fuori dallo stesso in seguito all'interazione con l'impulso laser; Gli ioni così prodotti vengono fatti incidere su un convertitore (detto *catcher*), dove reazioni nucleari indotte dagli ioni producono neutroni. Lo schema appena menzionato è detto "pitcher-catcher" ed è quello a cui ci si riferirà nel resto della trattazione.

Per impulsi laser super-intensi si intendono impulsi in grado di somministrare al bersaglio una intensità I>10^{18}W/cm^2. Se si considera che già a partire da intensità di 4 ordini di grandezza inferiori qualunque materiale viene ionizzato in pochi cicli di laser, è chiaro che nel regime super-intenso l'interazione tra impulso laser e materia è un'interazione tra impulso laser e plasma. Per raggiungere di valori di intensità così elevati, due strade sono percorribili con la tecnologia attuale:

- L'impiego di laser con potenza dell'ordine del PW. Questi sistemi sono in grado di somministrare al bersaglio impulsi ultra-brevi (centinaia di fs - 1ps) con energie dell'ordine delle centinaia di J. Data la potenza elevata richiesta ad ogni sparo, questi sistemi non possono operare a una frequenza maggiore di qualche sparo al giorno;
- L'impiego di laser con potenza dell'ordine dei TW, fino a un massimo di poche centinaia di TW. Questi sistemi laser somministrano al target una quantità molto minore di energia rispetto al caso precedente (qualche J). Tuttavia, valori elevati di intensità sono raggiunti impiegando impulsi

ultra-brevi (fino a poche centinaia di fs, in base alla tecnologia utilizzata) e ultra-focalizzati su regioni di diametro 10-100μm. La potenza minore richiesta ad ogni sparo, fa sì che questa classe di laser possa operare a una frequenza ben maggiore rispetto al caso precedente (da 0.1Hz a 1-2kHz).

La creazione di un plasma è necessaria per l'accelerazione di ioni: infatti, i plasmi sono in grado di sostenere al loro interno campi elettrici dell'ordine di qualche TW/m, che consentono l'accelerazione di ioni su scale spaziali dell'ordine del μm. Più precisamente, a seguito dell'interazione con l'impulso laser, una frazione degli elettroni presenti sullo strato frontale del target viene fortemente accelerata in avanti, riuscendo così ad attraversare il bersaglio creando una nuvola elettronica che si estende fuori dalla superficie posteriore del target. La separazione di carica sussistente tra la nube elettronica e gli ioni positivi all'interno del target è all'origine dei campi longitudinali estremamente intensi sopra menzionati. Gli ioni che vengono accelerati con maggior facilità sono quelli con un basso rapporto q/m, ossia i protoni. Il meccanismo descritto è chiamato TNSA (Target Normal Sheath Acceleration) e lo spettro risultante di ioni ha un andamento caratteristico approssimabile come un'esponenziale decrescente fino a una certa energia di cutoff.

Nell'ambito della produzione di neutroni a energie moderate (massimo 20-30 MeV), l'interesse per le sorgenti di neutroni basate su impulsi laser è legato a più fattori.
Innanzitutto questi sistemi hanno un elevato potenziale in termini di compattezza. Infatti, estendendosi il campo accelerante su scale di lunghezza dell'ordine del μm, di fatto la dimensione del sistema è determinata dalla dimensione del laser impiegato. Attualmente un laser compatto di potenza 10 TW occupa lo spazio di una stanza. Se, come è lecito aspettarsi, l'ulteriore sviluppo della tecnologia comportasse una diminuzione delle dimensioni dei sistemi laser impiegati, ci si avvicinerebbe alla realizzazione di una sorgente di neutroni portabile, il cui potenziale in termini di numero di utilizzatori sarebbe notevole.
Altri fattori che rendono le sorgenti di neutroni da laser potenzialmente vantaggiose rispetto alle CANS sono: una minore estensione spaziale del bunch (1cm alla sorgente) e un minore spread temporale (da decine di fs a qualche ns). Queste caratteristiche, insieme all'elevata direzionalità che caratterizza i neutroni prodotti da reazioni (p,n) e (d,n) su materiali leggeri come litio e berillio, costituiscono un vantaggio in vista dello sfruttamento d queste sorgenti per applicazioni. Attualmente sorgenti compatte di neutroni da laser sono in grado di produrre 10^{5-7}n/s, valore appena sufficiente per realizzare una radiografia

neutronica.

Avendo delineato i potenziali vantaggi derivanti dall'impiego di sorgenti compatte di neutroni da laser, è chiaro l'interesse nell'ottimizzare la performance di questi sistemi, al fine di realizzare sorgenti effettivamente impiegabili in applicazioni. Per fare ciò è importante disporre di strumenti teorici adatti alla simulazione dei sistemi in esame. Pertanto, lo scopo della mia tesi è quello di appurare il grado di affidabilità di strumenti analitici e numerici per la simulazione di sorgenti di neutroni da laser in uno scenario pitcher-catcher. Più precisamente, i codici numerici impiegati nelle simulazioni sono il codice particle-in-cell (PIC) *Piccante* per la simulazione dell'interazione laser-plasma e il toolkit Monte Carlo *Geant4* per lo studio della generazione di neutroni. Questi due strumenti sono stati integrati al fine di ottenere uno strumento numerico in grado di eseguire simulazioni multi-fisica, ossia di simulare in tutti i suoi aspetti il comportamento di una sorgente di neutroni da laser. Per quanto riguarda invece gli strumenti analitici, questi sono impiegati per fare stime semplificate di quantità caratteristiche del sistema.

Al fine di appurare l'affidabilità dei metodi teorici descritti per la simulazione di sorgenti di neutroni da laser, un benchmark è stato effettuato rispetto a dati sperimentali selezionati dalla letteratura. Nella definizione dei criteri per la scelta dei dati, attenzione è stata posta nella definizione di criteri per la scelta di dati sperimentali che tenessero conto dei vincoli imposti su certe quantità del sistema dall'architettura degli strumenti numerici impiegati.

I metodi analitici individuati si sono rivelati affidabili per la simulazione dei sistemi in esame solo parzialmente. Da un lato, alcune caratteristiche legate alla fisica dell'interazione laser-plasma e della generazione di neutroni sono catturate bene dalle simulazioni. Ad esempio, il metodo PIC riproduce bene la forma esponenziale degli ioni accelerati con TNSA, mentre il metodo Monte Carlo e i metodi analitici riproducono bene il cutoff maggiore dell'energia dei neutroni prodotti. Dall'altro lato tuttavia, alcune serie criticità sono emerse durante lo studio.

Innanzitutto, la letteratura riguardante esperimenti di generazione di neutroni da laser non è ricca. Questo fattore, combinato con i vincoli dettati dal costo computazionale delle simulazioni PIC sul range ammissibile di alcuni parametri operativi, ha fatto sì che non fosse possibile realizzare questa parte del benchmark. Tuttavia, una versione analitica dello spettro sperimentale degli ioni è stata usata come input della simulazione Monte Carlo, al fine di fare un confronto su quella parte.

In seconda istanza, è stata rilevata una scarsa disponibilità di valori sperimentali

di sezioni d'urto per le reazioni (p,n) e (d,n) nel range di energie considerato (da 0 a circa 30 MeV). Il fatto che Geant4 utilizzi dati sperimentali di sezioni d'urto solo per isotopi specifici e in range di energia non ampi è sicuramente una sorgente di discrepanza tra i dati ottenuti sperimentalmente e quelli ottenuti dalle simulazioni. Questo problema affligge anche i metodi analitici, in cui le sezioni d'urto sono impiegate per stime della resa di reazione o per ricavare spettri caratteristici dei neutroni prodotti.

L'ultima parte del lavoro ha riguardato la simulazione di scenari di sorgente compatta di neutroni da laser ottimizzata, basata su uno schema pitcher-catcher. Lo studio è stato condotto utilizzando simulazioni multi-fisica, ossia impiegando lo spettro ionico prodotto dal codice PIC come input per la simulazione Monte Carlo. Come accennato in precedenza, in vista dell'impiego in applicazioni reali, per le sorgenti di neutroni compatte un aumento del flusso neutronico sarebbe cruciale. Tuttavia, non potendo aumentare eccessivamente la potenza rilasciata sul target dal laser per rispettare il vincolo di compattezza della sorgente, un'ottimizzazione dell'intero processo di generazione neutronica risulta non solo benefico, ma necessario. Per le simulazioni sono stati impiegati due tipi di laser: un laser table-top da 20TW e un laser più voluminoso potente, ma comunque compatto, da 74TW.
Per ogni scenario simulato si sono ottimizzate le performance sia del pitcher che quelle del catcher. In particolare, per il primo si è impiegato un target nanostrutturato costituito da una foam di carbonio ottimizzata in densità e spessore depositata su un sottile substrato metallico. Quando irraggiata con il laser, la foam viene ionizzata e un plasma con densità elettronica circa uguale alla densità critica viene formato. In questo regime una maggior frazione dell'energia del laser viene trasmessa al target, conducendo a un incremento nella massima energia degli ioni. Il catcher invece, risulta ottimizzato dal punto di vista del materiale e dello spessore.
Il passaggio da un laser table-top a quello compatto comporta un aumento di circa un ordine di grandezza nell'emissione angolare dei neutroni nella direzione perpendicolare al target, che passa da 10^5 a 10^6n/sr. Questi valori sono in linea con i dati riportati in letteratura per dati di questo tipo.

Introduction

Already prior to the invention of laser technology in 1960, it was known that a charged particle belonging to a plasma can be accelerated by very strong electric fields (TV/m) developing over a scale of a few μm inside the plasma, following the interaction with a very intense electric field. More precisely, a super-intense laser pulse is required to obtain ion acceleration. When a super-intense and ultra-short laser pulse impiges onto a target, it rapidly ionizes matter, turning it into a plasma. Such pulses could not be obtained until 1985, when a technique called *Chirped Pulse Amplification (CPA)* was introduced [18].
Currently, super-intense laser pulses can reach intensities of the order of 10^{22} W/cm^2, which can be obtained using two different approaches. One possibility is to employ PW-class lasers pulses, which deliver an energy of some hundreds of J on the target within a time of hundreds of fs - 1 ps. On the other hand, more compact lasers of a few hundreds of TW in power, delivering only a few J on the target can be used. The high intensity is obtained focusing the pulse on very small areas (of diameter 10-100 μm) for very short times (up to hundreds of fs, depending on the laser technology). The most widely used laser technology for laser-driven ion acceleration is currently Titanium:Sapphire, due to its capability of generating ultra-short pulses (tens of fs).

Laser-driven neutron sources are systems for neutron production based on laser-induced ion acceleration. In such systems a super-intense laser pulse is delivered on a thin solid target (called *pitcher*), from which ions are accelerated. These latter are subsequently made to impinge on a converter target (called *catcher*), in which ion-induced nuclear reactions lead to neutron production. This setup for neutron production is called *pitcher-catcher* scheme. Another possibility is the so-called *bulk* scheme, in which laser-driven deuterons are accelerated onto a deuterated target, where d(D,T)p fusion reactions take place.
Laser-driven neutron sources show numerous advantages over accelerator-based

systems. In the first place they can provide shorter neutron bunch in space (∼1cm at the source) and time (some tens of fs to some ns), along with larger repetition rates (up to the order of the kHz). Secondly, the generated bunch of neutrons is characterized by high peak intensity and directionality: this is of great advantage for applications.

Recently, particular attention has been devoted to the theoretical and experimental study of neutrons generated with compact systems employing TW-class lasers. These systems are small in size: for powers of a few tens of TW they take up the space of one room. Among compact laser-driven neutron sources, neutron-generating systems employing table-top lasers would enlarge the number of users, besides representing a step towards the source portability.

The goal of this thesis is the assessment of the reliability of theoretical methods to simulate a laser-driven neutron source in a pitcher-catcher scenario. These include both analytical and numerical methods. Among the latter, "multi-physics simulations" combining particle-in-cell (PIC) methods for the simulation of laser-target interaction and Monte Carlo approaches for the study of ion-neutron conversion, have been adopted. More precisely, the codes employed in the two cases are, respectively, *piccante* and *Geant4*.

The thesis is organized as follows.

- Chapter 1 -*Neutrons: properties, applications and conventional sources*- presents an overview of some selected applications of neutrons, which are ore of potential interest for compact laser-driven neutron sources. Furthermore, a description of currently available neutron sources will is given.

- Chapter 2 -*Laser-driven neutron sources*- deals with the description of the characteristics and working principles of laser-driven neutron sources. In particular, the physics lying under the processes of laser-target interaction, ion acceleration and ion-neutron conversion are discussed. Also, the use of a carbon nanostructured foam in a bilayer target is presented as a possible scheme for performance enhancement. Following, the state of the art in the field of laser-driven neutron sources is presented. At the end of the chapter the motivations and goals of this thesis work are presented.

- Chapter 3 -*Theoretical tools for the simulation of laser-driven neutron sources*- is devoted to the description of theoretical methods suitable for the description of a laser-driven neutron source. These include analytical and numerical methods. Among these latter, an extensive description of the particle-in-cell and of the Monte Carlo approach is given, with specific

reference to their integration in laser-driven neutron sources simulations. In order to test the reliability of the previously discussed theoretical tools in simulating the systems under study, the need of a benchmark against experimental data taken from the literature emerges. Therefore, a set of selection criteria for the choice of experimental data are presented and discussed at the end of the chapter.

- Chapter 4 -*Benchmarking the codes against experimental data of laser-driven neutrons*- deals with the description of the benchmarking activity mentioned above. Firstly, the chosen experimental data are presented in detail. Then, a comparison between experimental results and theoretical predictions, obtained using the methods described in chapter 3 is illustrated, with particular attention to the issues that had to be addressed in order to perform theoretical estimates. Finally, the sensitivity of the results to parameters such as the converter material and thickness will be discussed.

- Chapter 5 -*Simulation of a compact laser-driven neutron source*- is devoted to the design and theoretical investigation of optimized compact laser-driven neutron sources based on a pitcher-catcher scheme. Firstly, the concept of compact laser-driven neutron source is specified, also with reference to the physical characteristics of compact accelerator-based sources. Secondly, the possible strategies for laser-driven sources optimization are analysed and implemented in four different schemes of optimized compact source. These scenarios are investigated theoretically using realistic laser parameters. The performance of such systems is tested using itegrated PIC and Monte Carlo simulations.

- Chapter 6 -*Conclusion and perspectives*- includes the overall reults of this thesis work, along with considerations about the further development in this field.

Chapter 1

Neutrons: properties, applications and conventional sources

Due to their peculiar properties, neutrons are widely employed in science and technology. For instance, only a few years after their discovery in 1932, neutrons started to be used by physicists to probe other nuclei or to produce fission chain reactions, paving the way for the civil exploitation of nuclear energy. Throughout the years neutrons have been employed in applications concerning health, energy production, imaging technology and many others. Naturally, this keen interest in neutrons has fostered over time the research of more and more well-performing neutron sources.
In this chapter all the aforementioned aspects will be treated. In particular in section 1.1 the main physical features of the neutrons will be presented, while sections 1.2 and 1.3 will be respectively devoted to the description of selected applications and to the currently available neutron sources.

1.1 Main neutron properties

The neutron, together with the proton, is one of the constituents of the atomic nuclei. In particular, since protons and neutrons behave similarly within the nucleus and they have similar masses, they are both referred to as *nucleons*.

Being slightly heavier than a proton, a free neutron is not stable, but it decays according to a β^- scheme showing a mean lifetime of 881.5s= 14.7min:

$$n \rightarrow p + e^- + \bar{\nu}_e \tag{1.1}$$

where p indicates a proton, e^- an electron and $\bar{\nu}_e$ an electronic antineutrino.
A neutron is not an elementary particle since it shows an internal structure made of quarks. In particular, the neutron is composed of one up quark (charge $+2/3$ e) and two down quarks (charge $-1/3$ e). This is the reason why the neutron is a particle with zero net electric charge, zero electrical dipole moment and zero electrical polarizability. Notice that experiments for testing the neutron electrical properties keep being performed. Therefore, the measured values for these quantities are not exactly zero, but correspond to the experimental lower limits. Its quark structure makes the neutron a member of the family of the *hadrons* and, more precisely, of that of *baryons*.
Furthermore, the quarks explain the magnetic behaviour and the spin possessed by the neutron. In fact, despite having zero net electric charge, the neutron is affected by magnetic fields. This is due to the neutron's non-zero magnetic moment, which can be modeled as a sum of the magnetic moments of the constituent quarks [19]. The value of the neutron's magnetic moment was first measured at Berkeley in 1940, by Luis Alvarez and Felix Bloch.
With regard to the spin number, the neutron has a spin of 1/2, which makes the neutron a fermion.
A summary of the physical properties of neutrons is given in table 1.1.
Neutrons are generally categorized according to their energy. A complete classification can be found in table 1.2.

Table 1.1: *Main properties of neutrons.*

Mass	m_n = 1.009u = 1.675×10^{-27}Kg
Composition	Quarks: 1 up, 2 down
Mean lifetime	881.5 s
Spin	1/2
Magnetic moment	μ = -1.913 μ_n[1] = -0.966×10^{-26} J/T

[1]The script μ_n indicates the nuclear magneton.

Table 1.2: *Neutron classification according to their energy.*

Cold neutrons	$E < 0.025eV$
Thermal neutrons	$E = 0.025eV$
Epithermal neutrons	$0.025eV < E < 1000eV$
Fast neutrons	$E > 1000eV$

The neutron was discovered as such by James Chadwick in 1932 at the Cavendish Laboratory in Cambridge. However, the idea of a neutral particle was conceived a long time before [20].
In 1920 Rutherford suggested that the nucleus consisted not only of protons, but also of neutral particles, which were assumed to be constituted by a proton and an electron bound together in some way [21]. It was Rutherford to choose the name *neutron* for the newly envisaged particle. A development in research occurred in 1931, when Walther Bothe and Herbert Becker discovered that α particles emitted by polonium produced a highly penetrating radiation when impinging on a light material target such as beryllium, boron, or lithium. Since the radiation was not affected by electric fields, it was assumed to be γ radiation. However, in 1932 Irène Curie and Frédéric Joliot showed that paraffin or any compound containing hydrogen emitted highly energetic protons if irradiated with the unknown radiation. After performing experiments, Chadwick concluded that the new radiation consisted of neutral particles with about the same mass as the proton. These particles are the neutrons. For this discovery Chadwick was awarded the Nobel Prize in physics in 1935.

1.2 Selected applications

Due to the absence of electric charge, neutrons interact with matter in a highly different way if compared to charged particles or electromagnetic radiation. More precisely, since neutrons do not feel the Coulomb force, they can interact with matter only by means of nuclear and magnetic scattering or inducing nuclear reactions. This results in an enhanced penetration of neutrons in matter with respect to charged particles, even when moving through high-Z solid materials [22].
These unique interaction properties make neutrons interesting for applications

covering a wide range of topics, such as nuclear science and technology [23], medicine [24], biology [25], geology [26], materials science [27] and archeology [28]. The main features of neutrons requested for some applications are summarized in table 1.3).

In this section a set of selected applications will be illustrated in detail. More

Table 1.3: *Selected features of some applications of neutrons.*

Name			**Reaction**	**Requested flux [n/cm^{2}s]**	**Energy of neutrons**
Materials analysis	Diffraction		n scattering	10^{7-8}	Thermal
	NAA	TNAA ENAA FNAA	(n,γ)	10^{9-10}	Thermal Epithermal Fast
	SEE testing[2]		none	10^{5-6}	Fast
Imaging	Thermal n radiography		n transmission	10^{6-7}	Thermal
	Fast n radiography		n transmission	10^{5-6}	Fast
	API		$T(d,n)^4He$	10^8 n/s	Fast
ANI[3]			$(n,f)^4$ or (γ,f)	10^{3-5}	Fast
BNCT[5]			$^{10}B(n,\alpha)^7Li$	10^{13} cm^{-2}	Epithermal

precisely, the attention will be drawn on those fields in which compact and economical sources providing neutrons of modest energy but in number sufficient for applications are required. In this framework, laser-driven neutron sources represent a promising alternative to current technology for neutron production.

1.2.1 Neutron-based materials analysis techniques

This family of neutron applications encompasses many different techniques aimed at material investigation. Although all these methods involve the bombardment

[2]SEE = Single Event Effects. The aim here is to induce defect in the sample under examination, not to induce a specific reaction in it. Also, the reported flux is meant as a commonly used minimum flux. An incresed flux (up to 10^{7-9} n/cm^2s would lead to faster testing time. For further explanation see section 1.2.1 and reference [29].

[3]Active Neutron Interrogation

[4]f = fission.

[5]In the case of BNCT what matters is the delivered therapeutic dose, which should be equal to 20Gy. The epithermal fluence value reported is related to the concentrations of the boron loaded pharmaceutical which can be obtained nowadays. For further explanation see [24].

of a sample with neutrons of proper energy, a first distinction can be made between *destructive* and *non-destructive* techniques. While the former involve damage and therefore unserviceability of the sample for further operation, the latter enable material testing without inducing defects in the analysed structure. This is an indispensable requirement when tests are performed on objects belonging to the cultural heritage or on installed structural components.

Destructive neutron-based techniques are widely used in the study of radiation-induced damage of materials, especially those involved in the design of fission and fusion reactors [30, 31].
Another field of application of these techniques is the investigation of *single event effects (SEE)* in electronic devices [29]. A single event occurs when a single energetic particle (a neutron in this case) strikes sensitive regions of an electronic device disrupting its normal function. This phenomenon is significant at high altitudes (e.g. at the cruising altitude of planes), being due to cosmic particles colliding with atoms in the atmosphere and creating cascades or showers of neutrons and protons.

On the other hand, non-destructive techniques for the analysis of materials can be categorized into different groups according to the employed analytical principle: neutron scattering or absorption.
Neutron scattering is at the basis of neutron diffraction, a technique enabling the determination of the detailed structures of atomic and molecular organization inside the sample along with the detection of mechanical stresses present in it [32]. Conversely, absorption techniques are based on the so-called "neutron-in-gamma-out" reactions, in which characteristic γ radiation is emitted by the de-excitation of nuclides activated by neutrons. Some among the numerous existing absorption techniques will be discussed in the following paragraph.

Neutron activation analysis (NAA)

Neutron activation analysis (NAA) is a nuclear technique for the bulk elemental analysis of elements in a large number of materials. The underlying physical mechanism is the following. When a neutron of a certain energy impinges on a nucleus of the sample material it is absorbed, transforming the target nuclide in a radioactive isotope, i.e. *activating* it. When the activated nuclide decays, it emits characteristic γ radiation, which can be detected and traced back to the nature of the emitting species. In this way it is possible to determine the sample elemental composition, from major components down to substances present

only in traces. Indeed, NAA is the most sensitive analytical tools for elemental analysis: detection limits of the order of $10^{-14}g$ can be reached [33]. Owing to this peculiarity NAA is a useful tool in those fields in which trace element analyses play a key role, such as doped-semiconductor technology, chemistry and mineralogy.

The general scheme for NAA involves the exposure of the sample to an intense neutron flux for a well defined time period. The quantitative determination of the elemental composition of the sample is performed as follows. Imagine to irradiate a sample containing N nuclei of the element under study with a neutron flux ϕ. Then the rate of accumulation of activated nuclides is given by:

$$\frac{dN^*}{dt} = N\sigma\phi - \lambda N^* - N^*\sigma^*\phi \tag{1.2}$$

where N^* is the number of activated nuclei produced at time t, σ is the neutron capture cross section of the considered element, λ is the decay frequency of the activated nuclide and σ^* is its total removal cross section. After an irradiation time T, the induced activity decreases with time as:

$$A(t) = N\sigma\phi(1 - e^{-\lambda T})e^{-\lambda t} \tag{1.3}$$

Clearly, the parameter T must be appropriately chosen. In general it never exceeds a few weeks or one month, also due to practical reasons. [33]
Neutron sources employed for NAA must provide fluxes larger than 10^9 n/cm^{2}s. Fission reactor are commonly employed, but also radioisotope-based sources or neutrons from nuclear reactions induced by accelerated particles can be used.
In this context it should be pointed out that the energy spectrum of neutrons in the radiation field of a reactor is not homogeneous in space. This implies that the output of NAA is dependent on the position of sample irradiation. For this reason NAA measurements are always performed irradiating the sample together with a standard sample of known composition. The two are irradiated under the same conditions and the produced γ rays are measured by the same device, therefore ensuring equal detection efficiency. Knowing that irradiation induces the same specific activity in the two samples, the unknown mass of a certain element m_x can be calculated as:

$$m_x = \frac{A_x}{A_s} m_s \tag{1.4}$$

where A_x and A_s are the activities measured in the sample and in the standard respectively, while m_s is the mass of the element present in the standard. If

γ-rays from more than one element are detected - which is often the case - the different photon energies can be resolved making use of a sodium-iodide scintillator (NaI(Tl)) or of a high-purity germanium (HPGE) semiconductor detector and employing γ spectroscopy techniques.
Besides its high sensitivity, NAA can be advantageous with respect to other techniques for numerous reasons. In the first place the signal measured in NAA depends only on the presence of radioactive nuclides so, at least in principle, it is matrix-independent. This implies that matrix preparation can be kept simple and that treatment of the sample after irradiation (e.g. chemical separation) is possible. Secondly, NAA is insensitive to light elements such as H, C, N, O, which makes them ideal constituents for matrices. Finally, since characteristic γ rays penetrate deeply through matter, also samples with extended geometry can be tested.

NAA is generally performed using thermal neutrons. However, it can be convenient to employ fast neutrons either when thermal neutrons induce only weak activation in the elements of interest (this is the case of elements such as H, C, N and O) or, conversely, when the sample is too highly activated by thermal neutrons [33].
The variation of NAA employing neutrons of the order of MeV is called *Fast Neutron Activation Analysis (FNAA)* and is a complementary technique to standard NAA [34]. Since the light elements detected by FNAA are also the main constituents of explosives and narcotic substances, this technique seems promising for homeland security applications (see section 1.2 for further details).
A further variation of NAA involves epithermal neutrons and is therefore indicated as ENAA. This technique employs neutrons with energies in the range $\sim$eV - 1 MeV for the analysis of samples which cannot be analysed otherwise because of the predominant activation of ^{24}Na. This is the case of some biological or sea water samples [35].
The neutron activation techniques mentioned until now belong to the group of the so-called *Delayed Gamma Neutron Activation Analysis (DGNAA)*, which means that activity measurements are performed only once the irradiation process has terminated. An alternative to this exists and is called *Prompt Gamma Neutron Activation Analysis (PGNAA)*. The technique involves activity measurements during irradiation. These are necessary when the sample contains isotopes with high neutron capture cross sections (e.g. B, Cd, Gd, Sm) or which decay too rapidly to be measured by DGNAA. PGNAA is used also when nuclear species leading to weak γ-ray intensities are present in the sample. One of the current fields of application of PGNAA is nuclear waste analysis [36].

1.2.2 Neutron-based imaging techniques

Neutron imaging techniques are methods employing neutrons as a probe for obtaining images of concealed objects. In general, these methods rely on the detection, downstream of the sample, of radiation containing the "signature" of its constituents. In particular, many neutron-based imaging methods exist, whose names vary according to the energy of the employed neutrons and to the exploited physical phenomenon. The most widely used techniques are *transmission neutron radiography* and *Associated Particle Imaging (API)*, whose main characteristics will be outlined in the following.

In transmission-based neutron radiography, neutrons passing through the object interact with the nuclei, leading to an attenuation of the beam, which is registered by a proper detector. In particular, neutron radiography exploits the scattering or absorption contrast between different elements to give information about the material under investigation.
What makes neutron-based techniques interesting is their complementarity to X-ray imaging. Indeed, X-rays attenuation depends on the material density and grows with it; conversely, the attenuation of neutrons is related to their interaction with the sample nuclei i.e., ultimately, to the material cross section for neutron interaction. The utterly different behaviour of the two probes results in the fact that, when investigating a sample, some features that are easily detected by neutrons could appear invisible to X-rays and viceversa. This can be easily seen in Fig. 1.1, in which the scans of an airfreight container obtained using γ-rays alone and in combination with neutrons are displayed. As a general rule, X-rays are more suitable for the imaging of high Z structures, while the efficacy of a neutron radiography on single elements should be evaluated from case to case.
Neutron radiography can be performed with thermal neutrons moderated from a fission reactor. However, the interrogating power increases significantly if neutrons of higher energy are employed.
There is growing interest in neutron radiography techniques in many fields of application. For example, they can be employed to study the penetration of water and other aqueous solutions inside cracks in cementitious materials [37]. Moreover, they are useful in carrying out various metallurgical controls (e.g. the detection of hydrogenated components in metallic structures) in a non-distructive manner [38].

Another common method for performing neutron-based imaging is API,

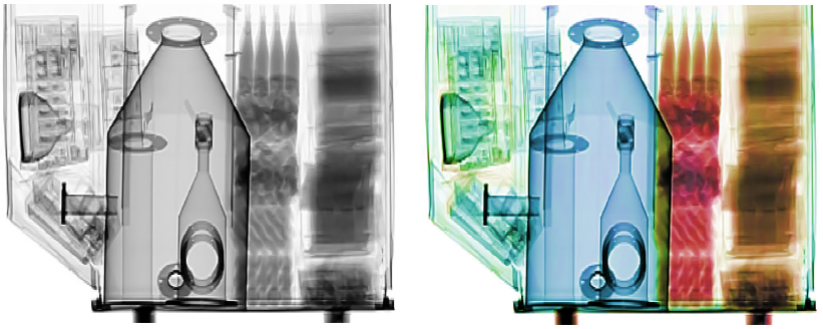

Figure 1.1: *The left-hand image is a γ-ray scan and the right-hand image is a combined neutron and γ scan of an airfreight container. The colour variations indicate different materials: from left-to-right the module contains assorted computer equipment, heavy steel industrial items, mixed boxes of food and boxes containing office files and papers. From [1]*

.

which is a three-dimensional imaging technique using fast neutrons. API is based on space and time correlation between the 14 MeV neutron and the associated α particle produced by the T(d,n)^{4}He reaction in a small accelerator or in a *sealed-tube neutron generator (STNG)*.[6] Indeed, the direction and time of emission of a single neutron are related to those of the α particle, which is detected with a position-sensitive detector. When the neutron interacts with the sample nuclei it produces characteristic γ radiation, whose energy and time of arrival on the detector are used to locate the neutron-nucleus interaction and to determine the target species present in the interaction position. The outcoming image is a 3D elemental map of the sample with high signal-to-noise ratio [2,5].

1.2.3 Security applications: detection of special nuclear material and illicit substances

Some of the above-mentioned techniques are employed in the framework of homeland security. Possible applications include the detection of illicit substances in transit areas for people and goods such as customs, seaports and airports. The hunted-for substances include explosives and drugs, as well as

[6] For further explanations see section 1.3.4.

smuggled *Special Nuclear Material*. This latter category includes fissile materials, which are subject to nuclear safeguards and, therefore, to material accountancy. Security applications for the detection of these two classes of materials will be extensively discussed in the following sections.

Non-intrusive neutron-based techniques for detection of illicit substances

Over the last decades there has been growing interest in non-intrusive detection of hidden explosives and illicit drugs, especially in airline luggage, small mail items and large cargo containers [39]. What makes neutrons the probe of election for application in this field is their differential sensitivity to the main constituents of explosive and narcotic substances, i.e hydrogen, carbon, nitrogen and oxygen. In particular, illicit materials are detected by measuring the ratio between a couple of the above-mentioned elements and comparing it to the known values for a list of substances (see Fig.1.2). An overview of the most diffused techniques for security matters are summarised in table 1.4.

Table 1.4: *Selected features of the main nuclear physics-based techniques for the non-intrusive interrogation of bulk samples. From [2].*

Technique	Radiation source	Probing radiation	Main reaction type	Detected radiation
TNA	^{252}Cf, STNG	Thermal neutrons	(n,γ)	Prompt γ-rays from neutron capture
FNA	STNG	Fast neutrons	$(n,n'\gamma)$	γ-rays from inelastic n scattering
PFNA	ns-pulsed accelerator	Fast neutrons	$(n,n'\gamma)$	γ-rays from inelastic n scattering
PFNTS	ns-pulsed accelerator	Broad spectrum of fast neutrons	All available	Source neutrons which are transmitted
API	Associated particle STNG	14MeV neutrons with associated α particles	$(n,n'\gamma)$	γ-rays in coincidence with α-particle
PFTNA	μs-pulsed d-T STNG	Fast during pulse, then thermalized neutrons	$(n,n'\gamma)+(n,\gamma)$	γ-rays from inelastic n scattering, capture and activation analysis
FNSA	ns-pulsed, continuous accelerator, STNG	Monoenergetic fast neutrons	(n,n)+(n,n')	Elastically and inelastically scattered neutrons

The first method employed for security controls has been *Thermal neutron analysis (TNA)*, which consists in measuring the prompt γ-rays emitted by the sample nuclei after irradiation with thermal neutrons. Within this technique,

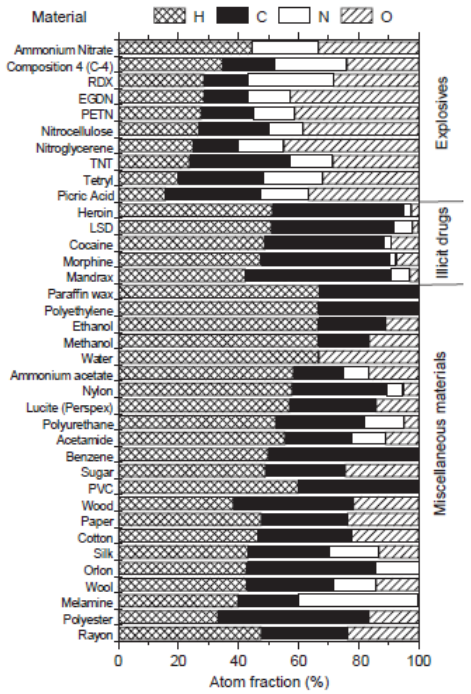

Figure 1.2: *Atomic fractions of the elements H, C, N and O, which constitute a selection of explosives, illicit drugs and miscellaneous everyday materials. From [2].*

the discovery of explosives is primarily based on the identification of nitrogen and hydrogen via the detection of ^{1}H and ^{14}N.
Fast neutron analysis (FNA) operates in an analogous manner, employing fast neutrons as a probe. Illicit substances are discovered by detecting ^{12}C, ^{14}N and^{16}O [40]. Even though fast neutrons are much less attenuated in the sample with respect to thermal neutrons, FNA imaging remains limited to smaller objects due the fact that spatial correlation between the interaction point inside the sample and the detection position must be preserved.
This limitation, together with the high background due to activation of the apparatus' structural materials, was overcome making use of pulsed-neutrons analyses including neutron time-of-flight techniques. Within these methods, a particle accelerator coupled to a lithium or beryllium target is used to accel-

erate ions, which impinge on the target generating neutrons via (p,n) or (d,n) reactions. The exact position of the interaction point inside the sample can be determined by measuring the time between neutron generation within the target and detection of the characteristic γ radiation, enabling the possibility of three-dimensional elemental imaging.
A similar result can be obtained making use of the aforementioned API technique, which allows the generation of ms-pulsed, sufficiently intense neutron beams at a smaller cost with respect to pulsed accelerator-based systems.

All these techniques have been considered as a non-intrusive method for luggage inspection [2]. This application has the most stringent requirements in terms of false negatives, which cannot be tolerated and false positives, which must be rare in order for the application to be effective and acceptable. Moreover, a short enough scanning time is necessary. In addition to this, neutron-based technologies must deal with severe safety issues related to radioprotection.
All of this considered, neutron-based screening systems seem not yet mature enough to be viable contenders for replacing X-ray technology for luggage inspection in the near future. However, some of these techniques have turned useful in other less demanding contexts, allowing a longer measuring time or a gretaer number of acceptable false positives and negatives .
This is the case of bulk air cargo scanning for fighting contraband of illicit drugs and explosives [41]. In this case scanners combine fast neutron and γ-ray radiography to provide high-resolution images of the analysed object, together with information on its elemental composition. The employed sources are: a D-T generator for neutrons and a sample of ^{60}Co for γ-rays. The measuring time is of the order of 1-2 minutes. Some of these systems are already commercially available.

Interrogation techniques for the assay of special nuclear material (SNM)

As anticipated in the introduction to this section, *special nuclear material* (henceforth referred to as SNM) includes fissile elements and compounds which are subjected to nuclear safeguards, i.e. a system of inspection and verification aimed at assuring the peaceful use of nuclear materials. These procedures were envisaged by the Nuclear non-Proliferation Treaty (NPT) and are supervised by the *International Atomic Energy Agency (IAEA)*. Among other liabilities, SNM is subject to accountancy, which is aimed at maintaining the security and

fighting against illicit trafficking.
Containers present many opportunities to hide smuggled SNM. Indeed, shielding is provided by both the material filling the container and the other containers during transportation. The commonly adopted countermeasures can rely on passive radiation detectors such as portal monitors and photon radiography, which originate an alarm if the detected activity exceeds a certain threshold. Another tool available for investigation is active interrogation, in which neutrons [42] or high-energy photons [43] are used as a probe to "interrogate" the object under examination: according to the induced "response radiation" the quantity and nature of the present fissile material can be assessed.
Both these techniques, just as all security applications, are subject to strict requirements such as a low number of both false negatives and positives, since an alarm indicating the possible presence of SNM may lead to very severe and potentially expensive responses. Furthermore, they must be characterised by a limited measuring time and be operationally safe from the point of view of radioprotection.

Neutron interrogation techniques have been developed in laboratories all over the world. In particular, at *Lawrence Livermore National Laboratories* (LLNL) in California, USA a prototype of active neutron interrogation (ANI) system has been designed and tested in the frame of the project "Nuclear Car Wash" (NCW) [44]. The idea is to interrogate a container using neutrons with energies between 3.5 and 7.0 MeV and then detect the γ-rays emitted by the β-decay of any short-lived neutron-induced fission product. The goal of this technique is to detect 5 Kg of SNM in a fully loaded container with detection probability greater than 95% and false alarm rate smaller than 0.1%, without impacting the flow of commerce and without subjecting any operator to an excessive radiation dose.
The neutrons are produced by means of the $d(D,n)^3He$ reaction employing a coupled system obtained with a radiofrequency quadrupole and a deuterium gas cell. Tests performed on static cargos and with detector arrays located in close proximity to the container lead to a positive outcome. Despite the need of further improvement and testing, these systems could start operation in the near future.
Widely employed neutron sources in this field are neutron generators (see section 1.3.4), which are devices able to produce neutrons with energies up to approximately 14 MeV.

As a last point, it should be highlighted that the presented ANI techniques

can be employed for the interrogation of fissile material in the framework of nuclear safeguards. This is proved by the fact that facilities exist, which are designed for performing both tasks. An example of such a system is the *Pulsed Neutron Interrogation Test Assembly (PUNITA)* facility located at the *Joint Research Center (JRC)* in Ispra, Varese, Italy [45].

1.3 Conventional neutron sources

Right after the discovery of the neutron by Chadwick in 1932, the only available sources were the so-called natural sources, in which neutrons are produced following a nuclear reaction induced by α particles emitted by a heavy unstable isotope. A revolution in the field occurred after the demonstration of the first self-sustained chain reaction by Fermi in 1942. After this year the development of fission reactor technology increased the availability of neutron beams.
In parallel, the technology of particle acceleration developed rapidly, leading to the creation of progressively more and more effective machines for accelerator-based neutron generation. [3].
In this section different kinds of conventional neutron sources will be examined in detail. The word *conventional* is used in opposition to *innovative* neutron sources, by which laser-driven neutron sources are intended. More specifically, radioisotope sources, research nuclear reactors, spallation sources and accelerator-driven low energy neutron sources will be discussed.
In Fig. 1.3 the development of neutron sources throughout the years is shown.

1.3.1 Radioisotope-based sources

Many of the transuranic heavy elements have an appreciable probability of spontaneous fission decay. Since in each fission event fast neutrons are released, these radioisotopes can serve as neutron sources. Obviously, these isotopes are produced encapsulated in a sufficiently thick container to avoid leakage.
The most used nuclide for this kind of sources is ^{252}Cf, which has a half life of 2.65y and emits 2.30×10^6 n/s per μg of sample. Due to its high specific activity and to encapsulation requirements, only μg of radioisotopes are present in commercially available sources.

A further scheme for neutron production based on radioisotopes involves compounds constituted by a proper radioactive species and by a light element such as beryllium or boron: the most common combinations are AmBe, PuBe

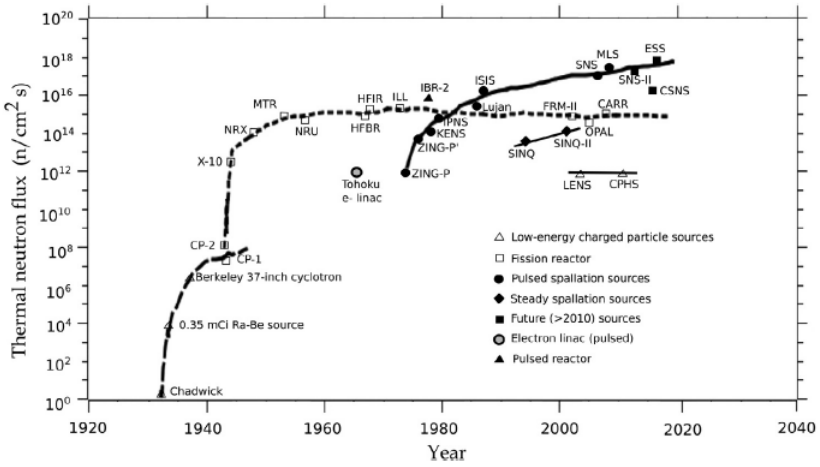

Figure 1.3: *The development of neutron sources throughout the years. From [3].*

or AmLi. In this scheme neutrons are produced by (α, n) reactions induced on the lighter species by the charged particles emitted in the decay of the heavy radioisotope.
Due to the long half-life of the radioisotope (e.g. ^{226}Ra has a half-life of 1622 years), such sources provide an almost constant flux (approximately equal to $10^5 - 10^7$ n/s [46]) of neutrons of some MeV in energy. If on one side the long life of the source is advantageous for users, on the other side, due to the large activity of the radioisotope, precautions must me taken to assure that the material remains well encapsulated. Also some radioprotection issues must be faced.
Let's consider the case of a Am-Be source: from the decay chain of ^{226}Ra, α particles with energies of about 5-8 MeV are produced, while the least bound neutron in ^{9}Be has a binding energy of 1.7 MeV. Provided that the two nuclear species are intimately mixed, when an α particle impinges on beryllium, it has a good probability of being absorbed, giving rise to the reaction $^4He(\alpha, n)^{12}C$, which has a Q-value of +5.7 MeV.
The fact that the α particles inducing the reactions do not necessarily have the same kinetic energy implies that the generated neutrons will have a continuous energy spectrum up to about 13 MeV. This is also attributable to the fact that the path of the emitted neutrons in matter before exiting the source may vary,

leading to different energy losses. Finally, when ^{12}C is produced in an excited state, the kinetic energy of the generated neutron will be lower by a quantity equal to the excitation energy of the product nucleus. The most probable neutron energy for AmBe source is ~ 5 MeV.
Due to the severe γ rays emission of ^{226}Ra, the most widely used sources are made of ^{239}Pu and ^{241}Am mixed with beryllium. The maximum neutron yield is obtained when Be is chosen as light element [46].
These sources produce approximately 10^7 n/s.

Another type of radioisotope-based sources are photoneutron sources: in this scheme neutrons are generated by (γ,n) reactions. The most widely employed reactions are $^9Be(\gamma, n)^8B$ and $^2H(\gamma, n)^1H$. Since they have a negative Q-value, γ radiation of sufficiently large energy must be used to induce the reactions.
γ radiation is usually provided by a nuclide activated in a fission reactor: the most common are ^{226}Ra, ^{124}Sb, ^{72}Ga, ^{140}La, ^{24}Na. These radioisotopes can lead to yields up to approximately 300 n/s per Ci of γ activity [46].
The advantage of this configuration is that, if the γ-rays are monoenergtic and the source is small enough to limit neutron scattering before exiting the material, the generated particles are nearly monoenergetic. The main disadvantage of photoneutron sources is that very large γ activities must be used in order to obtain a neutron flux of attractive intensity. Moreover, often the employed radioisotopes have such a short half-life that they must be reactivated between uses.

1.3.2 Research nuclear reactors

In order to achieve neutron production, fission reactor sources rely on a neutron-propagated chain reaction in the fuel (usually ^{235}U or ^{239}Pu).
One single fission events leads to a net neutron yield of about one. In addition to this, fission reactions produce two highly excited fragments with kinetic energies approximately equal to 170 MeV, which, together with the fragment excitation energy, is transformed into heat, β and γ radiation and neutrinos. Following fission, also neutrons are emitted: most of them are released promptly from the excited fission fragment nuclei (the so-called *prompt neutrons*), while a small fraction ($\sim 1\%$) emerges seconds or minutes after the fission event (*delayed neutrons*) because of the delayed decay of certain groups of fission products.
Fission reactors provide spatially homogeneous neutron fluxes of the order of 10^{13-15}n/cm^{2}s, which are continuous in time: these characteristic make nuclear reactors suitable neutron sources for applications such as NAA (see section

1.2.1). The energy spectrum of the generated neutrons is wide, ranging from fractions of eV to a few tens of MeV. However, these systems present unavoidable drawbacks such as: large costs of construction, operation and maintenance and decommissioning, complicated nuclear licensing procedures and necessity to deal with severe radioprotection issues.

1.3.3 Spallation sources

Spallation sources use accelerated high-energy protons (from hundreds of MeV to a few GeV) incident on a thick high-Z target to induce endothermic neutron-generating reactions (the threshold energy is equal to about 100 MeV). Common materials for spallation targets are Pb, W, U or Hg.
A schematic illustration of the spallation process is shown in Fig.1.4. When energetic protons impinge on a spallation target, intranuclear cascades of highly-energetic hadrons (p, n, and pions with E>20MeV) are created. The energy spectrum of the resulting neutrons is characterized by two main components.
In the first place, highly forward-collimated neutrons with energy up to 100 MeV are emitted as a result of direct hadronic interactions between the impinging protons and the target nuclei, enabled by the high kinetic energy of the former. Secondly, following hadronic bombardment, a highly excited nucleus in a pre-equilibrium state is formed. If the height of its fission barrier is comparable to its temperature, the nucleus can dispose of the excess energy via pre-equilibrium fission. If this is not the case, the nuclear evaporation mechanism is activated, leading to the emission of particles with energies below 20 MeV. In this case an isotropic distribution of neutrons with average energy of about 2 MeV is produced. During nuclear evaporation many processes occur. Firstly, light nuclei, together with β and γ radiation, are emitted. Furthermore, some debris nuclides such as ^{8}He, ^{9}He and ^{11}Li can β-decay leading to the emission of nearly monoenergetic neutrons with energy of hundreds of KeV. Also photoneutrons can be produced by the interaction of highly-energetic γ radiation with ^{2}H and ^{9}Be present in the surrounding material. These photons originate from the de-activation of target nuclides or from the above mentioned β-decay of some light spallation products.

Spallation sources provide the highest neutron fluxes, reaching values of 10^{15-16} n/cm^{2}s. They normally work in a pulsed operation mode, even though one continuous spallation source exists in the world, i.e. the SINQ facility [47] in Switzerland. The pulsed operation mode enables the emission of neutrons over time scale ranging from several hundreds of ns to μs. Another advantage is that

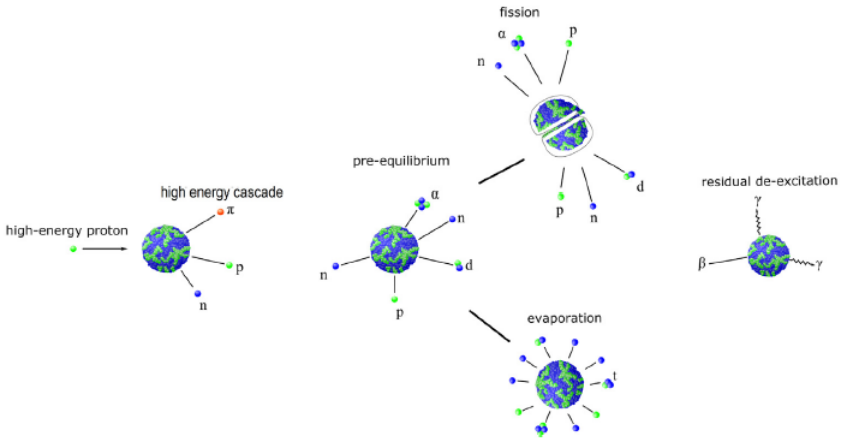

Figure 1.4: *Schematic illustration of the spallation process. The initial impact gives rise to high energy cascades within the nucleus and to the emission of particles with energies close to the incident energy. Later processes include pre-equilibrium, fission and evaporation, which lead to the emission of particles with lower energy and to the formation of daughter nuclei. From [3].*

the heat load on the target is alleviated when averaged over time. Spallation is the most efficient process for neutron production. Indeed, around 20 neutrons per incident proton are produced, with a relatively small heat release (about 30 to 50 MeV per neutron). These features make spallation an ideal process to obtain high neutron fluxes in an efficient way.
However, spallation sources present also drawbacks. In the first place, just as research fission reactors, they are costly to be built, operated and dismantled and require to deal with severe radioprotection issues. Secondly, these facilities require a very complex -and therefore expensive and prone to error- design. Eventually, due to the high energy of the incident protons the area of interaction with the target is elongated to several tens of cm right behind it. This hampers the efficient coupling of the generated neutrons into a compact moderator.

1.3.4 Accelerator-driven low energy neutron sources

Accelerator-driven low-energy neutron sources are accelerator facilities for neutron production generating particles with energy less than 100 MeV operating at a power level below 100 kW. The limits set on the power level of the machine

and on the maximum energy of the accelerated particles remark the distinction between these devices and high-power systems such as spallation sources and nuclear reactors. In contrast with such large neutron production facilities, accelerator-driven low-energy neutron sources are also called "CANS", i.e. *Compact Accelerator Neutron Sources*. Indeed, the main feature of a CANS is the reduced size: the whole neutron-generating system can be hosted in a bunch of properly designed rooms. The relatively simple design of CANS reflects on their reduced cost, which currently amounts to some tens of millions of euros.
CANS started to be developed in the 1970's: the interest in such systems was fostered by the shortfall in the number of the available neutron beams from research fission reactors and spallation sources, combined with the growth of the users' community. In this context CANS soon turned out to be an attractive alternative for many of the needs hitherto served by small reactors, opening up the opportunities for universities and small laboratory installations to enter the field of neutron physics with limited investments and without the proliferation and safety concerns associated with building a research reactor.
The general architecture of a CANS encompasses the following elements:

- A proton or deuteron source;
- A Radio-Frequency Quadrupole (RFQ) stage, whose role is to shape the continuous ion beam and ensure a first acceleration up to an energy of a few MeV. This stage is followed by an accelerator, which accelerates the ions up to the requested energy;
- Optics and transport lines to the target;
- A target made of a material giving rise to neutron-producing reactions when bombarded with ions.

Owing to their modular structure, these machines are extremely flexible in their design and, therefore, can be tailored according to the foreseen area of application.

Physically, accelerator-driven low-energy neutron sources are based on the reaction between accelerated particles and the constituents of a target made of converter material on which they are made to impinge. More specifically, neutron production schemes encompassed by this definition can be grouped into three categories, which will be investigated in detail in the following.

Photoneutrons

In this scheme electrons with energies between 10 MeV and 100 MeV are accelerated and made to impinge on a heavy element target, where neutrons are generated via (γ,n) nuclear reactions. The γ photons originate from both Bremsstrahlung and the nuclear photoeffect in the *giant dipole resonance region*. Giant dipole resonances are high-frequency collective excitations of atomic nuclei, which can be caused by any mechanism imparting enough energy to the nucleus. In this case the mechanism is enabled by high energy electrons, which couple to the nucleus via a virtual γ photon. The resulting nuclear reaction corresponds to the reverse of internal conversion decay [48].
An interesting feature of photoneutrons is that their energy spectrum is independent on the γ-ray spectrum, in particular for high Z materials. This can be seen in Fig.1.5, where the neutron energy spectra obtained by photoreactions on gold with different γ energy spectra overlap. This is due to the fact that the photoneutron energy is selected by the difference in energy between the initial and final state of the nucleus. Hence, the neutron energy spectrum is determined only by the nuclear properties of the converter material. This feature is of great advantage for the study of nuclear reaction cross sections.
Lastly, it should be pointed out that the handling of the γ radiation escaping the target can be problematic for both radioprotection and neutron detection.

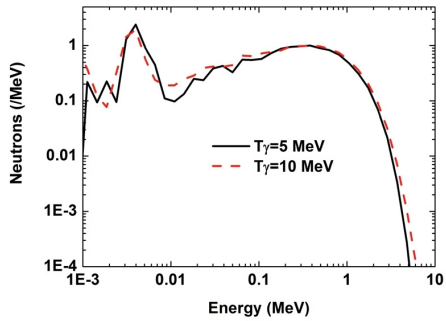

Figure 1.5: *Photoneutron spectrum from a gold target. The black solid line and red dotted line show the neutron spectrum from a 5MeV slope γ-ray and 10MeV slope γ-ray respectively. T_γ is the slope temperature of γ-ray with energy distribution f(E) = exp(-E/T_γ). From [4]*

.

Neutrons from fusion reactions

In these scheme neutrons are produced by means of deuteron-induced nuclear fusion reactions:

$$\begin{aligned} d + d &\rightarrow n + {}^3He + 3.26MeV \qquad E_n = 2.5MeV \\ d + t &\rightarrow n + {}^4He + 17.6MeV \qquad E_n = 14.1MeV \end{aligned} \tag{1.5}$$

Deuterons are accelerated up to the energy of a few hundreds of keV and then made to impinge on a target rich in deuterium or tritium ions, usually incorporated in a solid matrix such as TiDx or TiTx [3]. The design of devices exploiting nuclear fusion for neutron production is similar to that of other accelerators. The apparatus consists of a source for the generation of the positively charged ions, one or more structures for acceleration (electrostatic accelerators are the most common) and a target for ion conversion into neutrons. All the generated neutrons are produced with energy approximately equal to 14 MeV. One of such systems is the *Frascati Neutron Geerator* at the ENEA Laboratory in Frascati, Italy, which is a linear electrostatic accelerator-driven neutron source in which deuterons are accelerated up to about 300 keV at a current of about 1 mA. The system provides a flux of 14-MeV neutrons at intensities of the order of 10^{11}n/s used for neutronics experiments and development of new experimental techniques and detectors [49].

Another type of CANS exploiting nuclear fusion reactions is represented by the so-called "Sealed Tube Neutron Generators" (STNGs). The main feature of such systems is that the ion source, accelerator, optics elements and target are enclosed within a vacuum-tight enclosure, which is constitutes a "neutron sealed tube". A scheme of the architecture of a STNG is shown in Fig. 1.6.
In STNGs the accelerating system is commonly a LINAC, providing voltage up to $\sim$ kV. The most employed ion source in these devices is Penning ion source, which consists of a hollow cylindrical anode with cathode plates at each end. When gaseous deuterium is introduced in the anode region at a pressure of a few mtorr, the electric field between anode and cathode ionizes the gas. The generated ions are successively guided to the acceleration section by a coaxial magnetic field (several hundred Gauss) provided by a suitably shaped external magnet.

Interest in these devices was fostered during World War II in response to the military's need for a long-lived neutron source. Thereafter the technology was transferred to peaceful applications and refined in many aspects. Nowadays STNGs for fixed installations are commercially available on the market and even

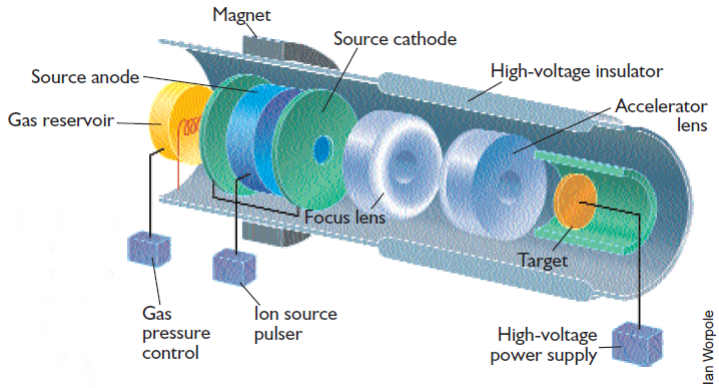

Figure 1.6: *Structure of a Sealed-Tube Neutron Generator (SGNT). From [5]*

some portable models exist. Due to their compactness, these latter devices are attractive for performing in situ measurements and experiments.
Requisites for portable and fixed installation devices are almost the same; the only differences reside in the fact that portable systems should be lighter and more compact, while fixed installation systems should provide higher neutron flux and have a longer operational lifetime [16].
The main features of a device for fixed installation and for portable use are illustrated in table 1.5.

The competitiveness of STNGs in the framework of compact laser-driven neutron sources relies also on their relatively low cost (currently some hundreds of thousands of euros), which makes them suitable for use in companies and university laboratories [50].
Advances in the field of sealed-tube neutron generators technology are oriented to the development of systems combining increased performances (e.g. higher neutron output, longer lifetime), enhanced portability (reduced dimensions and weight) and diminished cost. Another important issue is the improvement in generator design and power supply, in order to obtain lower energy consumption and hence longer operation when working off grid.

Table 1.5: *Neutron generators comparison. MP 320 and D 711 are the commercial names of compact neutron generators produced by the company* Thermo Scientific. *The former is a device for portable use, the latter is a system designed for fixed installation. Reproduced from [16].*

Characteristics	**MP 320**	**D 711**
Maximum neutron yield [n/s]	2×10^8	2×10^{10}
Rated yield [n/s]	1×10^8	1×10^{10}
Time at rated yield [h]	600	1000
Pulse frequency range [Hz]	100-20000	Continuous operation
Pulse duty cycle range [%]	5-100%	Continuous operation
Minimum pulse width [μs]	5	Continuous operation
Maximum high voltage [kV]	110	160
Maximum beam current	80 μA	3 mA
Power consumption [W]	50	n.a.
Total system weight (Neutron generator + Control module) [kg]	12(10+2)	1000
Neutron generator (diam $\times$ L) [cm]	12.1×57.2	25.4× n.a.
Control module (L $\times$ W $\times$ H) [cm]	37.4×15.9×4.6	n.a.

Neutrons from proton- or deuteron-induced reactions

In this scheme a generally light converter material such as lithium or beryllium is bombarded by protons or deuterons with energy in the range 2-50 MeV [3]. Neutron production is the result of ion-induced nuclear reactions.
The generated neutrons possess characteristics which are strongly dependent on the kinetic energy of the accelerated ions and on the nature of the induced nuclear reaction. In principle, a high neutron flux can be obtained accelerating all the ions up to an energy corresponding to a peak in the cross section of the neutron-generating reaction and bombarding the converter material at the highest possible frequency. However, in practice, the accelerator performance in terms of duty cycle and power is always limited by mechanical and heat disposal constraints on the converter.
These latter effects are consequences of the radiative load that the converter must withstand. In fact, when charged ions penetrate into matter many pro-

cesses must be considered. In the first place ions decelerate inside matter depositing their kinetic energy in the form of heat. This can induce local melting of the converter, for which a cooling system must therefore be designed. Secondly, radiation damage (i.e. defects in the crystalline structure induced by the impinging ions) must be taken into account. Eventually, accumulation of gaseous hydrogen at the depth where Bragg peak is situated can lead to the development of mechanical stresses inside the converter and also, eventually, to its disintegration.
As a last point concerning the converter design, attention must be paid to handling issues such as toxicity, inflammability and stability when in contact with air and water.

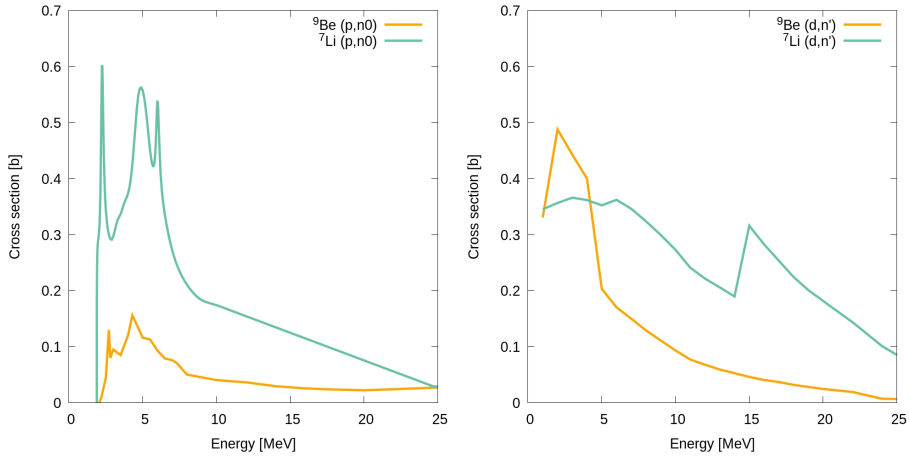

Figure 1.7: *Cross section for the (p,n) (on the left) and (d,n) (on the right) reactions on lithium and beryllium.*

Commonly, in the choice of a proper converter material, the requisite of large ion-to-neutron efficiency in the considered range of ion energy is to a large extent prior to thermal and mechanical requirements, which are tackled with specific converter design. For instance, as anticipated, in the case of low-energy neutron sources light elements such as lithium and beryllium are employed. As shown in Fig. 1.7, the cross sections for the (p,n)and (d,n) reactions of ^{7}Li and ^{9}Be are characterized by a low reaction threshold and a peak at low ion energy. This feature is beneficial for enhancing the source performance, since

Table 1.6: *Selected features of some applications of neutrons.*

Name	Reaction	Neutron flux	Operational mode [7]	$E_{max,n}$	Angular spectrum
Natural sources	Spontaneous fission[8]	2.3×10^6 n/s/μg	C	0-5.5 ∼MeV	Isotropic
	(α,n)	10^7 n/s	C		
	(γ,n)	10^{2-5}n/s/Bq	C	20keV-1MeV	
Fission reactors	(n,f)	10^{13-15}n/cm^2/s	C	up to 100MeV	Isotropic
Spallation sources	(p,n)	10^{15-16} n/cm^2/s	C	up to 1GeV	Forward peaked
CANS	(p,n), (d,n)	10^{13-15} n/cm^2/s	P	Wide spectrum up to tens of MeV	Forward peaked
	(γ,n)	10^{13} n/s/mA	P	Wide spectrum up to tens of MeV	
	(d,d),(d,t)	10^{8-10} n/s	P	2.4 MeV, 14.1 MeV	

ions don't need to be very energetic to induce neutron-producing reactions. All the problematic issues presented above will be discussed in detail for beryllium and lithium in sections 2.2.1 and 2.2.1, respectively.

In conclusion of the chapter a summary of the main characteristics of the above mentioned neutron sources is presented (see table 1.6).

[7] C = continuous, P= pulsed

[8] These data are referred to ^{252}Cf

Chapter 2

Laser-driven neutron sources

This chapter is devoted to the description of the characteristics and working principles of laser-driven neutron sources. In such systems a super-intense laser pulse is delivered on a thin solid target (called *pitcher*), from which ions are accelerated. These latter are subsequently made to impinge on a converter target (called *catcher*), in which ion-induced nuclear reactions lead to neutron production. The physics of laser-target interaction will be discussed in section 2.1, together with the features of the main plasma-based ion acceleration mechanisms and possible schemes for performance enhancement. A discussion on the ion-neutron conversion mechanism will follow in section 2.2, with focus on both theoretical and experimental aspects of neutron production. Finally, information about the current state of the art in the field of laser-driven neutron sources will be given in section 2.3.

2.1 Laser-plasma ion acceleration

As anticipated in the introduction to this chapter, laser-plasma ion acceleration is a technique in which ions are accelerated from a thin solid target as a consequence of irradiation with a super-intense laser pulse. The main feature of super-intense and ultra-short laser pulses is that, when impinging onto a target, they rapidly ionize matter, turning it into a plasma. Currently, super-intense laser pulses can reach intensities of the order of $10^{22}\mathrm{W/cm}^2$. This high value

can be reached using two different approaches:

- Employing laser pulses characterized by high power (of the order of 1 PW). In this case an energy of some hundreds of J is delivered on the target within a time of hundreds of fs - 1 ps. These lasers can work at a maximum repetition rate of a few shots per day;

- Employing more compact and less powerful lasers (hundreds of TW) delivering only a few J on the target. The high intensity is obtained focussing the pulse on very small areas (of diameter 10-100 μm) for very short times (up to hundreds of fs, depending on the laser technology). These lasers are suitable for operation at frequencies ranging from 0.1Hz to 1-2kHz.

The creation of a plasma is necessary for ion acceleration: indeed, plasmas are able to sustain electric fields of the order of some TW/m, which enable the acceleration of charged particles over length scales of the order of a few μm.

The principle on which plasma-driven ion acceleration relies was first formulated by Veksler in 1957 [51] and is called *coherent acceleration*. According to this mechanism, the magnitude of the accelerating field is proportional to the number of particles being accelerated. Although Veksler's idea dates back to 1957, up to 1980's the development of ultra-high-intensity laser systems was hindered by the impossibility of sufficiently amplifying the ps- and ns-long laser pulses due to unwanted non-linearities and optics damage. A breakthrough in the field occurred in 1985, when *Chirped Pulse Amplification (CPA)* was introduced [18]. This technique allowed an immediate increase of a 10^{5-6} factor in the intensity of existing lasers.
Nowadays three main laser technologies are exploited in the field of laser-driven ion acceleration: Titanium:Sapphire, CO_2 and Nd:YAG lasers. Among these, Ti:Sapphire lasers are the most widely used, due to their capability of generating ultra-short pulses (tens of fs) delivering tens of J on a spot with diameter of only a few μm.

While in electron acceleration experiments, the laser pulse is delivered on a gas jet, in laser-driven ion acceleration experiments the target is commonly a thin foil, which, when irradiated, turns into a plasma with density values typical of a solid. Ionizing a thin solid target requires laser intensities greater than 10^{16}W/cm^2. If the intensity is further increased, relativistic effects become non-negligible, above all on the electrons dynamics. An immediate way to understand whether relativistic effects on the electrons motion are negligible or

not is to evaluate the magnitude of the normalized vector potential a_0, which is defined as:

$$a_0 = \frac{e|\mathbf{A}_0|}{m_e c^2}\lambda[\mu m]\sqrt{\frac{e^2\lambda^2 I_0}{2\pi m_e c^3}} = 0.85\lambda[\mu m]\sqrt{I_0[10^{18}W/cm^2]} \tag{2.1}$$

where $\mathbf{A}_0$ is the amplitude of the vector potential of the electric field, while I_0 is the peak intensity of the laser pulse. Relativistic effects cannot be neglected if a_0=1, i.e. when intensities larger than 10^{18}W/cm^2 are delivered on the target. Therefore, when current super-intense lasers interact with matter, a plasma characterized by a relativistic electron dynamics is produced. As will be shortly explained, this is required for laser-based particle acceleration. If intensities of the order or 10^{24}W/cm^2 were reached, the ion dynamics would become relativistic as well; however, such intensities are still inaccessible with the currently available technology.

2.1.1 The physics of laser-plasma interaction

In order to give a satisfactory physical description of laser-plasma interaction, it is useful to introduce some physical quantities that will appear in the discussion. In a plasma at a given temperature charge separation occurs spontaneously as a result of the continuous competition between thermal motion and electromagnetic interaction among charged particles. The characteristic length corresponding to the charge displacement is called *Debye length* and can be defined for each population of particles present in the plasma. If the dynamics of the charges in the plasma is modelled as a harmonic process, a characteristic frequency called *plasma frequency* can be defined as:

$$\omega_{p,i} = \frac{v_{th,i}}{\lambda_{D,i}} = \sqrt{\frac{4\pi n_{0,i} e^2}{m_i}} \tag{2.2}$$

In this expression $v_{th,i} = \sqrt{T_i/m_i}$ is the thermal velocity of charged particles belonging to the i-th species present in the plasma, while $\lambda_{D,i}$, m_i and $n_{0,i}$ are their associated Debye length, mass and unperturbed number density. Since the plasma frequency has an inverse dependence on the mass, electron dynamics will occur on the shortest times scales.

At this point it is useful to discuss under which conditions the propagation of an electromagnetic wave in a certain medium can occur. In general, an electromagnetic wave propagating in a given medium must satisfy Maxwell equations and a dispersion relation derived from Kramers-Krönig relations. In general, plasmas are dispersive media, whose response to external electromagnetic perturbations may be delayed in time and non-local in space. However, the case of an unperturbed, collisionless, non-relativistic, spatially non-dispersive plasma which responds linearly to small perturbations will be considered. When a plane monochromatic electromagnetic wave with wave vector $\mathbf{k}$ and frequency ω illuminates the plasma, it can be sustained only if it is: either a transverse wave with dispersion relation:

$$\omega^2 = \omega_p^2 + |\mathbf{k}|^2 c^2, \tag{2.3}$$

or if it is a longitudinal mode respecting:

$$\omega = \omega_p. \tag{2.4}$$

Remember that the hypotheses of spatially non-dispersive medium implies that the characteristic lengths of the system (i.e. the Debye lengths of the species present in the plasma) are much smaller than spatial variations of the perturbing electric field.
If $\omega \geq \omega_p$ the wave can propagate through the plasma, while if $\omega \leq \omega_p$, it is partially reflected and partially damped inside the medium. In this latter case, the thickness over which the laser interacts with the plasma is called *skin depth* and is defined as:

$$L = \frac{c}{\sqrt{\omega_p^2 - \omega^2}} \tag{2.5}$$

Another useful parameter for describing laser-plasma interaction is the critical density, i.e. the density at which $\omega_p = \omega$:

$$n_c = \frac{m_e \omega^2}{4\pi e^2} = 1.1 \times 10^{21} cm^{-3} \left(\frac{\lambda}{1\mu m} \right)^{-2} \tag{2.6}$$

In this way, the above considerations on frequency can be transposed into considerations on densities. Consider the linear expression of the plasma refractive index:

$$N = \left(1 - \frac{\omega_p^2}{\omega^2} \right)^{1/2} = \left(1 - \frac{n_e}{n_c} \right)^{1/2} \tag{2.7}$$

where n_e is the number density of electrons in the plasma. Then, three different interaction regimes can be individuated:

- $n_e < n_c$: the plasma is *under-critical*, therefore N is real and the laser is able to propagate in it;
- $n_e > n_c$: the plasma is *over-critical* and is opaque to the laser pulse, since N is an imaginary number;
- $n_e = n_c$: the plasma id *near-critical*. Laser-plasma interaction in this regime is characterized by a strong coupling between radiation and matter.

If relativistic effects are considered, the non-linear form of the refractive index must be considered [52]:

$$N_{NL} = \left(1 - \frac{n_e}{n_c \gamma}\right)^{1/2} \tag{2.8}$$

where γ is the *relativistic factor* given by:

$$\gamma \simeq \sqrt{1 + \frac{{a_0}^2}{2}} \tag{2.9}$$

The condition for relativistic plasma transparency then becomes $n_e < \gamma n_c$.

In order to give a satisfactory description of laser penetration into the plasma, radiation pressure effects must be taken into account. When non-linear terms are not neglected in calculations, an effective force proportional to $|\mathbf{E}|^2$ appears. This force is called *ponderomotive force* and is different from zero when non-uniformities in the spatial profile of the electric field are present. It can be defined as:

$$\mathbf{f}_p = -m_e c^2 \nabla \left(1 + < \mathbf{a} >^2\right)^{1/2} \quad \mathbf{a} = \frac{e\mathbf{A}}{m_e c^2} \tag{2.10}$$

Here $\mathbf{a}$=e$\mathbf{A}$/mc^2, where $\mathbf{A}$ is the vector potential of the electromagnetic wave defined as $\mathbf{E}$=$1/c \cdot \partial \mathbf{A}/\partial t$. The ponderomotive force is the effective force describing the motion of a charged particle in an oscillating non-uniform field averaged over one oscillation. $\mathbf{f}_p$ scales as the squared particle charge and inverse particle mass, thus it mainly affects electrons, while its effect on protons and ions in general is negligible. Since $\mathbf{f}_p$ acts on electrons on time scales much shorter than those of characteristic ion dynamics, electrons are forced to separate from ions and to move towards regions where a weaker electric field is present.

If a laser pulse propagates in an under-critical plasma, it can propagate through matter for long distances. In this scenario the pulse acts on electrons,

pushing them towards regions where the $|\mathbf{E}|^2$ is smaller (see Fig.2.1). When the pulse, moving at a velocity close to c overcomes the electrons, these are pushed backwards, again via the ponderomotive force. This results in the fact that electrons are pushed back and forth by the laser pulse: this can trigger a collective oscillation of the electrons, i.e. a plasma wave. If the frequency of the

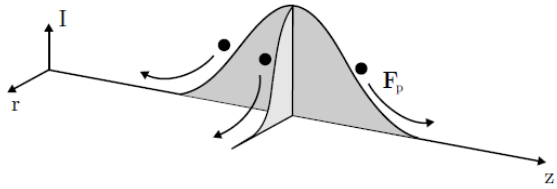

Figure 2.1: *Schematic action of the ponderomotive force. From [6].*

laser pulse is properly chosen, the oscillation can become resonant. In this case electric fields up to the order of some GV/m arise and part of the oscillating electrons are trapped in the regions close to the maximum of the field, where they are accelerated. This phenomena is called *wakefield generation.*
Conversely, if the laser pulse impinges on an over-critical plasma, which is the case of solid thin foils, the interaction is limited to the target surface. In this scenario, the laser pulse transfers part of its energy to the electrons present on the front side of the target through different mechanisms. In all cases, electrons are extracted from the target and then re-injected in the plasma at very high energies. If the accelerated electrons are sufficiently energetic for passing through the target, they give rise to a strong charge separation, which, in turn, leads to strong electric fields on the rear side of the target. This field can lead to the acceleration of hydrogen contaminants naturally present on the rear surface of the target.

When the laser interacts with an over-critical plasma, the generated electrons, moving through the plasma under the action of the ponderomotive force, transport part of the laser energy in the overdense region, where the laser pulse propagation is not allowed. These particles are usually called *hot electrons*: they are relativistic electrons whose energy is of the order of the cycle-averaged oscillation energy in the electric field of the laser in vacuum. Their generation, as well as the understanding of the underlying mechanism, is of crucial importance for ion acceleration. In the frame of super-intense ultra-short laser interaction

with an overcritical plasma three mechanisms for hot electrons generation can be individuated [53]:

1. *Resonant absorption regime*
   When the electromagnetic field of the laser is P polarized, the component of the electric field parallel to the plasma density gradient excites the so-called *electron plasma waves*, which contribute to ion acceleration towards the rear of the irradiated target. Although present, this mechanism is not significant at the intensities typical of a super-intense laser pulse.

2. *Brunel heating*
   In presence of a steep plasma density gradient and P polarization, electrons are extracted from the skin layer by the combined action of the fields of the incoming and reflected laser pulse. After a half oscillation they are reinjected into the target with high energy due to the action of the normal component of the electric field. Due to this, the Brunel effect vanishes when no component of the electric field normal to the surface is present, i.e. at normal incidence and for S polarization.

3. $\boldsymbol{J}\times\boldsymbol{B}$ *heating*
   In this scheme electrons are extracted from the target just as above, but they are later reinjected thanks to the oscillating component of the $\mathbf{J} \times \mathbf{B}$ force. This mechanism is strongly quenched for C polarization, in which the oscillating component of the $\mathbf{J} \times \mathbf{B}$ force is suppressed.

2.1.2 Target Normal Sheath Acceleration

Having introduced the mechanism at the basis of ion acceleration within a plasma, a fundamental issue is whether it is possible to conceive theoretical models relating the characteristics of the accelerated ions to laser and target properties. Among the numerous proposed mechanism Target Normal Sheath Acceleration (TNSA) has proven to be the most solid, due to the agreement of predictions with experimental data.

The mechanism at the basis of TNSA is the following. As already explained, the ponderomotive force acts on electrons with a time scale much shorter than that of ion dynamics. This implies that, while the ions can be considered still, hot electrons are formed on the front side of the target. These electrons escape from the rear side, where they form a cloud with a length of a few λ_D. Because of the induced charge separation, an electric field called *sheath field*, decaying

outside the target on a distance of a few μm, arises. Thanks to the sheath field, ions belonging to the contaminants layer present on the rear of the target are accelerated. The ultimate ions trajectories depend on the local orientation of the rear surface and on the electric field lines driven by the time-dependent spatial electron density. The ions accelerated at the highest energy commonly reside at a maximum depth of a few μm from the target surface, while the low-energy ions in the spectrum are accelerated by rarefaction waves propagating into the target as TNSA proceeds. A scheme of TNSA is shown in Fig. 2.2.

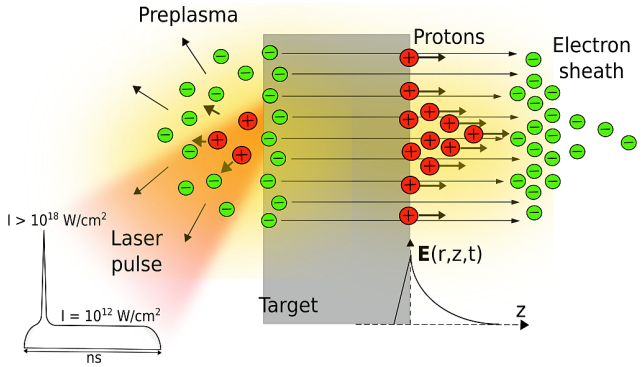

Figure 2.2: *TNSA scheme. From [7]*

In TNSA ions are accelerated proportionally to their charge-to-mass ratio: therefore, protons will be accelerated first, while the acceleration of other ion species takes place over longer time scales. Independently from the accelerated ion species, energy gains of the order of some tens of MeV per nucleon can be obtained.

The entity of the sheath electric field can be estimated by making use of dimensional arguments. Indeed, if the sheath extends over a length L_s and hot electrons have a temperature T_h, the field can be estimated as:

$$E_s = \frac{T_h}{L_s} \tag{2.11}$$

Using the electrons Debye length (a few μm) for the estimating L_s and considering that generally the temperature of electrons produced in typical experiments is of the order of the MeV, E_s is of the order of some MV/m, i.e. some TW/μm.

More realistic estimates can be performed using theoretical models for TNSA description [54].

Ions accelerated by TNSA are characterized by a typical decreasing exponen-

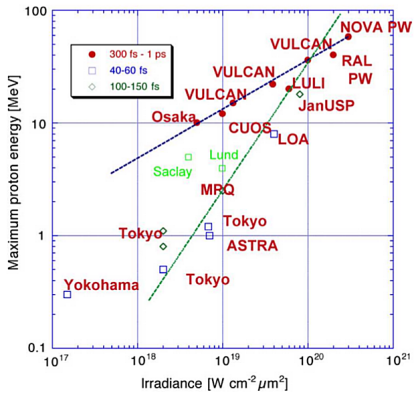

Figure 2.3: *Maximum proton energy as a function of the irradiance for three possible ranges of laser pulse duration. From [8]*

tial energy spectrum with a certain cutoff energy. In this regard, scalings can be very useful for predicting the performance of ion acceleration at laser intensities which exceed present-day capabilities. For example, in Fig. 2.3 the maximum proton energy against the laser irradiance I_r for some existing laser facilities is shown. As it can be seen, two different trend lines are present, which can be attributed to different strategies for obtaining super-intense pulses. Indeed, lasers delivering highly powerful pulses show a $\sim I_r{-}1/2$ scaling, while less powerful ultra-short systems scale as I_r.

At present, it is not guaranteed that the ion energy scaling observed so far will be maintained with growing laser intensities. Furthermore, the availability of lasers of increasing power unveiled the existence of many different laser-ion generation mechanisms, such as radiation pressure acceleration (RPA), collisionless shock acceleration, break-out afterburner (BOA), Coulomb explosion, hole boring (HB) and relativistic transparency (RT) [52]. Notice that a TNSA component of acceleration is always present, even when trying to suppress it for studying alternative acceleration mechanisms.

2.1.3 Innovative target materials for enhanced TNSA

In order to be appealing for applications, laser-driven ion sources should provide energies of the order of 1-100 MeV and average currents from a few nA up to a few mA. These values still exceed the performance of current laser-driven sources. In order to fulfil the aforementioned requirements, it would be beneficial to employ high repetition rate laser systems. As explained at the beginning of the previous section, this cannot be achieved using highly powerful lasers. On the other hand, lasers with a power of a few hundreds of TW are suitable for working at repetition rates ranging from 0.1Hz to 1-2 kHz. These devices manage to produce super-intense laser pulses delivering only some J on the target, but focusing the laser beam over regions of a few μm for very short times (tens or a few hundreds of fs).
All of this considered, the design of a target enabling performance enhancement and able to work with a certain repetition rate would be crucial for making laser-driven ion sources viable contenders for specific applications.
With this aim several target schemes have been proposed throughout the years: ultra-thin foils [55, 56], reduced mass targets [57], nanosphere targets [58], grating targets [59] and and ultra-thin diamond-like carbon foils covered with carbon nanotubes [60]. Although effective for enhancing the source performance, many of these scheme require ultra-high laser systems and cannot work in a repetitive mode.
Besides enhanced acceleration performances, the design should require provide robustness, so that the targets could be handled easily without any risk of damage.

A promising path towards the goal is represented by *double layer targets* (henceforth called DLT) constituted by an ultralow-density layer (foam) deposited on a μm-thick solid foil. The idea at the basis of this scheme is that the interaction of a laser with this target will result in the formation of a controlled near-critical ($n_e \sim n_c$) plasma layer on the illuminated surface. This layer should allow a greater coupling between laser and target. Indeed, in this scenario the laser is able to achieve deeper penetration in the plasma, therefore extending the region of laser-energy absorption to the whole plasma volume. This results in an enhanced efficiency in laser-ion energy conversion, along with a greater cutoff energy and number of accelerated ions with respect to solid foil targets.
Assuming for the laser wavelength typical values of systems employed in high-intensity experiments (i.e. $\lambda \sim$0.8-1μm), the corresponding plasma critical den-

sity is:

$$n_c = \frac{m_e \omega^2}{4\pi e^2} = 1.1 \times 10^{21} cm^{-3} \left(\frac{\lambda}{1\mu m} \right)^{-2} \sim 0.88 - 1.1 \times 10^{21} cm^{-3} \qquad (2.12)$$

This corresponds to mass densities of a few mg/cm^3, which is 400 times lower than graphite density and a few times the density of air. The only solid materials possessing such low densities are foams. These are extremely challenging materials to be manufactured, since advanced materials science techniques are required. One way to produce a nanostructured DLT is to grow the foam on the solid substrate using pulsed laser deposition (PLD) techniques. By varying deposition parameters such as the pressure in the deposition chamber, temperature and deposition time, it is possible to achieve good control over the foam density, thickness, morphology and structure [61]. The influence of some of the aforementioned parameters on the foam architecture is shown in Fig.2.4.

These targets have been experimentally tested at both moderate [62] and relativistic [9] laser intensities, showing a significant improvement with respect to bare targets. More precisely, as expected from theory, a greater efficiency in the conversion of laser energy into ion kinetic energy is registered when a carbon foam is used.
Furthermore, the presence of the nanostructured material makes the ion spectrum less sensitive to the laser polarization: while with a homogeneous plasmas there is a non negligible polarization dependence of the energy absorption efficiency, differences are strongly attenuated with nanostructured plasmas (see Fig. 2.5). This can be attributed to the fact that a laser pulse interacting with a nanostructured target impinges on randomly oriented surfaces due to the presence of porosities.
The effect of the nanostructured material on the ion energy spectrum is shown in Fig.2.5 for different values of foam thickness. The image shows that the ion maximum energy is increased by the presence of the nanostructured foam, with an optimum value for thin foam layers. The maximum gain ratios (i.e. $E_{p,max}$ with foam/$E_{p,max}$ with simple foil) obtained in the above-cited cases ([62], [9]) are respectively equal to 2-3 and 1.4-3.

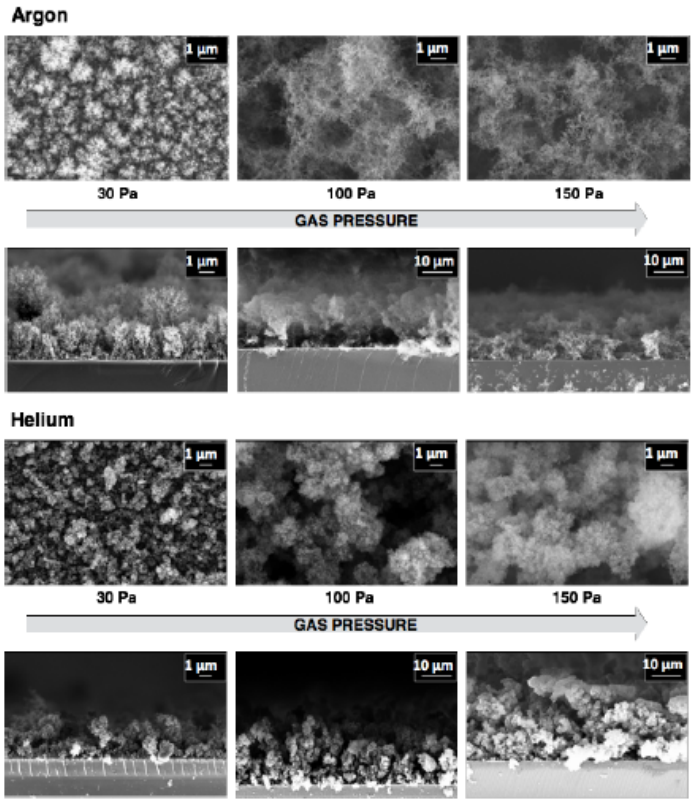

Figure 2.4: *Scanning Electron Microscopy images showing the dependence of nanostructure's morphology on the deposition chamber gas properties. Top views and cross sections alternate on the rows. From [6].*

2.2 Neutron generation from laser-driven ions

As anticipated in the introduction to this chapter, laser-driven neutron sources are generally based on a *pitcher-catcher* scheme, in which ion- and neutron-generation processes take place in two physically separated targets. Another possibility to achieve neutron production is to work in a *bulk scheme*, in which one single thicker target is employed, where both ion acceleration and nuclear

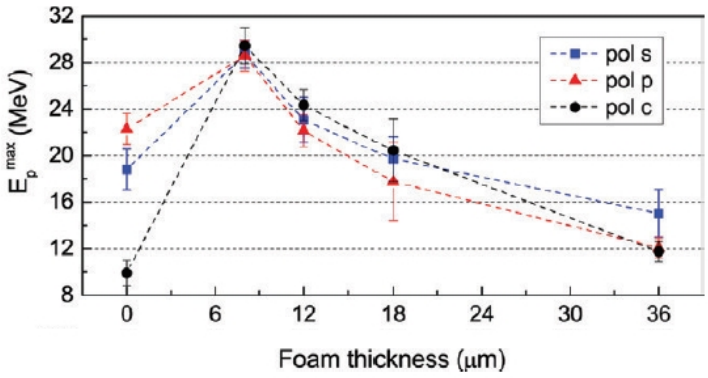

Figure 2.5: *Role of the foam thickness and laser polarization. $E_{p,mx}$ as a function of the foam thickness for s- (blue squares), p- (red triangles) and c- (black circles) polarization for different values of foam thickness. From [9].*

reactions take place under the action of a sufficiently intense laser pulse. The two schemes are shown in Fig.2.6.
The most interesting scenario in the framework of this thesis is represented by a pitcher-catcher setup, which will be further discussed in the following sections.

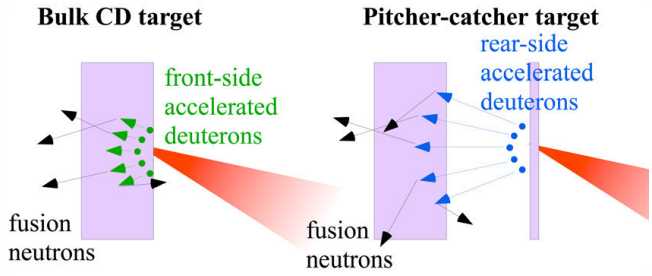

Figure 2.6: *Schematic of pitcher-catcher and bulk schemes for neutron production.*

2.2.1 Nuclear reactions for ion-neutron conversion and converter materials

In a laser-driven neutron source employing a pitcher-catcher scheme, the neutron generation process occurs in the same way as in CANS (Compact Accelerator Neutron Sources): the ion beam impinges on a target made of converter material in which neutron-producing reactions take place. As explained in section **??**, a large number of ion-induced nuclear reactions for neutron production exist, which can be categorized in different groups according to the particle inducing the process. One possible mechanism is to exploit ion-induced nuclear reactions for neutron production.

A preliminary step in the individuation of a suitable process for neutron generation is the analysis of the cross section of the candidate reactions. Indeed, in view of the creation of a competitive neutron source, the reactions guaranteeing the highest possible neutron yield should be selected.
In general, nuclear reactions possessing a cross section peaked at low energies provide higher neutron yield. This is due to the fact that, at a certain moment during their slowing down process, all the ions cross the energy value corresponding to the cross section's peak, therefore increasing the reaction probability. For this reason, in the framework of laser-driven neutron sources, reactions induced by protons or deuterons on low Z materials such as lithium and beryllium are the common choice. The cross section of (p,n) and (d,n) reactions on these materials is plotted in Fig.2.7.
In Fig.2.7 also the cross sections for (p,n) and (d,n) nuclear reactions on a set of medium Z materials are shown. Specific isotopes of these elements possess cross sections for ion-induced neutron production which are peaked at higher energies with respect to low Z elements. Therefore these materials, by virtue of their large cross section at peak energies, could be in principle employed in experiments involving particularly energetic ions or in peculiar converter design [15]. The possibility to employ medium Z materials in laser-driven neutron sources will be discussed in greater detail in chapter 4.

The Q-value and threshold energy for (p,n) and (d,n) reactions on lithium and beryllium are listed in table 2.1. As a general feature, the Q-value is negative for (p,n) reactions, while it is positive for (d,n) reactions. This implies that, at even ion energy, deuterons produce the most energetic neutrons. In particular, the Q-value of (d,n) reactions on beryllium and lithium is equal to 4,362 and 15,03 MeV, respectively. Furthermore, being exothermic, (d,n) reactions have

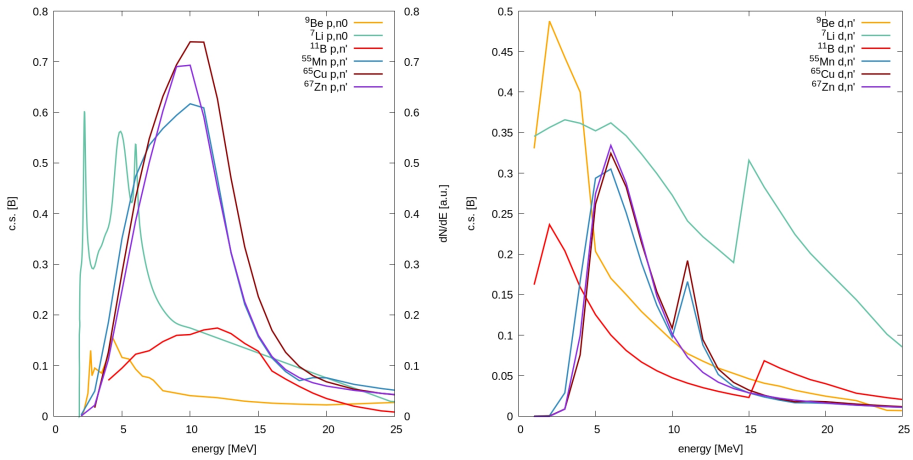

Figure 2.7: *Cross section for the main (p,n) (on the left) and (d,n) (on the right) reactions on a set of converter materials.*

no energy threshold: this implies that, in principle, all the ions produced by laser-plasma interaction are available for reaction. However, it can be seen from Fig.2.7 that no data for the cross sections are reported at energies smaller than 1 MeV. After a research of experimental data of cross sections of deuteron-induced reactions, it was seen that only very few data are available in that energy range. This issue will be taken up again in chapter 5, with reference to the simulation of a compact laser-driven neutron source. The same does not occur in beryllium, where all the (p,n) reactions have an enenrgy threshold slightly lower than 2 MeV in both the aformentioned converter elements.

Table 2.1: *Q-value and E_th for (p,n) and (d,n) reactions on lithium and beryllium.*

Element	**Reaction**	**Q-value [MeV]**	**E_{th} [MeV]**
Beryllium	(p,n)	-1.85	2.06
	(d,n)	+4.36	0
Lithium	(p,n)	-1.64	1.88
	(d,n)	+15.03	0

Besides neutron yield and energy requirements, another selection constraint in view of applications could concern directionality: the more collimated the produced neutron beam is, the higher the achievable fluences. In particular, the neutron beam divergence from a laser-driven pitcher–catcher source in the laboratory frame will be a convolution of the divergence of the input ion beam and the neutron beam divergence expected for a collimated beam of ions.
Reactions involving light ions such as ^{7}Li(p,n)^{7}Be, ^{9}Be(p,n)^{9}B,^{13}C(p,n)^{13}N, d(d,n)^{3}He, ^{7}Li(d,xn)^{A}X, ^{7}Be(d,xn)^{A}X allow highly peaked fluxes by producing a narrow cone beam of neutrons. Among the candidate reactions, those occurring in lithium and beryllium are those providing the most collimated neutron flux. Indeed, the neutrons produced via the ^{7}Li(p,n)^{7}Be and ^{9}Be(p,n)^{9}B reactions for proton kinetic energies just above the production threshold are cinematically focused into a cone in the direction of the proton beam [11].
On the other hand, the neutrons generated by the (d,n) reaction on these elements are characterized by a degree of anisotropy increasing with the impinging ion energy. This behaviour is displayed in Fig.2.8 for deuterons impinging on lithium with different kinetic energies. At values of the order of a few tens of MeV this behaviour is mainly due to *stripping reactions*, which imply the capture of the deuteron's proton when the nucleons pass near the target nucleus along with the scattering of the remaining neutron, typically at small angles.
This process also accounts for the typical shape of the energy spectrum of neutrons produced by (d,n) reactions on a wide class of elements. As it can be seen in Fig./reffig:tunability, for impinging deuterons with energy E_d, a peak in the neutron spectrum appears at $E_n \sim E_d/2$ [10]. This feature enables a certain degree of tunability in energy of the neutron source.
The role played by the ion beam divergence on the anisotropy of neutron emission in the case of laser-driven neutron sources has been investigated in many studies [63–65].

Finally, it is crucial for the feasibility of a laser-driven neutron source to discuss some issues related to the converter technological properties and handling prescriptions. As explained above, the most commonly employed converter materials are lithium and beryllium. The problems associated to the use of such elements in laser-driven neutron sources, as well as in CANS, are:

1. Low melting temperature. This is, in general, the limiting factor for the maximum energy that can be delivered on the target and, in turn, for the maximum neutron energy.

2. Mechanical stresses induced either by temperature gradients throughout

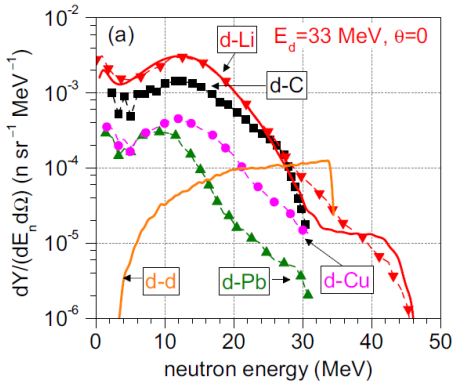

Figure 2.8: *Neutron spectra from nuclear reactions driven by a beam of monoenergetic deuterons with energy 33MeV impinging normally onto thick converters of various materials. The observation direction is $\theta = 0$. Solid lines are the outcome of simulations performed for D and Li. From [10].*

the converter or by the flow of a coolant needed for avoiding the material melting.

3. Hydrogen embrittlement induced by *blistering*, i.e. the accumulation of gaseous hydrogen at a depth corresponding to the ions Bragg peak in the converter material. The name of this phenomenon is due to the damage appearing on the target surface, which resembles a blister. This process leads to target distruction after a certain time of operation.

With regard to handling prescription, the ideal converter should be easily employable, which implies sufficient mechanical robustness for manipulation, reduced toxicity and reactivity with oxygen and water and, eventually, the absence of long-life radioactive nuclides among the reaction products.
Some examples of converter materials already employed in accelerator-based neutron-production are shown in table 2.2.

All the aforementioned aspects will be addressed in greater detail in the following paragraphs, for the specific cases of lithium and beryllium converters.

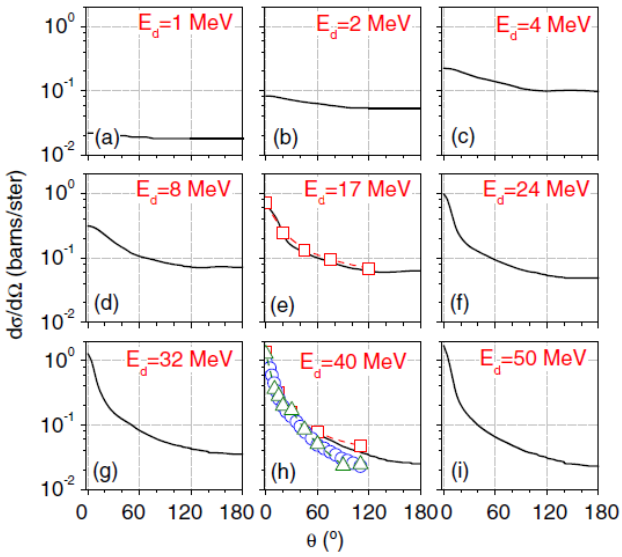

Figure 2.9: *Angular distribution of the differential cross section for neutron production $d\sigma/d\Omega(E_d,\theta)$ from $^7Li(d,n)^7Be$ nuclear reaction for selected deuteron energies. Black solid lines represent the cross section data calculated analytically by the authors, while the symbols represent experimental data [11].*

Table 2.2: *Neutron-generating reactions in compact accelerator-based neutron sources. Reproduced from [3].*

Reaction	$\mathbf{E}_{projectile}$ **(MeV)**	$\mathbf{E}_{Threshold}$ **(MeV)**	$<\mathbf{E}_{neutron}>$ **(MeV)**	**Neutron yield (n/mA/s)**
^{7}Li(p,n)^{7}Be	~2.50	1.88	~0.60	9.09×10^{11}
^{9}Be(p,n)^{9}B	~4-20	2.06	~1.60-8.00	$0.50\text{-}1.20\times10^{12}$
^{9}Be(d,n)^{10}B	1.50	0	1.66	3.30×10^{11}
^{2}H(d,n)^{3}He	0.15	0	2.50	$\sim2.00\times10^{9}$
^{3}H(d,n)^{4}He	0.15	0	14.10	$\sim5.00\times10^{10}$
^{13}C(d,n)^{14}N	1.50	0	1.08	1.9×10^{11}
^{12}C(d,n)^{13}N	1.50	0.33	0.55	6.00×10^{10}

Lithium

Lithium converters have been widely tested in the past decades in the framework of compact accelerator neutron sources (CANS). As mentioned in the previous section, a distinction must be made between monoenergetic ions typically produced by accelerators and ions with a wide spectrum, as in the case of laser-driven ion sources. Given that this difference cannot be disregarded in the ultimate design of the converter, the following considerations on its architecture are valid in both schemes. Besides its high neutron yield lithium has numerous drawbacks from an engineering point of view.

In the first place lithium possesses an extremely low melting temperature (182°C) and a low thermal conductivity (85 W/mK). This implies that, as long as interaction with a solid target is required, a cooling system must be integrated in the target structure, enhancing its complexity and cost. The cooling system should be able to dispose of the heat load caused by the impinging ion beam. For this purpose, cooling systems based on a water flow well-separated from the lithium have been proposed. Such systems work up to the melting point of water, i.e. at 100°C. This limit was overcome by employing a liquid metal heat carrier (gallium), which also eliminates the danger of extremely violent reactions in case of coolant leakage into the chamber volume. In fact, lithium reacts exothermically with water and, hence, with the humidity contained in air. However, this strategy proved to be unviable due to the chemical reactivity of the liquid metal at high temperature [66].
Another solution to the heat load problem is to work with liquid lithium, therefore eliminating the 182°C maximum temperature constraint [67]. Experimentally, a flow of liquid lithium exposed to vacuum has been irradiated with protons of energy 1.940 MeV and average current on target of 1.2 mA. In this scheme it has been possible to work at temperatures greater than 200°C obtaining a neutron flux of 3×10^{10}n/s which, as expected, is higher than the one obtained with limiting temperature constraints. However, in this scheme the danger of explosion caused by any leakage of liquid lithium exists. Furthermore, the exploited nuclear reaction on ^{7}Li produces ^{7}Be, which is a 478 keV γ-emitter with a half-life of 53.3 days. For both these reason the target was encapsulated in a stainless steel envelope.

A further issue that must be addressed for lithium converters is hydrogen embrittlement caused by ion injection. To overcome this problem, a peculiar converter design has been proposed, in which a layer of material with high hy-

drogen diffusion coefficient is placed at the depth corresponding to the Bragg peak of the accelerated ion species [68]. This diminishes the quantity of hydrogen retained by the material.

Eventually, it is noteworthy to mention lithium compound converters: in particular, a widely used material in laser-driven neutron generation experiments is lithium fluoride (LiF). Despite its toxicity when swallowed or inhaled [69], this compound shows a melting temperature of 848°C, which is much higher than the one of lithium. This enables the possibility to release, to a large extent, the heat load constraint on the target. From a neutronic point of view fluorine can contribute to the overall neutron yield with the reaction ^{19}F(p,n)^{19}Ne, whose cross section in the energy range 20-30 MeV is 15–25 mb, i.e. comparable to that of ^{7}Li(p,n)^{7}Be (see Fig.4.3).

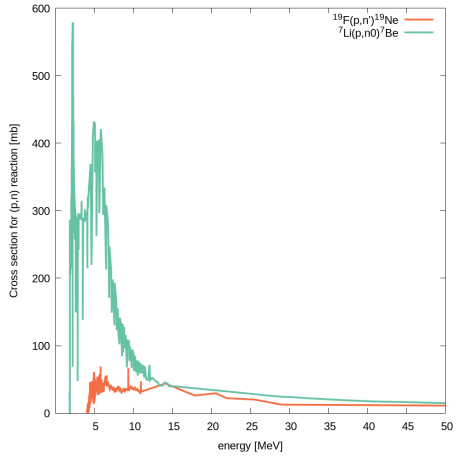

Figure 2.10: *(p,n) cross sections for lithium and lithium fluoride.*

Beryllium

In beryllium many mechanisms of neutron generation are active at different energies. All the $^{9}Be(p, n+x)$ reactions with energy threshold lower than 15 MeV are listed in table 2.3.
The first reaction reported in the table is ^{9}Be(p,n_0)^{9}B, which occurs through the formation of the compound nucleus ^{10}B. The writing n_0 denotes the fact

Table 2.3: *$^{9}Be(p,xn)^{A}X$ reactions with energy threshold lower than 15 MeV. From [17].*

Reaction	Q-value [MeV]	Reaction threshold [MeV]
p+^{9}Be→ ^{9}B+n	-1.850	2.057
p+^{9}Be→ ^{9}B+n+γ	-1.886	2.057
p+^{9}Be→ ^{8}B+p+n	-1.665	1.851
p+^{9}Be→ ^{8}Be+p+n+γ	-1.701	1.851
p+^{9}Be→ ^{5}Li+α+n+γ	-3.538	3.933
p+^{9}Be→ 2α+p+n	-1.573	1.749

that the generated neutron leaves the nuclide in its ground state. Other important (p,n) reactions are: neutron generation from the first excited state of the ^{9}Be nucleus (second line) and three-body breakup (third line). The remaining reactions are less important from the point of view of the neutronic yield.
It should be noticed that many among the reported reactions proceed through excited reaction intermediates, which de-excite emitting γ-rays. The presence of high-intensity γ radiation, besides being hazardous from a radioprotection point of view, constitutes a problem for the formation of a pure neutron beam. To overcome this, a lead sheet can be installed downstream of the beryllium target, with thickness optimised in order to achieve complete γ suppression.

Although the first experiments on accelerator-based neutron production used lithium as converter material, this was soon abandoned due to the aforementioned weak thermal performance. Consequently, beryllium converters started to be investigated as a possible alternative. Despite providing smaller neutron yields, beryllium has better thermal properties if compared to lithium, with a melting point of 845°C and a thermal conductivity of 218 W/mK.

The heaviest problem affecting beryllium converters is blistering (see the beginning of this section for further information). To solve this problem, a scheme similar to the one adopted for lithium was conceived [12]. This consists in a backing material to be placed on the rear of the beryllium target hosting a region with high hydrogen diffusion coefficient (see Fig.2.11). The converter material was designed and optimized considering both mechanical and thermal aspects. In particular the target should withstand a certain pressure against vacuum and the pressure of the cooling water flow. Moreover, it should be able

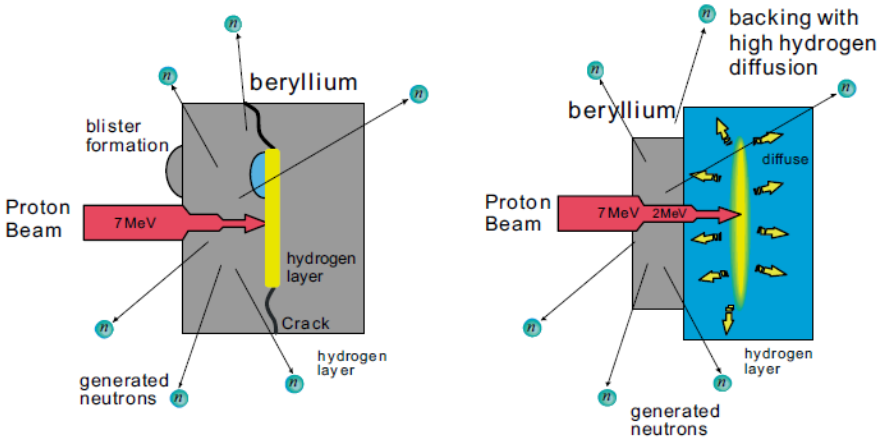

Figure 2.11: *Blistering mechanism in thick beryllium target (left) and concept of new target structure using a backing material with high hydrogen diffusion coefficient (right). From [12].*

to dispose of the heat generated by the deceleration of the impinging ions. This system resulted in no blistering or cracking after one year of operation (i.e. 2000 h of proton beam irradiation at 100 μA and 192 h of cooling).
Furthermore, attention was drawn on the choice of a highly permeable-to-hydrogen material which would not give rise to long-life activated nuclides after irradiation. All of this considered, vanadium was selected. Even after one year of operation no activation of vanadium was detected: the only radioactivity present came from the employed brazing material, namely, a solution of silver and indium. To hinder this effect, a direct bonding technology should be employed.

In order to combine the good neutronic properties of lithium with the larger operational temperature range of beryllium, a bilayer converter design employing both materials has been conceived [70]. In this scheme protons impinge on a thin beryllium target, which is cooled on its rear side by a flow of liquid lithium. This latter layer also acts as a second neutron production target. In this configuration the beryllium layer acts as a barrier for the liquid lithium region. Although experiments with this converter design haven't been reported in the literature, based on calculations the proposed scheme seems to enhance

neutron production performances, even if problematic issues such as blistering and activation haven't been addressed by the authors.

2.3 State of the art

Neutron production using super-intense lasers has been investigated since the pioneering work by Norreys and colleagues in 1998 [71]. In their experiment a 1.3 ps-long laser pulse impinges on a deuterated target, enabling neutron production via D(d,n)^{3}He nuclear reactions. Since then, research on laser-driven neutron production has continued on two fronts, fostered by factors such as the reduced cost and the limited radioprotection issues with respect to conventional neutron sources: on one side, PW-class laser facilities have been devoted to the production of high neutron fluxes; on the other side, the possibility to produce moderate fluxes with less powerful TW-class lasers has been explored. This latter scheme is of interest for applications requiring a relatively low flux of neutrons with energy up to a few tens of MeV. The produced neutron bunch has a very short duration (of the order of tens to fs at the source position), which is advantageous from the point of view of applications. Furthermore, the reduced size and cost of TW-laser systems, along with their limited radioprotection issues, make them suitable for installation in universities and small laboratories. Present-day super-intense lasers can produce pulses with intensities larger than 10^{21} W/cm^2 [14]. The highest neutron yields are observed using PW-class lasers and amount to about 10^{10} n/shot [65].
The complexity of the systems under investigation encouraged, throughout the years, the development of analytical and numerical tools suitable for their description. Such methods are aimed at both helping theoretical investigation and improving the design of experiments. The most widely diffused numerical techniques are *particle-in-cell* codes for simulating laser-plasma interaction and *Montecarlo* codes for the study of ion-neutron conversion.
Both experimental and theoretical investigations that can be found in the literature in the framework of laser-driven neutron sources will be discussed in the following section, in order to outline the state of the art of the field.

2.3.1 Experiments of laser-driven neutron sources

As explained in section 2.1, super-intense lasers employed in laser-driven neutron sources can be divided into two groups: PW-class and TW-class lasers. While

the former devices produce high intensity pulses delivering a large amount of energy on the target (some hundreds of J within some hundreds of fs - 1 ps), the latter rely on pulses delivering a limited amount of energy (up to a few J) focused on a very small area and within a very short time (up to a few hundreds of fs). The laser technology employed for producing extremely short pulses is Ti:Sapphire, with which durations down to tens of fs can be reached.
Large laser facilities are particularly expensive to build and operate, seen the large infrastructures needed. For this reason only a few of them exist and they are primarily devoted to the study of nuclear fusion.
On the other side, among TW-class lasers, particularly compact devices are the so-called *table-top lasers*, whose power is currently limited to a few tens of TW. These systems are characterised by reduced size (they take the space of a room) and relatively low cost. This makes them suitable for installation in research centers and universities. Furthermore, following a further reduction in the dimension of table-top lasers, neutron sources based on such devices might be promising candidates for the realization of a portable neutron-generating device.
While PW-class laser systems are able to produce 10^{10} neutrons per shot, for table-top lasers this value is reduced by two or three order of magnitude. Anyhow, it must be considered that, due to the large amount of power required, PW-class lasers can be operated with a repetition rate of only a few shots per day. Conversely, TW-class lasers are able to work in a repetitive regime with frequencies up to the order of the kHz [72, 73]. A high repetition rate is fundamental for producing neutron fluxes sufficient for applications.

The overwhelming majority of the experiments on laser-driven neutron sources reported in literature have been performed using PW-class lasers. On one side, this choice is motivated by the wish to obtain large fluxes of energetic neutrons in view of applications; on the other side, large laser facilities are already equipped for dealing with radioprotection issues related to neutron production. However, also a few experiments employing table-top lasers are reported in literature. These have been mainly performed at the university of Michigan and, more precisely, at the "HERCULES laser facility" [74] and at the "Lambda cube" laser facility" [75]. Besides taking up several rooms of space and being able to provide beams of 300 TW in power, the HERCULES laser can also be used in a "table-top" regime, hence providing shots delivering only 1-1.5 J on target with frequency up to 0.1 Hz [14].
On the other hand the "Lambda cube" laser is a table-top Ti:sapphire laser providing a focal intensity of $5\times10^{18}\mathrm{W/cm^2}$ and delivering 4 mJ on the target

at each shot. Employing this laser system, experiments aimed at the creation of a high-frequency pulsed laser-driven neutron source were performed [72, 73]. For this purpose, the laser was made to impinge on a channel containing flowing heavy water (D_2O), where neutrons are produced thanks to the d-d fusion reaction. The laser, providing an intensity of 10^{19}W/cm^2 and laser pulses of the duration of $\sim$40fs was operated at a frequency of 1-2 kHz. The energy delivered on the D_2O-channel at each shot amounted to $\sim$6-18mJ. This configuration resulted in the production of neutrons with maximum energy of 2.45 MeV and flux $\sim 10^5$ n/s. This value is comparable to other table-top laser based neutron sources [76, 77], but in this scheme continuous all-day operation was possible.

As pointed out in section 2.2, laser-driven neutron sources can rely either on a "pitcher-catcher" or on a "bulk" scheme.
In the vast majority of experiments reported in literature a "pitcher-catcher" scenario is employed. The structure of the pitcher depends on the charged particles being accelerated. Indeed:

- If protons or electrons are accelerated, common target materials are plastics such as mylar, polyethilene and polystyrene or metals such as Al, Au and Cu. Since metals normally do not contain hydrogen, the acceleration of protons relies on the presence of a layer of hydrogen-rich contaminants on the rear of the target.

- If energetic deuterons are required, deuterium-rich targets must be employed. More precisely, the use of targets made of deuterated PE and PS is reported in literature. Another method for accelerating deuterons is to apply on the rear of the target, which can be made of normal or deuterated plastic, a layer of deuterated contaminants. Many deuteration techniques have been proposed, among which the application of a deuterated paint or the production of a layer of deuterated ice on the rear of the target [14].

All the mentioned targets have a thickness ranging from hundreds of μm to 1mm.
Conversely, only in a few cases the bulk scheme has been employed in experiments [72, 73, 78]. In this case a target commonly made of deuterated plastic is directly irradiated by the laser and neutron production occurs due to d-d fusion reactions. d-d fusion reaction produces 2.45MeV neutrons, which is much less than the 14.1MeV conferred to neutrons by the d-t fusion reaction. However, tritium is never employed in the context of laser-driven neutron sources due to

its radioactivity[1].

The most relevant acceleration scheme employed in laser-driven neutron generation is TNSA (see section 2.1.2), but also other mechanisms such as breakout-afterburner (BOA) and relativistic transparency (RT) have been investigated. In particular, in the framework of laser-driven neutron sources the maximum neutron energy obtained with TNSA is about 40MeV, while for BOA and RT schemes neutrons were generally accelerated to much larger energies (up to 140MeV) [79–81], also due to the fact that these regimes require an intensity on target greater than TNSA to be established.

As regards neutron production, the following discussion will be referred to a pitcher-catcher scenario. In order to optimize the neutron spectrum in view of a certain application, the choice of the converter material is crucial. When protons or deuterons are accelerated, the most widely used converter materials are beryllium, lithium or lithium fluoride, in a thickness ranging from 0.5mm to 2cm. Their strong points and drawbacks have been discussed in section 2.2.1.
The possibility of employing medium Z materials such as copper, zinc and manganese as converters has been investigated theoretically and deemed as interesting [82]. In literature one work by Zagar and colleagues reports the investigation of neutron production in lead. In particular, they have analysed the energy spectrum for a beam of protons accelerated by the VULCAN laser (intensity 4×10^{20}W/cm^2, pulse energy 400J and pulse duration 0.7ps) obtained by McKenna and colleagues and have calculated theoretically the resulting neutron spectrum [83,84]. Starting from an exponential spectrum with proton cutoff energy of ∼45MeV, calculations showed that 2×10^9 neutrons per laser shot were generated with maximum energy of ∼35MeV. Although the number of produced neutrons is comparable to the one obtained in other experiments [**?**, 82], these performance level can be reached only using highly energetic protons, since the cross section of lead for (p,xn) reactions is significant only for energies greater than 15MeV.
Besides ion-neutron conversion, heavier elements such as Au, W or Cu are employed for the production of photoneutrons (see section 1.3.4 [4,79,85]). Despite the low efficiency of the Bremsstrahlung process, which also causes huge target heating, 2×10^6n/shot have been obtained using a 26.6mm thick tungsten converter and a table-top 10 TW laser ("UT^3 laser lab" at University of Texas, Austin). The estimated neutron peak flux was of 6.7×10^{16}, while the generated

[1] Tritium decays β^- with a half-life of ∼12d.

neutron bunch had a temporal structure of ∼300ps. The maximum energy of the neutrons was ∼4MeV [86]. Table-top photoneutron sources are a promising technology for applications. Current research is aimed at enhancing their performance by optimizing converter geometry, employing efficient converter materials and optimizing the energy distribution of the electron bunch. Furthermore, the upcoming high repetition kHz lasers could help to increase the neutron flux.
As a last issue concerning the possibilities explored for converter design, is noteworthy to mention the experiment conducted by Brenner and colleagues, who employed a bilayer converter constituted by 1mm of copper on the front side (i.e. the one that "sees" the impinging ions) and 4mm of lithium [15]. In particular, neutron production from the above described converter and from a 2cm thick lithium block was tested, using the same ion spectrum. According to experimental results, the presence of copper, which generates neutrons via the ^{63}Cu(p,n)^{63}Zn reaction, results in an increase of the neutron yield, along with an enhanced stability of the neutron energy spectrum against shot to shot variations. This experimental scenario will be further discussed in section 4.6.4.

Finally, as regards the maximum neutron energies obtained in experiments of laser-driven neutron sources, it is related to the maximum kinetic energy of the incident ions via the Q-value of the occurring nuclear reaction (see section **??** for further explanation). Therefore, neutrons obtained using mechanism such as BOA or RT reach energies of ∼150MeV, while TNSA neutrons have maximum energies of 35-40MeV.

The result of this study is summarized in table 2.4.

2.3.2 Analytical methods and numerical investigations

Because of the physical complexity of laser-driven neutron sources, experimental research on the topic is supported by the design and application of increasingly refined theoretical methods. A good deal of papers present in the literature is consequently devoted either to the development of such tools or to their application for the description of laser-driven neutron sources. The major theoretical methods that can be found in the literature can be grouped into three categories:

1. Particle-in-cell (PIC) methods for the simulation of the interaction be-

Table 2.4: *Summary of the main features of laser-driven generation experiments reported in the literature.*

Acceleration schemes	TNSA, BOA, RT
Target material	For protons: CH_2, polystyrene, mylar, (Al, Au, Cu)+ H rich contaminants For deuterons: deuterated polystyrene, CD_2, D_2O flow
Target thickness	hundreds ofμm 1mm
Laser pulse duration	40fs - a few ps
Laser energy delivered on target	mJ - 400J
Distance between pitcher and catcher	$\sim$5mm
Converter material	For ion conversion: Li, LiF, Be mainly Au, W, Cu
Converter thickness	0.5mm - $\sim$2cm
Maximum energy of neutrons	TNSA$\sim$40MeV, BOA or RP$\sim$150MeV, photoneutrons$\sim$4MeV
Maximum neutron flux in forward direction	10^{7-9}n/s

tween laser and pitcher target. These simulations provide information concerning the whole ion-generating process, such as the ion energy spectrum and the trend in time of the efficiency of conversion of the laser energy into kinetic energy of the ions and electrons.

2. Montecarlo methods for the simulation of ion transport and neutron generation inside the converter material. The outcome of the process is a prediction on the angular and energy spectrum of the generated neutrons.

3. Relatively simple numerical calculations commonly employed for making estimates or general predictions on the outcome of experiments.

As regards PIC simulations of laser-target interaction, the most diffused codes are *OSIRIS*, *EPOCH* and *piccante*. Commonly, the results of two-dimensional

and not three-dimensional simulations are reported, due to the large computational cost of the latter.
Apart from "standard" PIC simulations aimed at gaining information about the ion acceleration process, specific applications of this tool can be found in the literature. In particular Petrov and colleagues have studied the impact of contaminants on laser-driven ion acceleration using 2D particle-in-cell simulations [87]. The target is a bilayer of aluminium and CD plastic, hosting a proton-rich contaminant layer on its rear side. The idea is to individuate a critical condition which distinguishes the regimes of protons acceleration and protons+deuterons acceleration by varying the contaminant layer thickness and the laser fluence, i.e. the laser energy per unit area. The investigation indicated that for laser fluences smaller than $1\mathrm{J/cm}^2$ the contaminant layer on the rear surface inhibits deuteron acceleration, while in the opposite case deuterons and heavier ions can be successfully accelerated. Therefore in the latter case the target could be employed without resorting to cleaning of the proton contaminant layer.

Many codes are available to perform Montecarlo simulations of laser-driven neutron sources predicting the characteristics of the neutrons generated in a converter. The most diffused are Geant4 (GEometry ANd Tracking) [86, 88], FLUKA (FLUktuierende KAskade) [79] and MCNPX (Monte Carlo N-Particle Transport Code) [81, 89]. None of the three aforementioned codes is prevalently used. Other possibilities are PHITS [4] and DOWNSPEC [13].
Montecarlo simulation tools, besides being employed to gain information on the neutron angular and energy spectra, are also useful for design optimization. For instance, in literature the use of MCNPX (Monte Carlo N-Particle eXtended, an enhanced version of MCNPT) is reported for the optimization of the directionality of an epithermal neutron beam emerging from a moderator assembly [89].

Numerous theoretical works include simulations of the whole process of neutron generation, from the laser interaction with the target to the energy and direction of emission of the neutrons [10, 14, 77, 90]. This is made possible by the coupling between PIC and Montecarlo codes. More precisely, the ion energy spectrum produced by the former is fused as an input to the latter. The strong point of this approach is that, since PIC simulations allow a lot of parameters to be varied, comprehensive parametric theoretical studies of neutron generation can be performed. In particular, quantities such as the laser peak intensity, laser pulse duration and thickness of both pitcher and catcher targets can be varied. The neutron yield and its angular distribution can be represented as a

function of these parameters [11, 63].

Lastly, a large set of analytical methods is reported in literature for performing simple investigations. These allow, for example, the determination of the maximum neutron energy or the computation of convolution integrals, providing the total neutron yield expected when ions with a certain energy spectrum impinge on a material with a given stopping power and cross section for neutron production [91].
For instance, in order to evaluate the overall ability of one material to produce neutrons, Higginson and colleagues [13] have proposed to look at the neutrons produced per incident proton at a given energy, as shown in Fig.2.12. This datum is actually more useful than the cross section alone, since it accounts for the slowing-down of protons in the material. This is, again, the result of a convolution integral, in this case between the differential cross section of the considered reaction in energy and the material stopping power.

Another interesting analytical tool for giving a rough estimate of the neu-

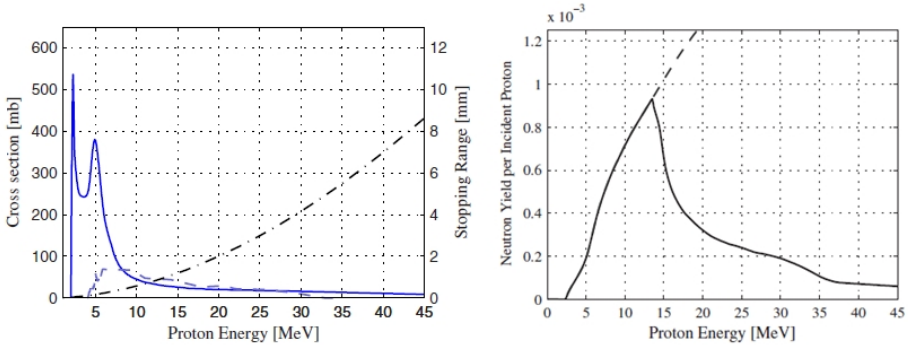

Figure 2.12: *On the left: On the left axis the cross-sections for the (p,n) reactions of ^{7}Li and ^{19}F are plotted vs incident proton energy. On the right axis the mean stopping range of protons in LiF is plotted (dashed line, data from SRIM code). On the right: Angularly integrated neutron production probability of protons of a given energy in LiF. The solid line is for 0.9 mm thickness, while the dotted line is for an infinite block of LiF. Adapted from [13].*

tron yield in a certain ion-target scenario has been reported by Zagar and colleagues [83]. The method relies an easy but effective way to compute the ion-neutron conversion efficiency ϵ_{xn}. Denote the characteristic length travelled by a particle by $\Gamma = 1/\Sigma$, where Σ is the macroscopic cross section for a certain

reaction and the range of the incident particle in the material R. As long as one only neutron-producing reaction is dominant and R is a few orders of magnitude smaller than any Γ, ϵ_{xn} can be expressed as:

$$\epsilon_{xn} = \frac{R}{\Gamma} \tag{2.13}$$

If the considered ion spectrum is not monoenergetic, the average energy weighted on the cross section of the ions contributing to the (ion,n) reactions in the considered energy interval is calculated. The value of Γ computed at this energy is then used to determine ϵ_{xn}. This approach was successful in predicting the measured neutron yield from the experiment.

Theoretical methods for the description of laser-driven neutron sources will be discussed in greater detail in chapter 3.

2.4 Open issues and goals of the thesis work

In order to define the motivations and goals of this thesis work I would like to give an overview of what as been discussed so far.
Chapter 1 has been devoted to the examination of conventional neutron sources, along with the discussion of their potentiality and limits. Furthermore, a set of selected applications of neutrons has been presented. In particular, the discussion was focussed on those applications in which laser-driven neutron sources could potentially become viable candidates for replacing current neutron-generation technology.
In chapter 2 the physics of laser-driven neutron sources has been thoroughly discussed as regards both laser-plasma interaction and neutron generation, with emphasis on ion-induced nuclear reactions. Moreover, many technological aspects of current laser-driven neutron generation have been pointed out and existing solutions for performance enhancement have been outlined. Eventually, an investigation of the state of the art in the field of laser-driven neutron sources has been presented, with focus on both experimental and theoretical aspects. In particular, the necessity of employing theoretical tools for the interpretation of experimental data or for experimental design optimization strongly emerged.

Based on information reported in the literature, the majority of the experiments performed so far have made use of PW-class lasers, while only a few authors employed TW-class compact lasers.

Although obtaining high fluxes of energetic neutrons might be of interest for certain applications, PW-class lasers are currently unable to sustain pulsed operation at a frequency acceptable for applications. Conversely, neutron sources based on compact or even table-top lasers can provide reduced size and radioprotection issues, low cost and repetition rates ranging from 0.1Hz to some kHz, without renouncing the very short duration of neutron pulses and to the concentrated neutron intensity in the forward direction.
Currently, compact neutron sources based on ion-induced nuclear reactions can produce $\gtrsim 10^7$n/sr in the forward direction [14]. Considering a sample placed at 5 cm distance from the source and a laser shot frequency of 0.1 Hz, a neutron flux of about 4×10^4n/cm^2/s can be estimated . This magnitude of the neutron flux is insufficient for applications such as fast neutron radiography. Fluxes suitable for this purpose ($\sim 10^7$n/sr) can be obtained using laser-driven photoneutron sources, even though the generation of high energy γ-rays represents a serious radioprotection issue.

All of this considered, in order to develope high-performance compact sources, it is necessary to perform an optimization of the overall scheme leading to neutron production. Since the physics involved in laser-plasma interaction and in ion-neutron conversion is utterly different, a pitcher-catcher scenario is preferred. Indeed, thanks to its modularity, it is possible to simulate the two aforementioned processes separately, using the output of the former as an input for the latter. These "multi-physics simulations" are realized employing suitable theoretical methods for the study of the processes occurring in the pitcher and catcher targets. In particular, PIC simulations are employed for simulating laser-driven ion acceleration, while a Montecarlo code is used for the quantitative analysis of neutron generation.

Although the use of such methods is widely reported in the literature, they have never been employed for the study of a compact neutron source in which a table-top laser is included. In this context, the optimization of the system can rely only partially on an increase in laser power, otherwise the compactness requirement wouldn't hold any more. Therefore, other parameters must be manipulated. The most straightforward idea is to properly choose the materials employed in the pitcher target and in the converter in order to increase the number of the produced neutrons and enhance their flux.
While many different and often sophisticated designs have been proposed throughout the years for the pitcher target in order to improve the ion generation process, the catchers used in experiments for laser-driven neutron generation are

quite standard (e.g. a few mm thick lithium or beyllium blocks or μm-thick metal foils). Only in one work the design of a bilayer converter including copper and lithium has been proposed [15]. The idea at the basis is to improve the overall neutron yield using a converter architecture that utilizes all of the ion beam content. Futhermore, despite their potential in terms of cross sections for neutron generation, medium Z materials such as copper, manganese and zinc have been barely taken into account as candidate converter materials.

All of this considered, this thesis work aims at theoretically investigating the feasibility of a compact laser-driven neutron source. In pursuit of the aformentioned goal it has been first and foremost necessary to develope reliable theoretical tools for the accurate description of the system under investigation. As noted above, due to the plurality of physical phenomena occurring in a laser-driven neutron source, it was necessary to develope a computational tool able to perform "multi-physics simulations", in which both laser-target interaction and neutron generation processes are included in an interdependent manner. In particular, the former is simulated using the particle-in-cell code *Piccante*, while the latter is studied with the Montecarlo code *Geant4*. This activity has been complementary to the study and application of simplied analytical methods for making predictions about the main characteristics of laser-driven neutron sources.
Based on the potentialities and limitations of the available theoretical tools for the description of a laser-driven neutron source, and according to the established goal of this thesis work, criteria for the selection of a case-study suitable for a benchmark have been identified in chapter 3.
The results of the selection process and of the benchamrk activity are reported in detail in chapter 4. In the same chapter also some studies on the dependence of the neutron yield on the converter material and thickness are illustrated. This is prodromic to the studies illustrated in chapter 5, in which optimized designs of compact laser-based neutron source are investigated. In particular, based on theoretical considerations, four scenarios of compact neutron source were conceived and tested by performing multi-physics simulations. The results of such study are eventually presented and discussed.
Lastly, in chapter 6 the conclusions of this work and its future perspectives will be highlighted.

Chapter 3

Theoretical tools for the simulation of laser-driven neutron sources

As anticipated in chapter 2, in the framework of laser-driven neutron sources experimental research goes hand in hand with theoretical activity. This latter is crucial for both developing theoretical models for the effective description of laser-driven neutron sources and supporting with simulations the design of new experiments. In this chapter the main theoretical tools employed for the simulation of laser-driven neutron sources will be presented. Among these, analytical methods will be addressed in section 3.1, while numerical tehniques will be discussed in section 3.2. In order to test the reliability of such tools in predicting the behaviour of a laser-driven neutron source, a benchamrk will be performed against experimental data taken from the literature. For this purpose section 3.3 will deal with some preliminary issues related to this activity, whose results will be extensively discussed in chapter 4.

3.1 Analytical methods

As a general concept, analytical methods applied to the study of a physical system allow making predictions on it through quite simple calculations. In the framework of laser-driven neutron sources, analytical methods are widely used

for performing estimates of physical quantities used for the description of ion acceleration and neutron generation. Considering that, in the framework of this thesis work greater attention will be devoted to the latter aspect, the analytical methods illustrated in the following are suitable for the study of ion-neutron conversion.

3.1.1 Evaluation of the maximum obtainable neutron energy based on the Q-value of the induced nuclear reaction

In its most general form a nuclear reaction involves a particle called *projectile* impinging on a usually stationary target. Depending on the characteristics of the nuclides involved in the reaction and on the physical parameters characterizing the interaction, different reaction mechanism such as the compound nucleus mechanism or direct interaction can take place. In any case, if the nucleus generated by the reaction is in its ground state, then the process can be modelled as a classical binary collision among two bodies.
As an example, let's consider the neutron-generating reaction illustrated in Fig. **??**), in which an incident ion (particle 1) with energy E_1 impinges on a stationary target atom (particle 2). Particle 3 is the neutron and particle 4 is the product particle. Angle θ is the direction of the emitted neutron in the laboratory system relative to the direction of the incident ion. By applying energy and momentum conservation equations to the system, a law expressing the neutron energy as a function of other parameters of the system is obtained. Under the hypotheses that $m_1 << m_2, m_4$, it takes a simlified form:

$$E_3(\theta) \simeq E_1 + Q + 2\sqrt{\frac{m_1 m_3}{m_4^2}\left(1 + \frac{Q}{E_1}\right)E_1}cos\theta \tag{3.1}$$

Here E_1 is the energy of the projectile, θ is the neutron emission angle with respect to the projectile incidence direction and Q is the Q-value of the reaction. The Q-value of a nuclear reaction is net energy released by the process and can be negative, positive or zero. In particular, a reaction with a positive Q value is exothermic, while a reaction with a negative Q value is endothermic.
The angular dependence in equation 3.1 implies that the emitted neutron gains maximum energy in the direction of the ion beam (i.e. for $\theta = 0$). The neutron energy then decreases with increasing emission angle, reaching minimum for θ=π.
If it holds that the projectile and the particle generated by the raection are

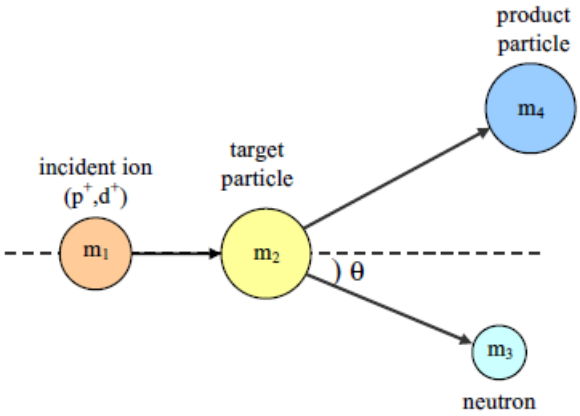

Figure 3.1: *Scattering geometry of a nuclear reaction in the laboratory frame.*

much lighter than the target nucleus (i.e. $m_1, m_3 << m_4$), then the maximum energy of the emitted neutron can be written as:

$$E_n^{max} \simeq E_{ion} + Q \tag{3.2}$$

where E_{ion} is the kinetic energy of the ion inducing the reaction. If a broad ion energy spectrum is considered, as in the case of TNSA ions, then E_{ion} refers to the kinetic energy of the most energetic ion impinging on the target. Therefore, according to eq. 3.2 the energy of the most energetic neutron can be computed as a sum of the kinetic energy of the most energetic ion present in the spectrum and the Q-value of the raection. When the Q-value of a reaction is negative, from eq. 3.1 it is possible to compute the *threshold energy* of the reaction, i.e. minimum kinetic energy that the projectile must carry in order to trigger the process. The threshold condition always occurs for θ=0, when the reaction products move separately in the forward direction. At θ=0 and if it is reasonable to consider that $m_1 + m_2 = m_3 + m_4$, then the threshold energy for a certain reaction can be written as:

$$E_{th} = |Q|\left(1 + \frac{m_1}{m_2}\right) \tag{3.3}$$

The Q-value and threshold energy for (p,n) and (d,n) reactions on lithium and beryllium have been already been commented in section 2.2.

3.1.2 Evaluation of the neutron yield and angular spectrum based on nuclear cross sections

While in the previous section a very easy equation for computing the neutron maximum energy has been presented, in this section a more advanced tool is required. Prior to the description of the actual analytical method, it is useful to remark some concepts related to cross sections. The *integral cross section* of a nuclear reaction is measured in barns (1b= 10^{-24}cm^2) and expresses the probability that a given particle reacts with a certain nuclear species. Other types of cross section exist:

- The *differential cross section in energy* $d\sigma/d\Omega$, which expresses the probability that, following the reaction, a particle is emitted within the solid angle $d\Omega$;
- The *differential cross section in energy* $d\sigma/d\Omega$, which expresses the probability that a particle is emitted with a certain energy over the entire solid angle.

The total cross section can be computed by integration of the differential ones.

Making use of the integral cross section for a neutron-producing reaction, it is possible to compute analytically the overall neutron yield. This is achieved by performing a convolution between the energy spectrum of the ions impinging on the converter target and the integral cross section for a certain nuclear reaction. Taking into consideration the general case of a non mono-energetic ion beam, the total neutron yield for a certain reaction nuclear reaction can be expressed as:

$$Y = \int_{E_i} f(E_i) \frac{N_{AV}}{m_w} \int_{E_i}^{0} \sigma(E_s) \frac{dE_s}{dE_s/d(\rho x)} dE_i \tag{3.4}$$

Where:

- $f(E_i)$ is the energy distribution function of the ions impinging on the target;
- N_{AV} is Avogadro's number;
- m_w is the molecular weight of the converter;
- σ is the integral cross section for the ion-neutron reaction;
- E_s is the transient energy of the ions during the slowing down;

- ρ is the mass density of the material;
- $dE_s/d(\rho x)$ id the mass stopping power of the converter.

This integral can be performed numerically, provided that all the data appearing in the equation are known. Notice that Eq.3.4 holds only if the converter is thick enough to stop all the ions impiging on it.
Proceeding analogously but using the differential cross section in energy $d\sigma(E_s)/d\,E_s$ instead of the integral cross section, a predictive energy spectrum for the generated neutrons is obtained.
In principle, the same procedure allows the determination of the angular spectrum of the produced neutrons, provided that the angular differential cross section $d\sigma(E_s)/d\phi$ is employed in the integral instead of the integral cross section. In this case, though, the result provided by the integral is a function of the relative angle between the incident ion and the outgoing neutron. Since the angular spectrum is normally referred to the emission angle in the laboratory frame of reference, a change of coordinates must be operated in order to obtain the final result.

3.2 Numerical methods

In the previous section some analytical methods applicable to the simulation of laser-driven neutron sources have been illustrated. If on the one hand such tools allow performing simple estimates with a reduced computational effort, they also have limits. Indeed, when the complexity of the simulated physics increases, the calculations become more and more complex, until when they cannot be solved with an analytical approach. Also in the specific case of laser-driven neutron sources, although some analytical methods are applicable, it is impossible to solve analytically the equations describing the physics of ion and neutron generation. In the following, the numerical methods suitable for describing the physics of laser-driven neutron sources will be illustrated.

3.2.1 The need for multi-physics simulations

The generation of laser-driven neutrons in a pitcher-catcher scenario is a process involving two temporally subsequent stages: the production of accelerated ions from a thin target and the generation of neutrons by nuclear reactions in a converter material. As illustrated extensively illustrated in chapter 2, the physics

lying under the two processes is utterly different.
For instance, in the former step we deal with laser-plasma interaction, which must be investigated using relativistic cinematics, while in the framework of neutron generation only particles with a maximum energy of tens of MeV are involved. Therefore the description can be non relativistic. Moreover, in the former stage the system under examination, i.e. the plasma, is constituted by a macroscopically large number of charged interacting particles, so a statistical approach must be adopted. This is not the case of the interaction of ions and neutrons in the converter material, in which the involved particles can be considered indepedent with a good degree of approximation.
This to name only a few of the differences between the physics of the processes occuring in a laser-driven neutron source. Simulation tools are commonly designed to work with a specific physics and offer the possibility to investigate at a certain degree of detail phenomena occurring in a given range of parameters. Therefore, it is clear that, in order to simulate the whole neutron generation process, we will need more numerical tools for simulation, each tailored on the physics under examination. All of this considered, the need for a multidisciplinary approach and multi-physics simulations naturally arises. In particular, the focus will be set on:

- *Particle-in-cell methods* for the simulation of laser-plasma interaction;
- *Montecarlo methods* for the simulation of the interaction of ions with matter and the generation of neutrons.

The strategy we will adopt to perform multi-physics simulations consists in employing the output results of the particle-in-cell simulations as an input for the Monte Carlo code. In this way, it is possible to exploit the powerful synergies between diverse simulation tools.

3.2.2 Particle-In-Cell simulations of laser-driven ion acceleration

Among the numerous numerical tools for the simulation of laser-plasma interaction in diverse regimes, the particle-in-cell (PIC) method has proven to be reliable for the investigation of non-linear processes in a collision-less plasmas. This definition encompasses fields much diverse from laser-driven neutron production, such as astrophysics, magnetohydrodynamics, magnetic reconnection, and microinstabilities in tokamaks. In the framework of laser-driven ion acceleration, PIC has been widely employed for making predictions about the

maximum obtainable particle energy or to study the effect on the accelerating performance of advanced target architectures. Only in relatively recent times PIC has started to be used for the simulation of laser-driven ion acceleration in the framework of laser-driven neutron sources.

The idea at the basis of the PIC scheme is the following. Being the plasma defined as an ensemble of a sufficiently large number of electromagnetically interacting particles, it is useful to introduce the quantity distribution function $f_i(\mathbf{x}, \mathbf{v}, t)$, which is defined as the number density per unit element in phase space. The subscript i refers to the i^{th}-population of particles (electron, protons, etc.). To solve the cinematics of the particles constituting the plasma one should solve the system constituted by:

- Maxwell equations, which govern the evolution of the electromagnetic field;
- The evolution equation of $f_i(\mathbf{x}, \mathbf{v}, t)$ which, if the hypothesis of collisionless plasma holds, is called relativistic Vlasov equation:

$$\frac{\partial f_i}{\partial t} + \mathbf{v} \cdot \frac{\partial f_i}{\partial \mathbf{x}} - q_i \Big(\mathbf{E} + \frac{1}{c} \mathbf{v} \times \mathbf{B} \Big) \cdot \frac{\partial f_i}{\partial \mathbf{p}} = 0 \tag{3.5}$$

  where m_i and q_i are the mass and electric charge of the particles belonging to the i-population, $\mathbf{v}$ is the particles' velocity, $\mathbf{p} = m\gamma\mathbf{v}$ is the momentum with $\gamma = \sqrt{1 + \mathbf{p}(t) \cdot \mathbf{p}(t)/m^2c^2}$, $\mathbf{E}$ and $\mathbf{B}$ are the electric and magnetic fields.

The PIC scheme is based on a combination of two methods: a Lagrangian approach for the study of the distribution function of a set of so-called *macroparticles* and an Eulerian approach for the computation of the value taken by the electromagnetic field, which is performed on a grid fixed in space. More precisely, the current density associated to the macroparticles (each macroparticle corresponds to a certain number of real particles) is deposited on the grid points, on which the electromagnetic field is then calculated. Successively the Lorentz force acting on each macroparticle is evaluated by interpolation and is used to solve the equation of motion. This procedure is repeated iteratively, i.e. the resolving strategy proceeds via successive steps in which, in turn, either the position of particles or the value taken by the electromagnetic field are updated.

In greater detail, the resolving strategy proceeds as follows. Firstly, we have seen that in the PIC description each particle species is regarded as the sum of a finite number of macroparticles:

$$f_i(\mathbf{x}, \mathbf{v}, t) \approx \sum_{j=1}^{M} f_j(\mathbf{x}, \mathbf{v}, t) \tag{3.6}$$

The written approximation in 3.6 tends to an equality the smaller is the volume $\Delta\mathbf{x}\Delta\mathbf{v}$ occupied by the macroparticle in the phase space. In order to reduce some numerical noise which arises if one considers point-like particles in the configuration space, they are allowed to assume a finite extended form, while remanining point-like in the velocity space (see Fig.3.2). The shape function S

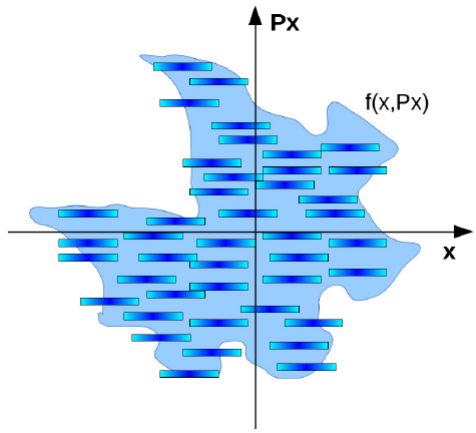

Figure 3.2: *2d representation of the extended macroparticles in the configuration space. From [6].*

describing the macroparticles becomes:

$$f_j(\mathbf{x}, \mathbf{v}, t) = A \sum_{i=1}^{n} \delta(\mathbf{v} - \mathbf{v}_i(t)) S(\mathbf{x} - \mathbf{x}_i(t)) \tag{3.7}$$

where A is a normalization constant. At this point, substituting 3.7 in 3.5 we can obtain the equation of motion for the macroparticles:

$$\frac{\partial \mathbf{x}_j(t)}{\partial t} = \frac{\mathbf{p}_j(t)}{\gamma_j(t) m} \frac{\partial \mathbf{p}_j(t)}{\partial t} = q \int S(\mathbf{x} - \mathbf{x}_j(t)) \Big[\mathbf{E}(\mathbf{x}, t) + \frac{\mathbf{p}_j(t)}{\gamma_j m c} \times \mathbf{B}(\mathbf{x}, t) \Big] d\mathbf{x} \tag{3.8}$$

Each macroparticle moves under the effect of the Lorentz force averaged over its volume and as if it had a mass m. Among the available PIC codes that can be used to study laser-plasma ion acceleration, in this work simulations will be performed with the code *Piccante*.

Throughout the years, PIC methods have proven to be reliable tools for the simulation of laser-plasma interaction in the ion energy range from zero to many tens of MeV. Despite this, they are still characterized by strong limitations, mainly related to their large computational cost.

In the first place, the computational cost of a PIC simulation depends enormously on its dimensionality: it is much more expensive to perform a 3D simulation rather than a 2D one. Furthermore, 2D geometry, which includes only the three electromagnetic field components E_x, E_y and B_z does not fully account for effects such as current filamentation, quasistatic magnetic field generation and angular distributions of the accelerated electrons [63]. Therefore, 3D is a requisite for performing realistic simulations of the system under study.
Besides dimensionality, the computational cost is a function of a large number of factors such as: the simulation time, the desired resolution in space and time and the density of the target layers. Combining suitably the above mentioned factors, it is possible to estimate the computational cost of a PIC simulation.
The onset of limitations on the target thickness and density can be explained as follows. In order to see which phenomena occur over a certain length scale in the simulated physical system, a sufficient number of grid nodes per unit of λ is normally arranged so as to map it. However, if the region is tiny, a huge number of nodes would be required to resolve it. For this reason extremely thin targets (thinner than $\sim$100nm) can be hardly simulated by the PIC code, unless paying a large computational price. An analogous problem arises when high density targets are employed. In fact, the higher the electron number density n_e in the target, the thinner the interaction "skin depth", i.e. the distance that a laser can travel in the overcritical plasma. When this region becomes too thin, a large number of grid nodes is required for achieving sufficient spatial resolution: this again leads to an increase in the computational cost.

In order to reduce the computational cost of PIC simulations, many strategies can be adopted, e.g. performing 2D instead of 3D simulations, varying the plasma density and thickness at constant mass thickness so that the laser interacts with the same number of particles within the plasma, etc. Naturally, the reduced computational cost of such "simplified" simulations come at the price

of a less realistic output. In this sense, the quality of a PIC simulation is always the result of a compromise between its computational cost and the quality of its output.

With regard to multi-physics simulations of laser-driven neutron sources, two actors contribute to the overall computational cost: the particle-in-cell simulation of laser-ion acceleration and the Monte Carlo simulation of ion-converter interaction. While the latter can be performed at a reasonable computational cost, the same does not necessarily hold for PIC. This means that PIC simulations are currentlly the limiting factor for the degree of accuracy of multi-physics simulations.

3.2.3 Monte Carlo simulations of ion-neutron conversion

Monte Carlo algorithms are numerical methods employed for finding solutions to mathematical problems which possess a large enough number of variables and, therefore, cannot be analytically resolved. The concept at the basis of the Monte Carlo scheme is the possibility to perform a sampling of a given probability distribution $f(x)$ using randomly sampled numbers. This means that a set of events is generated which are distributed according to the function $f(x)$. The solution obtained with a Montecarlo method is never exact, although its uncertainty decreases as the number of sampled events increases.
The Monte Carlo scheme is not necessarily the most convenient way to solve a problem if compared with analytical methods, since it requires a greater expense in terms of computational resources. Still, it becomes more and more advantageous as the complexity of the problem grows. This points out that the convenience of Montecarlo methods with respect to other techniques is a matter of balance between costs and benefits.
Let's consider, as an example, the analytical methods for obtaining informations on the characteristic of the generated neutrons illustrated in section 3.1. Despite providing an exact solution, it is evident that the calculations can become harder and harder as the system's complexity increases, due to the greater number of variables (e.g. cross sections, stopping power data) that need to be processed, leading to non-trivial numerical integrations. This is the reason why in the framework of this thesis we will rely mainly on the Montecarlo method for simulating the interactions of the accelerated ions inside the converter material and for obtaining information about the characteristics of the generated particles. Analytical methods will be employed to perform calculations, which

will serve as comparative data to assess the grade of agreement with the output of Montecarlo simulations.
Among the available Montecarlo codes that can be used to study radiation interaction with matter, in this work simulations will be performed with the code *Geant4*.

General features and structure of the Geant4 toolkit

Geant4 is a toolkit for the simulation of the interaction of particles in matter. It includes the tools for the definition and management of all the aspects that must be implemented to perform a simulation: the geometry, the employed materials, the required physics, the characteristics of the shot primary particles, the tracking of particles, the management and exporting of the results.
The physical processes included in the code cover a large range of phenomena (e.g electromagnetic, hadronic and optical processes) and span an extremely large interval of energies (from fractions of eV up to several PeV). Moreover, the properties of a large set of particles and materials are comprised. Due to its extreme flexibility Geant4 is employed in a wide variety of settings and its areas of application include the simulation of particle detectors, accelerators and high-energy physics.

Geant4 is written in C++ and, as it was released to public in 1998, it was the first Montecarlo code to employ object-oriented programming [92]. The advantage of object-oriented programming is that it allows the definition, in the code architecture, of a uniform interface and common organisational principles, hence facilitating the tool management and expansion (e.g. when new physical models are added). This simplification is obtained by means of class abstraction: an *abstract class* acts as intermediary for the creation of a concrete class defined by the user, that will inherit all the properties of the abstract class. In this way the user can assemble his/her program with components either provided by the code or self-supplied. This is also why Geant4 is said to be a *toolkit*, unlike other Montecarlo simulation tools designed for the same purpose (e.g. FLUKA, MNCPPX, etc.).
The abstract classes of Geant4 are classified into 17 main categories related by a fixed net of dependencies (see Fig. 3.3).
Geant4 provides the abstract interface for eight user classes:

1. ***G4VUserDetectorConstruction*** for setting the geometry and the materials of the simulated objects.

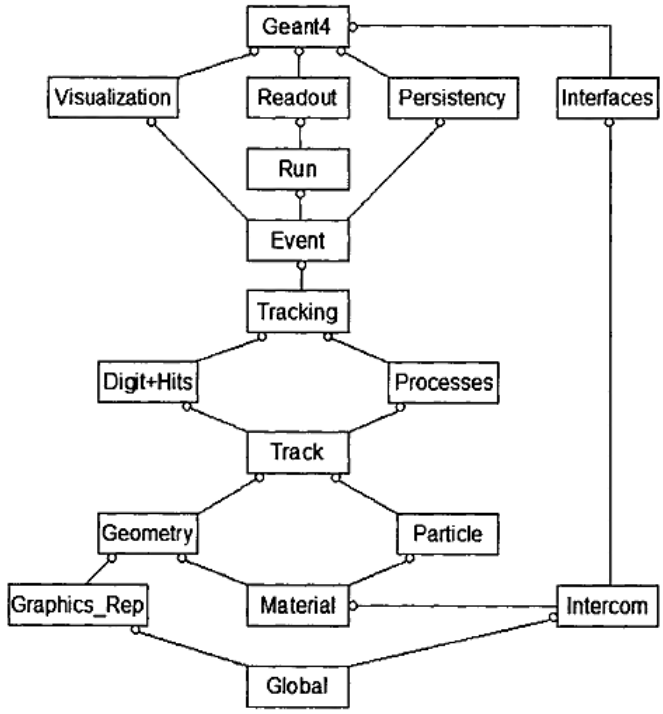

Figure 3.3: *Geant4 class category diagram.*

2. ***G4VUserPhysicsList*** for selecting the particles involved in the simulation and the desired physical models.

3. ***G4VUserPrimaryGeneratorAction*** for generating the primary vertices and particles;

4. ***G4UserRunAction*** for actions at the beginning and end of every run;

5. ***G4UserEventAction*** for actions at the beginning and end of every event;

6. ***G4UserTrackingAction*** for actions at the creation and completion of every track;

7. ***G4UserSteppingAction*** for managing the behaviour at every step;

8. ***G4UserStackingAction*** for managing the access to the track stacks (these are related to the priority of processing of each event occurring in the material).

Only the first three classes must be concretely implemented and instantiated, since for these Geant4 provides no default behaviour.

The physics of Geant4 for low-energy neutron generation

As pointed out in the previous paragraph, Geant4 contains a large variety of complementary and sometimes alternative physics models covering the physics of photons, electrons, muons, hadrons and ions in a wide range of energies.
Due to the large number of reactions accounted for in the toolkit, a particle *in flight* (i.e. moving in the material between two subsequent interactions) will be subject to many competing processes. Since the particle proceeeds in steps, the problem turns into determining what limits the step and also how to modify the particle parameters if it is not "killed" in the interaction.
Let's consider a particle in flight: on average it will undergo an interaction after having travelled a distance equal to its mean free path λ, which for an isotope i present in a weight fraction x_i in a material of density ρ possessing a cross section σ_i for a specific reaction can be expressed as:

$$\frac{1}{\lambda} = \rho \sum_i (\frac{x_i \sigma_i}{m_i}) \tag{3.9}$$

If we define a parameter n_λ as

$$n_\lambda = \int_0^l \frac{dl}{\lambda(l)} \tag{3.10}$$

where l is the distance covered by the particle, the probability of the particle to survive over a distance l will be P(l)=e$^{-n_\lambda}$. n_λ is computed at the beginning of each event as $n_\lambda = -\ln(\eta)$, where η is a random number between [0,1] sampled from a homogeneous distribution. n_λ is computed for each competitive process on all the present materials and the process which returns the smallest distance is selected and its post step action is invoked. If the particle is killed in the interactions, secondary particles are generated; otherwise the story of the particle continues and the iteration is repeated after having decremented n_σ by an

amount corresponding to the travelled step length.

Having understood the way in which Geant4 manages the competition among different physical processes, the physics encompassed by the toolkit will now be illustrated. In Geant4 five types of physical processes are considered:

1. **Optical physics**
   This physics deals with optical photons, i.e. photons whose wavelength is much greater than the typical atomic spacing ($\simeq$ 10nm), corresponding to energies below 100eV. This class is useful for the simulation of the optics of scintillators and Cherenkov detectors and the relates light guides.

2. **Decay physics**
   This physics is implemented in Geant4 by the class *G4Decay*, which chooses the decay time by means f the algorithm illustrated above and the decay mode according to the branching ratios of the particle, which are normally included in the code. Many models are available for determining the characteristics of the emitted secondaries.

3. **Photon/lepton-hadron physics**
   This physics includes photonuclear and electronuclear reactions, which are handled as hybrid processes which require both hadronic and electromagnetic models for their implementation.

4. **Electromagnetic physics**
   The electromagnetic physics included in Geant4 provides models for phenomena such as ionization, Bremsstrahlung, single and multiple scattering of charged particles, low-energy photon and charged particles interactions. In particular Geant4 provides two models: the *standard* EM package for particles with energies above 1 keV and the *low-energy* EM package for interactions at energies down to 100 eV.
   In Geant4 charged particles' energy loss is attributed to ionization and Bremsstrahlung. To be more precise, for energetic particles it is modeled as a discrete process in which secondary electrons and Bremsstrahlung photons are generated, while for low energy transfers the process is treated as continuous. Notice that, since Geant4 imposes that the cross sections for interaction must be approximately constant along the particle's step, thus the length of the step must be chosen accordingly.
   In the case of charged hadrons interacting with matter, Bremsstrahlung can be neglected, hence only ionisation is considered in the electromagnetic physics. This is implemented by the class *G4hIonisation* for ions

with unitary charge, by the class *G4ionIonisation* for ions with charge greater than one. Some useful models included in these classes are [93]:

- *G4BetheBlochModel*, which implements Bethe-Bloch stopping model and is valid for protons with T>2MeV;
- *G4BraggModel*, which implements the physics of the Bragg peak for protons and is valid for protons with T<2MeV;
- *G4BraggIonModel*, which implements the physics of the Bragg peak for alpha particles and is valid for alpha particles with T<2MeV;

With regard to the interaction of photons in matter, the main processes included in Geant4 are photoelectric effect, Compton scattering and pair production. [94].

5. **Hadronic physics**
Geant4 proves to be an extremely flexible tool for the simulation of hadronic interaction. In fact it provides numerous physical models apt to this scope, each valid over a well-defined energy range. As a whole, these models cover a wide range of energies, allowing the study of extremely diverse phenomena such as neutron transport and high energy physics. However, in a single application only a small part of the energy range might be needed, therefore the user must choose the physical model suitably in terms of physics and CPU performance. The models for hadronic interaction offered by Geant4 are designed to conserve energy, momentum and the majority of quantum numbers. They can be grouped into two main categories:

- *Theory-driven models*, in which the cross sections employed in the simulations are evaluated using theoretical formulas. Currently the following models are included:
  - *Fritiof model* (FTF) model
    It is used for the simulation of hadron-nucleus or nucleus-nucleus interaction in high enrgy physics. It assumes that all hadron-hadron interactions are binary reactions.
  - *Quark-Gluon-String-Parton* (QGSP) model
    It is used in high energy physics.
  - *Bertini intranuclear cascade* (BERT) model
    It handles the interactions of incident hadrons up to 10 GeV. In this model interactions are described in terms of particle-particle

collisions. A cascade of hadrons inside the nucleus is generated. In the last stage of the cascade the model provides the physics for nuclear evaporation, which takes place as long as the excitation energy is large enough to remove fragments from the nucleus.

  - *Liége intranuclear cascade model* (INCL++)
    This model was developed for the study of nuclear spallation reactions, hence it is suitable for usage at energies of some hundreds of MeV. It includes the physics of the intranuclear cascade combined with evaporation model and allows the use of light ions (A from 2 to 18 included) as projectiles.
  - *Binary cascade* (BIC) model
    This model is alternative to Bertini cascade for energies lower than a few GeV. In fact it is valid for protons and neutrons with incident kinetic energy below 3 GeV, pions with $E_{kin} < 1.5$ GeV and light ions with E_{kin} <3 GeV/A.

- *Data-driven models*, in which the cross sections employed in the simulations are taken from data libraries. Data-driven models are considered the best option for modelling, provided that experimental cross section data offer sufficient coverage. When data are not available from the libraries theory based approaches are employed to extract missing cross-sections from the measured ones or, at high energies, to predict these cross-sections.
  Data-driven models in Geant4 are mainly related to neutron and proton-induced isotope production, and with transport of neutrons at low energies.
  The data required for simulations are taken mainly from the ENDF/B-VII (Evaluated Nuclear Data File) library [94–96] and TENDL [97] data library when the experimental data are not available. These latter are generated through the TALYS nuclear model code.
  In the following the main data-driven models offered by Geant4 are listed.

  - *High precision model* for low energy charged particles interactions
    This data-driven model simulates the inelastic interactions of hadrons with kinetic energies up to 200 MeV. Since theoretical nuclear models fail in predicting cross section in this energy range and in order to provide accurate modelling, all the data necessary for simulation are taken from data libraries. The model is

implemented in the *G4ParticleHPInelastic* class [94].

– *High precision model* for low energy neutron interaction
This model describes the interactions of neutrons with kinetic energies from thermal up to 20 MeV. It is strongly recommended to activate this model, also in parallel with other hadronic models, when performing simulations with neutrons in this energy range, otherwise the toolkit could provide unreliable results [94, 95]. In particular four models are included in this set: radiative capture, elastic scattering, fission and inelastic scattering. The model is implemented in the *G4NeutronHP*.

When implementing the relevant physics for the scenario of interest, the user can choose to develop his own physics list class adding single components provided by the toolkit, or can exploit pre-compiled physics Lists which cover typical cases [93]. Drawing the attention onto hadronic processes, the main pre-compiled physics lists are:

- *G4HadronPhysicsFTFP BERT HP*
In this physics list the FTF and BERT models control the inelastic hadron-nucleus processes, while the package NeutronHP provides elastic, inelastic, capture and fission processes at energies below 20 MeV.

- *G4HadronInelasticQBBC*
This physics list is analogous to the previous one, apart from the fact that inelastic hadron-nucleus processes are also handled by the BIC model for energies ranging from 0 to 1.5 GeV.

- *G4HadronPhysicsINCLXX*
This physics list is recommended for simulating the spallation reactions.

- *G4HadronPhysicsQGSP BIC HP*
In this physics list the QGS, FTF AND BIC models control the inelastic hadron-nucleus processes, while the package NeutronHP provides elastic, inelastic, capture and fission processes at energies below 20 MeV.

- *G4HadronPhysicsQGSP BIC AllHP*
This physics list is analogous to the previous one, apart from the fact that it contains also the subclass *G4ParticleHPInelastic* which simulates the interaction of low energy charged particles.

In the frame of laser-driven neutron sources protons and neutrons posses energies ranging from 1 to a few tens of MeV, hence we will use *G4HadronPhysicsQGSP BIC HP* and *G4HadronElasticPhysicsHP*.

3.3 Benchmarking the codes against experimental data of laser-driven neutrons from literature: preliminary discussion

In the previous sections the numerical methods employed for the simulations of laser-driven neutron sources have been illustrated and their main features outlined. Moreover, the potentiality of codes' integration for performing multi-physics simulations was highlighted. In the literature on laser-driven neutron sources multi-physics simulations are employed in theoretical works, while it was impossible to find papers attesting their use for reproducing experimental data. Conseguently, in order to test the quality of our integrated simulation tool, a benchmark of our codes against experimantal data of laser-driven neutrons taken from literature will be performed. Its results will be described in chapter 4.
In this section some issues preparatory for the benchmarking activity will be addressed: in particular the focus will be set on the definition of criteria for the choice of an article suitable for the benchmark and on the outcome of the selection process.

3.3.1 Data selection criteria

In this section criteria for the selection of the article to be benchmarked will be chosen. To this scope, it is worth remarking that the final goal of the present thesis work is to assess whether multi-physics simulations of laser-driven neutron sources can produce reliable descriptions of such systems. As mentioned earlier in this section, the available theoretical methodes are particle-in-cell and Monte Carlo simulation codes, along with analythical methods. Taking this into account, it is possible to proceed with the definition of selection criteria.

In the first place, the architecture of the assembled PIC + Monte Carlo code employed for performing multi-physics simulations requires that the ion acceleration ions and neutron production occur separately in space and subsequently in time. This is equivalent to saying that the experiment to be reproduced must

involve the production of neutrons in a pitcher-catcher configuration. Indeed, in a bulk neutron generation scheme, ion and neutron generation occur simultaneously and in the same material. Therefore, experiments performed in this latter scheme must be excluded from the candidates for the benchmark.

Secondly, since the goal of the benchmark activity is to test the quality of the illustrated simulation tools for performing multi-physics simulations, the requirement of reproducibility is indispensable. Among the existing ion acceleration schemes, TNSA is the most investigated and well understood. Furthermore, as explained in section 2.1.2, many different acceleration mechanisms diverse from TNSA may originate during the interaction of high intensity laser pulses with matter and each of these may dominate the physics of the interaction depending on the experimental configuration. In any case, a TNSA component is always observed. All of this considered, the experiment to be benchmark must involve the production of neutrons obtained from ions accelerated with a TNSA scheme.

A further point concerns the nature of the accelerated ions. As mentioned in section 2.2, in a TNSA scheme the accelerated ions are light species, i.e. protons, deuterons or carbon ions. The acceleration that each ion undergoes is proportional to its charge-to-mass ratio, hence protons are accelerated to the highest energies if compared with other ions on an equal footing. For this reason it was chosen to select an article in which only protons are accelerated.
This choice has been motivated also by a practical issue. The ions accelerated in a TNSA scheme belong mainly to the contaminant layer present on the rear surface of the target. This layer is rich in protons and hydrocarbons. It forms spontaneously due to the contact with gases present in the atmosphere. Things would be different if the accelerated ions were deuterons: in this case it is necessary to deposit a deuterated layer on the rear surface of the target and keep it under a protected atmosphere to avoid the formation of the hydrogenated layer. If this operation is not carried out with sufficient accuracy, a double layer of deuterons and protons forms and protons are preferentially accelerated by the TNSA mechanism.

Concerning computational resources, in section 3.2 it has been pointed out that currently PIC simulations are the limiting factor for the degree of accuracy of multi-physics simulations. Having in mind to perform a 3D PIC simulation of laser-ion acceleration with the same parameters of the benchmark article, a constraint has been imposed on the laser pulse time duration, which should be smaller than 100 fs. This number was compatible with the available computa-

tional resources. As a final point, it is worth stressing that articles candidate to the benchmark should provide as many experimental details as possible. In fact, the larger the quantity of available data, the more effective the benchmarking will be.

3.3.2 Outcome of the selection process

First of all, it is worth stressing that, while the literature concerning laser-driven ion acceleration is very rich and diversified, papers about experiments of laser-driven neutrons do not appear in large numbers. This sheds light on the state of progress of the two lines of research: whereas the field of laser-driven ion acceleration has been widely investigated since the '90s both theoretically and experimentally, the study of laser-driven neutronsources, above all by Ti:Sapphire technology, is still in its early days.

After submitting the candidate papers to the selection process many have been excluded, mainly because not compliant with computational restrictions. This is coherent with the fact that, as already pointed out in section 2.3, the vast majority of experiments reported in the literature have been conducted at large laser facilities, employing highly energetic laser pulses with duration between a few hundreds of fs and 1 ps, while only in a few experiments laser pulses of duration shorter than 100 fs have been used.
Considering also the other requirements (pitcher-catcher scheme, TNSA, only protons being accelerated), the selection process has led to the individuation of one only candidate. In the following chapter, the possibility to perform a simulation of the experimental laser-ion acceleration process will be discussed in the light of the critical issues related to PIC methods reported in section 3.2. If the feasibility of a PIC simulation of the selected experiment will be assessed, a multi-physics study involving integrated PIC and Monte Carlo simulations will be performed.

Chapter 4

Benchmarking the codes against experimental data of laser-driven neutrons

The present chapter is devoted to the description of the benchmarking activity conducted in order to assess the reliability of the theoretical tools discussed in chapter 3 for the simulation of laser-driven neutron generation. The experimental data will be presented in detail in section 4.1. The following sections (4.2, 4.3, 4.4) will present respectively some analythical results, the results of the performed PIC simulations and the hypotheses adopted in the Geant4 Monte Carlo simulation. The results of the benchmarking activity on the Monte Carlo code Geant4 are presented in section 4.5. Finally, the sensitivity of the results to the temperature on parameters such as the ion temperature and the converter material and thickness will be discussed in section 4.6.

4.1 Description of the selected experiment

The selection process described in chapter 3 has resulted in the selection of an article by Zulick and colleagues [14] in which a laser-based neutron generation experiment performed at the HERCULES Laser Facility of the University of Michigan is described. The main experimental parameters are reported in table 4.1.

Table 4.1: *Summary of the main parameters used by Zulick et al. [14].*

Laser	Pulse energy=1.1 ± 0.4J at 0.01 Hz Intensity=$2 \times 10^{21} W/cm^2 s$ Pulse duration=40fs
Acceleration mechanism	TNSA
Target properties	Parylene, 100nm thick
Accelerated ions	Protons
Maximum proton energy	10.27MeV
Catcher properties	LiF (lithium fluoride), 8.5mm thick
Reactions	$^7Li(p,n)^7Be$, $^{19}F(p,n)^{19}Ne$
Q-values	-1.64MeV, -4.02MeV

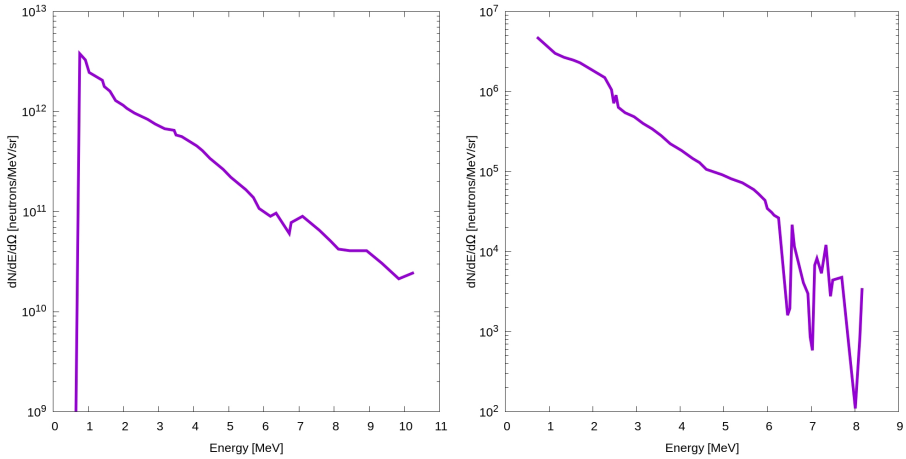

Figure 4.1: *Experimental ion (left) and neutron (right) spectra along the target normal direction.*

In Fig. 4.1 the measured ion and neutron spectra are reported. Additional information concerning the results are:

1. The flux in the forward direction is 6.7 ± 3.7 times higher than the flux at 90°;

2. The observed neutron flux (expressed in n/sr) in the forward direction is equal to $1.0 \pm 0.5 \times 10^7$n/sr.

In the experimental configuration adopted by Zulick and colleagues the primary neutron diagnostics are neutron time-of-flight (nToF) detectors constituted by an organic scintillators coupled to photomultiplier tubes. Two detectors with an active surface of diameter 16cm were placed at distances of 2.75 and 3.28 m from the target, while one with active surface diameter of 35.5cm was located at 9.45 m. All the nToF detectors were located in the forward direction within a 15° cone.
Due to both the complexity of simulating in detail the experimental setup and also to the lack of many information concerning it, some simplifying hypotheses have been adopted in Geant4 simulations:

1. The experiment is performed in vacuum, but no vacuum chamber was modelled, hence the container's walls do not influence the studied phenomenon;

2. All the active volumes defined for gathering data about the neutrons' energy work with a unitary efficiency, i.e. all the neutrons with the stated characteristics are registered and none is lost.

3. Being the isotopic composition of the LiF converter unspecified, the material was assumed to have natural isotopic composition. Notice that the lithium and fluorine isotopes interesting for neutrons production represent the 92.41% and 100% of the respective elements as present in nature. Therefore the above hypothesis would hold with very good approximation even in the case of an enriched converter material.

4. The experimental data provided by the article are unclear on the solid angle of emission of both protons and neutrons. This hinders the possibility to compute an absolute number for the ions arriving on the catcher and for the neutrons produced. For this reason, based on the fact that in the experiments detectors are said to cover a solid angle embraced by a cone of aperture 15°, this value has been chosen as a reference for both proton and neutron emission. Although this is arbitrary, to set the same solid angle of mission for both, allows the computation of an overall neutron yield.

4.2 Estimates based on analytical methods

As illustrated in section 3.2.3, analytical methods are extremely useful for performing simple estimates of some characteristic quantities of the system under investigation. In the framework of the benchmark activity, quantities relevant for the evaluation of the source performance have been evaluated. These include the maximum neutron energy, the angular spectrum of the emitted neutrons and the neutron yield per shot proton.
In all cases, the ion spectrum incident on the converter material has been fitted with a line in a semilogarithmic scale (see Fig. 4.2). The exponential behaviour of the spectrum appears to be well described by a function $e^{-E/T} = e^{-0.51 \times E}$, where T is the so-called *ion temperature*. The exponential shape of the ion spectrum is characteristic of TNSA in a large energy interval (see section 2.1). The results of this activity are reported in table 4.2.

Table 4.2: *Comparison between experimental results and analytical estimates for some quantities relevant for the description of a laser-driven neutron source.*

Quantity	**Experimental datum**	**Analytical result**
$E_{p,max}$	7.2 ± 0.8MeV	8.63MeV
Neutron yield per proton	1.03×10^{-6}	3.5×10^{-4}
$\frac{Flux_{0deg}}{Flux_{90deg}}$	6.2 ± 3.7	4

The maximum neutron energy has been evaluated using Eq. 3.2, considering the maximum ion energy and Q-value listed in table 4.1. The experimental value is slightly lower than the theoretical one. This can be explained considering the attenuation of the generated neutrons before exiting the converter material. In fact, a converter thickness of 8.5mm was adopted, which is much greater than the maximum range of the most energtic protons impinging on LiF (0,587mm). Therefore, almost all neutrons are created far from the converter rear boundary and need to pass through a certain depth of attenuating material before exiting the target.

With regard to the neutron yield per proton, this quantity expresses the number of neutrons emitted for ion impinging on the converter target and is

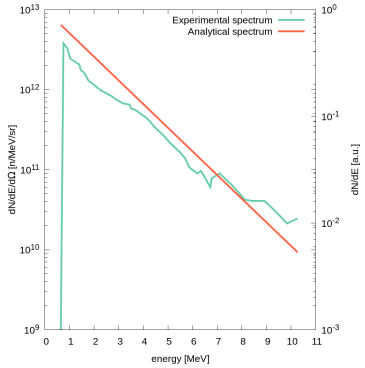

Figure 4.2: *Experimental ion spectrum reported by Zulick et al. [14] (in green) and fitted analytical exponential spectrum (in orange).*

therefore a direct measure of the efficiency of the proton-to-neutron conversion process. Mathematically speaking, it can be computed by means of equation 3.4, which is a convolution integral between the analytical form of the energy spectrum of the impinging protons and the cross section of the main proton-induced neutron-generating nuclear reactions evaluated at the actual energy of the decelerating ion. The cross sections for (p,n) reactions on ^{7}Li and ^{19}F is shown in Fig. 4.3. As it can be seen in table 4.2, the analytical value is about 100 times greater than the experimental one. However, it must be considered that, according to hypothesis 4 reported in the previous section, the experimental neutron yield has been computed considering a forward-directed emission direction, therefore accounting for only a small part of the neutron spectrum emitted over 4πsr. On the other side, the analytical value of the yield takes accounts for the neutrons emitted over 4πsr, which might explain why it exceeds the experimental. Furthermore, it must be considered that the analytical calculation was performed on lithium and not on its compound LiF, which tipically shows a lower neutron yield with respect to elemental lithium.

As a last point, the neutron angular spectrum of the generated neutron beam has been computed by numerically solving Eq.3.4 using the differential angular cross section instead of the integral one (see section 3.1.2). The result of this calculation is shown in Fig. 4.4. The angular spectrum has been computed under the following hypotheses:

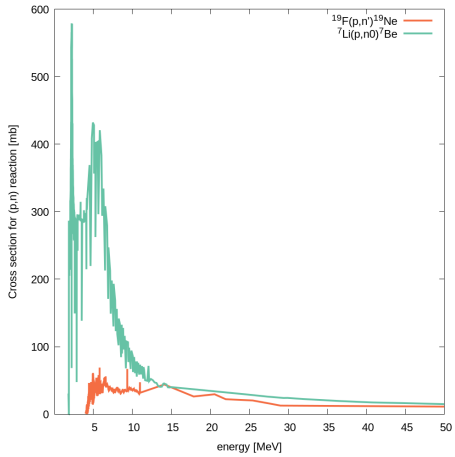

Figure 4.3: *Cross section for (p,n) nuclear reaction of ^{7}Li (in blue) and ^{19}F (in orange).*

1. ^{7}Li instead of LiF has been used, due to the unavailability of double-differential cross section data for ^{19}F.

2. The double-differential cross section data for ^{7}Li are available for the energy range 1.95-7 MeV. Therefore, the maximum ion energy was set to 7 MeV instead of the ∼10 MeV measured experimentally, while the lower cutoff of protons was set to 1.95MeV in this calculation.

From the angular spectrum in Fig. 4.4, a clear directionality of the beam is inferred. Althuogh no information about the angular spectrum of the emitted neutrons is provided in the article, it is reasonable to expect that, by not accounting for the most energtic ions, the analytical angular spectrum will be less forward-peaked with respect to the experimental one. Moreover, the presence of fluorine in the target, which has a smaller (p,n) cross section with respect to lithium (see Fig. 4.3) in the considered range of ion energies, leads qualitatively to a decrease in the overall neutron yield per shot proton.
From the angular spectrum displayed in Fig. 4.4, the value of the ratio $Flux_{0deg}$ $/Flux_{90deg}$ displayed in table 4.2 has been evaluated. From a comparison between the values of such ratio obtained experimentally and analytically, it can be seen that, though not identical, the two values are compatible if the experi-

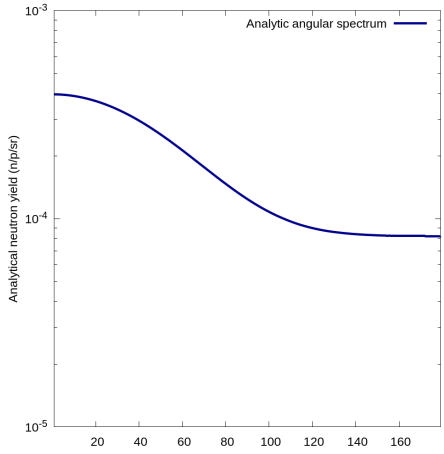

Figure 4.4: *Neutrons' angular spectrum.*

mental range of uncertainty is considered.

As expected, analytical methods proved reliable for giving a simple description of quantities which are of primary importance for the description of a laser-driven neutron source. The observed discrepancies can be attributed either to to two factors: on the onde hand, the lack of sufficient information about the experimental data unavoidably led to the formulation of hypotheses, which, though realistic and reasonable, do not guarantee faithfulness to reality; on the other hand, as regards the analytical form of the neutron spectrum, the lack of sufficient knowledge about the double-differential cross section on the whole energy range of interest, contributes to the observed discepancy.

4.3 Simulations with the Particle-In-Cell code PICCANTE

As explained in chapter 3, the feasibility of PIC simulations reproducing experimental data of laser-ion acceleration must be discussed in the light of the general critical issues related to PIC methods discussed in section 3.2. In this section, the feasibility of performing a 3D PIC simulation of the ion-acceleration process using the experimental data reported by Zulick and colleagues will be assessed. The value of the most relevant parameters for laser-target interaction

are listed in table 4.4.

Table 4.3: *Comparison between experimental results and analytical estimates for some relevant quantities.*

Laser parameters	Type: Ti:Sapphire Pulse energy=1.1 ± 0.4J at 0.01 Hz Intensity=$2 \times 10^{21} W/cm^2 s$ Pulse duration=40fs P-polarization λ=800nm Focal spot (FWHM)=1.3μm
Pitcher target	Parylene, 100nm $\Rightarrow n_e = 213 n_c$

According to the dat reported in table 4.4, the laser interacts with a 100nm-thick plasma, whose density is highly over-critical ($n_e = 213 n_c >> n_c$). As explained in section 3.2, small values of the target thickness along with high target density imply the need of high spatial resolution for resolving physical phenomena occuring over such short length scales. In particular, the target thickness corresponds to 0.125λ, where λ is the wavelength of the laser oscillating electric field. Since resolving phenomena occurring at the scale of the characteristic length λ is of interest, a sufficient number of grid nodes per unit of λ is normally arranged so as to map it. However, a huge number of nodes would be required to resolve a scale of 100nm. Analogously, the interaction of the laser pulse with such a high plasma density results in a skin depth of only 8nm. All of this considered, 3D simulations of the chosen experiment proved to be unfeasible due to large computational costs. However, it was decided to perform some preliminary and less expensive 2D simulations with "relaxed" parameters in order to individuate a scenario able to replicate in 3D the physics of the real system at a lower computational cost. For this purpose a set of 2D simulations have been performed varying the electron density n_e and the target thickness t under the constraint of constant mass thickness. The results of such investigation are reported in Fig. 4.5.

After this scan, it was chosen to simulate in 3D the most relaxed case, i.e. the one with n_e=$40 n_c$ and t=0.666λ. The main parameters of such 3D simulation

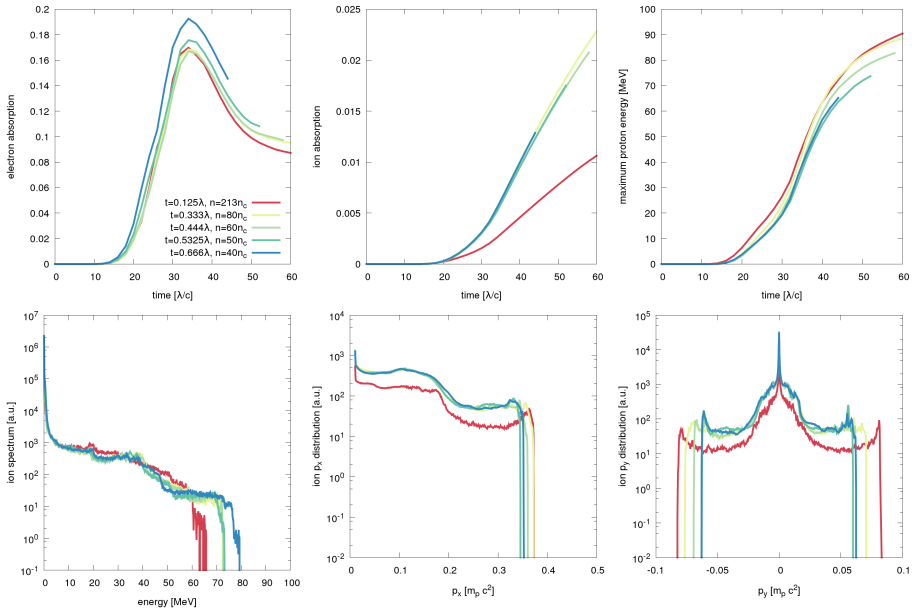

Figure 4.5: *Results of 2D PIC simulations performed with "relaxed" parameters. The lines in red correspond to the parameters of the real system.*

are listed in table **??**, while results are shown in Fig. 4.6 and 4.7.

Table 4.4: *Main parameters of the 3D PIC simulation.*

Laser parameters	Type: Ti:Sapphire $a_0 = 30$ Spatial resolution: $40pp\lambda$[1] Time duration of the simulation: $50\lambda/c$ Cost $\gtrsim$ 8000CPUh
Target parameters	$n_e = 40n_c$ $t = 0.666\lambda$
Pitcher target	Parylene, 100nm $\Rightarrow n_e = 213n_c$

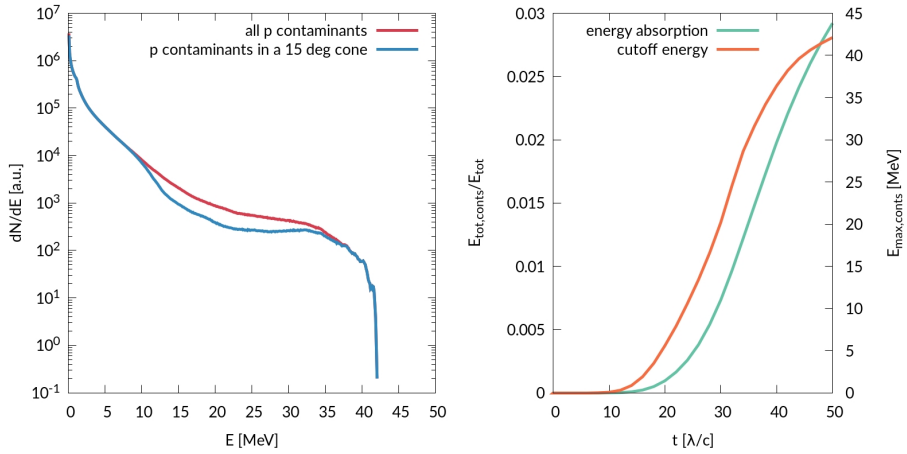

Figure 4.6: . *On the right: Energy spectrum for all the accelerated protons (red) and for those emitted in a cone of aperture 15° (blue). On the left: Progress in time of the fraction of the laser energy absorbed by the ions (green) and of the maximum ion energy (orange).*

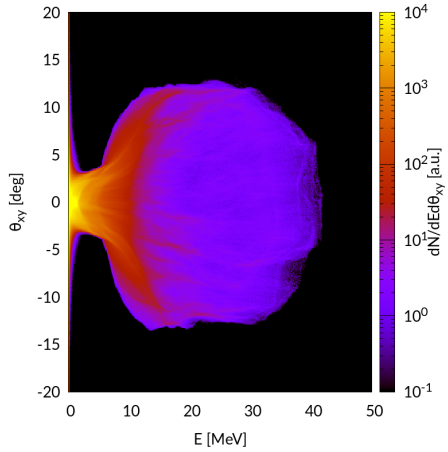

Figure 4.7: *Number of emitted protons according to energy and emission angle.*

[1] ppλ=points per λ, i.e. the laser wavelength.

As it can be seen, approximations have led to a huge overestimation of the maximum ion energy, which amounts to 42 MeV instead of ∼10MeV. This is justified by the fact that, although the laser passes through the same amount of matter due to the constant mass thickness requirement, in the real case it interacts with a much denser plasma.
The impossibility of performing a 3D PIC simulation at a reasonable computational cost hindered also the execution of a multi-physics simulation. However, it was possible to benchmark the Monte Carlo code against experimental data by fitting the ion spectrum provided in the article with an analytical exponential function (see Fig. 4.2).

4.4 Simulations with the Monte Carlo code Geant4

In order to be able to reproduce the neutron data measured by Zulick and colleagues in their experiment it is necessary to implement in Geant4 the whole configuration of the experimental setup, whose accurate description in Geant4 is crucial for obtaining reliable results. The most delicate aspects to be considered are:

1. The geometrical configuration;

2. The employed materials;

3. The setting of diagnostics, i.e. conditions set by the user on a particle type, position and/or momentum that, when satisfied, lead to the storage of selected information concerning the system and to the creation of output files.

Based on the experimental neutron diagnostics employed in the experiment (see section 4.1), besides recording the overall energy and angular neutron spectrum, the following diagnostics have been set for the record of neutrons' energy:

1. All the neutrons emitted in the half-space on the rear side of the converter, opposite to the ion beam;

2. All the neutron emitted in a cone of aperure 15°, i.e. the angle covered by the detectors in the experiment;

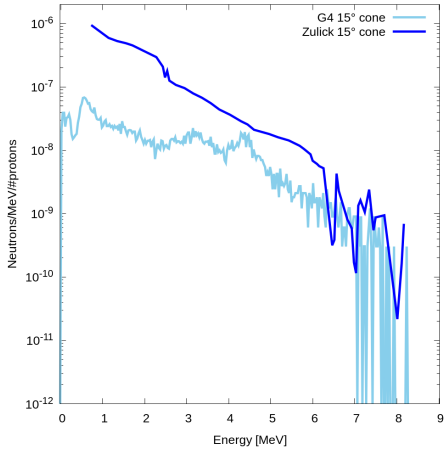

Figure 4.8: *Experimental and simulated neutron energy spectrum.*

3. All the neutrons reaching the detector with smaller diameter located 2.75m far from the converter.

This choice was motivated by the fact that in the article the ion and neutron spectra are said to be recorded in the forward direction, but it is not specified over which solid angle. Therefore, by placing diagnostics covering different solid angles it was possible to gather more informations on this aspect.
In the following section the results of the Geant4 simulation performed under the above-illustrated hypotheses are presented.

4.5 Discussion of results

In this section the results of the benchmark Monte Carlo simulation of neutron generation can now be presented. As a remark, remember that the energy spectrm used as an input to Geant4 is the analytical fit of the ion spectrum obtained experimentally.

In Fig. 4.8 and 4.9 the simulated neutron energy spectrum for neutron emission within a cone of aperture 15° is reported, along with the angular spectrum predicted by Geant4. The energy spectrum has been normalized dividing by the overall number of the ions impinging on the converter on a solid angle covered by a cone of aperture 15°. According to the plot, Geant4 reproduces very well

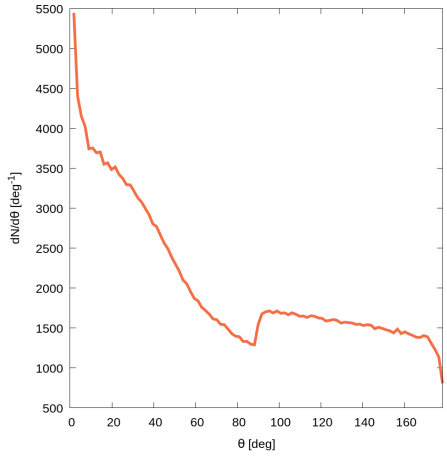

Figure 4.9: *Neutron angular spectrum predicted by Geant4.*

the cutoff energy of the emitted neutrons, but predicts a lower yield with respect to the experimental case, especially at low neutron energy. The overall neutron yield has been calculated from both experimental and theoretical results. This led, for an emission solid angle corrisponding to a cone of aperture 15°, to a value of $1,03 \times 10^{-6}$n/p for the experimental case, against 8.67×10^{-9}n/p for the numerical simulation. In conclusion, Geant4 underestimates the overall neutron yield by a factor of about 100. However, if instead of the value of the solid angle reported in hypothesis 4 in section 4.1 a value of 2π is considered, the neutron yield would be equal to $5,96 \times 10^{-7}$, i.e. the experimental data would be underestimated of a factor of 10. In absence of experimental details, both choices are legitimate. This aspect sheds light on the importance of performing simulations of experiments in which experimental data are reported in great detail.

Let's now analyse the simulated angular neutron spectrum on the righthand side of Fig. 4.9. The neutron beam appears to be highly forward-peaked. Although no experimental data on the emission angle has been provided by Zulick and colleagues, the directionality of neutrons produced by the nuclear reaction $^7Li(p,n)^7Be$ is a known and well-investigated property. This feature was evident also from the angular neutron spectrum computed analytically in section 4.2. A comparison between the two is shown in Fig. 4.10.

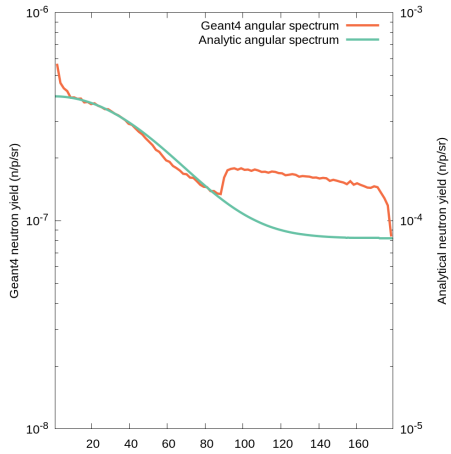

Figure 4.10: *Comparison between the neutron angular spectrum obtained analytically (in green) and the one predicted numerically by Geant4 (in orange).*

It can be seen that the two lines are very similar in shape, apart from the discontinuity predicted by Geant4 at an angle of 90°. This feature, not resolved by the analytical method, is generally present in angular spectra of laser-driven neutrons produced in a pitcher-catcher configuration. Its physical origin must be traced back to the geometry of the converter: usually the thickness of such target is quite small if compared to its other dimensions, therefore it is improbable that a neutron, which is normally produced far from the edges, travels an almost straight path parallel to the converter surfaces and exits the material st 90° with respect to the ion beam.
Furthermore, focussing on Geant4 data and comparing the obtained neutron yields at 0° and 90°, it is found that the yield at 0° is ∼5 times higher than the one at 90°. This datum is perfectly consistent with the experimental one, which amounts to 6.2±3.7.
Eventually, when comparing the two lines quantitatively, a discrepancy of 3 orders of magnitude in favour of the analytical data arises. Besides the considerations already reported in section 4.2 fr the analytical spectrum, further elements can be cnsidered. In the first place, it must be pointed out that the theoretical methods being compared, are based on the same input neutron energy spectrum, therefore any disagreement between the two cannot depend on factors related to the experimental data. One hypothesis is that the cross sec-

tions employed for the calculations in the two cases vary significantly. Indeed, Geant4 uses theory-based TALYS cross section data, while for computing the analytical spectrum, experimental data have been used. Furthermore, while in the analytical spectrum neutrons are recorded as soon as they are produced, in the Monte Carlo simulation the neutron is detected only once it has escaped the converter target. It is possible that some neutrons moderating inside lithium just stop inside the material.

In conclusion, Geant4 was succesful in predicting only some parameters relevant to the description of a laser-driven neutron source, e.g. the neutrons' maximum energy. Also the directionality of the beam and the depression of the neutron yield at 90° in the source angular spectrum were caught. However, significant discrepancies have been observed with respect to experimental data. As extensively discussed, such disagreement must be mainly attributed to the lack of clear and unambiguous experimental information. In order to perform a fair comparison, an article providing detailed data concerning the experimental setup should be considered.

4.6 Sensitivity of the results to the converter material and thickness

In order to achieve a better understanding of the phenomena occurring inside the converter during the ion-neutron conversion process, the experimental results obtained by Zulick will be tested against variations of the target thickness and material by means of simulations in Geant4. This analysis is performed also in preparation of chapter 5, where optimized schemes for compact laser-drivne neutron sources will be studied. Commonly, in experiments of ion-based laser-driven neutron sources, the criterion employed for the determination of the converter thickness states that the converter should be thick enough to stop the most energetic impinging ions [91]. Indeed, if the thickness of the converter is smaller than the range of the most energetic ions in that material, a part of the charge will be transmitted through the converter, therefore leading to an only partial exploitation of the potential for neutrons generation. On the other side an excessively thick converter would lead to a decrease in the neutron beam collimation and, hence, in the achievable neutron flux.
The experiment described by Zulick falls within the lattr case, since the LiF converter is equal to 8.5mm, while the range of the most energetic (10MeV) ions in that material amounts to only 587 μm.

In order to study the effect of the converter thickness on the neutron yield, a set of simulations in Geant4 have been performed, in which ions with a spectrum fitted by the article of Zulick et al. were made to impinge on LiF targets of growing thickness. The neutron yield as a function of LiF thickness is shown in Fig. 4.11 on the lefthand side. From the image it can be easily seen that the

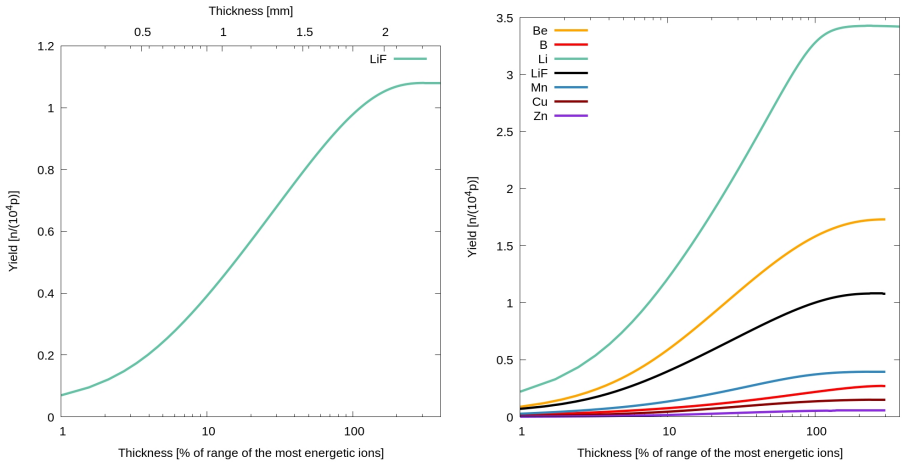

Figure 4.11: *Neutron yield in LiF (on the lefthand side) and other materials (on the righthandside) as a function of the converter thickness expressed in units of length (upper axis) and normalized to the range of the most energtic ions (lower axis).*

neutron yield increases with the converter thickness up to a thickness value corresponding to the maximum range of the most energetic ions, where the curve bents to form a plateau. Indeed, despite not being shown, the graph remains steady up to 8.5mm of LiF thickness. This behaviour is not a peculiarity of LiF. Indeed, using Geant4 it has been possible to record the same trend for a set of materials which are of interest in converter studies (see Fig. 4.11). An analogous theoretical study leading to similar results has been reported in literature by Yang et al. [82].

Already from Fig. 4.11 a classification of converter materials, limited to the specific case of the ion spectrum obtained by Zulick, can be drawn. In this context, the most efficient element for neutron conversion is lithium, followed by beryllium, lithium fluoride and, far below, by boron and the medium Z elements manganese, copper and zinc. It must be highlighted that Fig. 4.11 is referred to

materials with natural isotopic composition. This implies that for each element, more than one isotope could potentially contribute to the neutronic production. Besides the converter's thickness, the converter material is another relevant parameter that can be varied in order to enhance the performance of a laser-driven neutron source, since it affects the overall neutron yield, the maximum energy of the generated neutrons and their angular spectrum. More specifically, the crucial physical quantities necessary to assess the quality of a converter material are: its isotopic composition and the cross sections of all the neutron-producing reactions of its constituents. These two aspects will be discussed in the following subsections.

4.6.1 Role of the converter cross section: analytical calculations

It is well known that the behaviour of each isotope in terms of neutron production efficiency can be traced back to the energy dependence of its cross section for (ion,n) reactions in the range spanned by the accelerated ions. The cross sections for the (p,n) reaction of some selected isotopes is shown in Fig. 4.12 together with the experimental ion spectrum present in the article.

In order to investigate theoretically the influence of the cross section on the neutron yield, a convolution integral between the analytical form of the ion spectrum measured by Zulick and the cross section for neutron production of some solected isotopes has been performed. In particular, in order to obtain an accurate output, the calculation has taken into account for each isotopes the main reactions involving neutron production. These include, besides the standard (p,n) reaction, also processes involving the emission of one or more particles along with the neutron. These latter reactions can be written as (p,n+x+y), where x and y can be either charged particles such as α, deuterons, tritions and protons or other neutrons. The result of this study is shown in Fig. 4.13, which represents the neutron yield as a function of the upper cutoff energy of the accelerated ions.

According to the data reported in Fig. 4.13, limited to the context of the experiment performed by Zulick and colleagues, the most effective isotopes for neutron generation are ^{7}Li and ^{9}Be. Even though all the reactions included in the theoretical calculations should be considered in order to explain this evidence, much can be understood by observing the cross section of the (p,n)

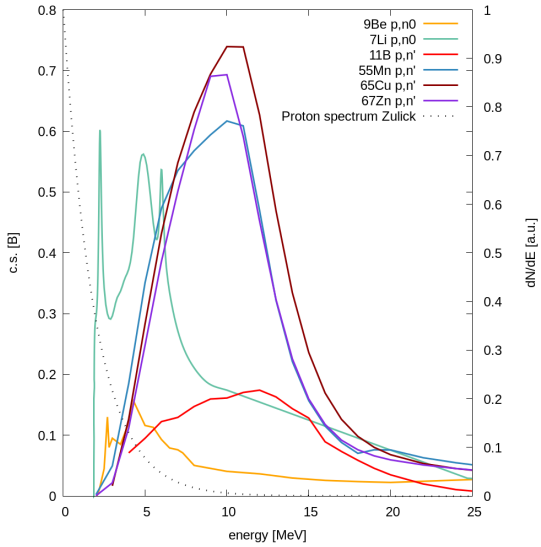

Figure 4.12: *(p,n) reaction cross section for different converter materials. The script n0 means that the produced neutron left the nuclide in its ground state; on the contrary, the script n' means that the emitted electron left the nuclide in one of its possible excited states. Also the analytic form of the ion spectrum reported in the article is shown (dashed line).*

reaction in Fig. 4.12. Indeed, the (p,n) cross section for both lithium and beryllium displays a maximum at energies slightly higher than the reaction energy threshold at ∼2 MeV. As already explained in section 2.2, as a general feature, the neutron yield is enhanced by the presence of high cross section peaks at low energy. In fact, on the one side, seen the exponential form of the ion spectrum produced by TNSA, the overwhelming majority of the accelerated ions reside there; on the other side almost all the ions impinging on the converter will pass through the reaction cross section peak at some moment during their slowing-down.
Both arguments can be invoked to justify the lower neutron yield observed in medium Z elements such as zinc, copper and mangenese. In fact, as it can be seen in Fig. 4.12, the considered isotopes of these materials have cross sections characterized by peaks at energies of ∼10 MeV. Considering that only a few ions in Zulick's neutron spectrum possess that energy, it is clear that their neutron

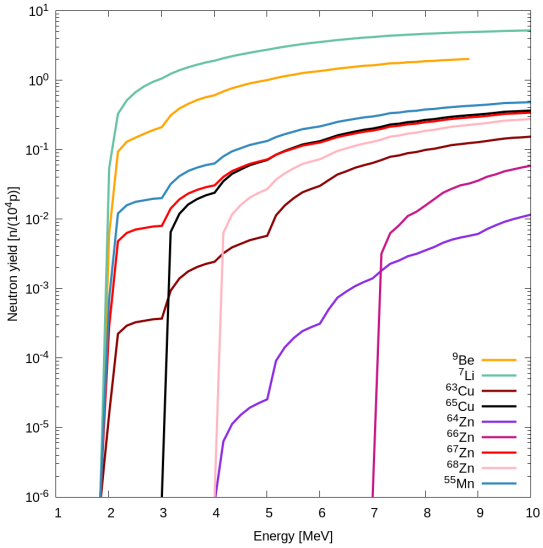

Figure 4.13: *Neutron yield for a set of isotopes as a function of the cutoff energy of the accelerated ions. The ion temperature is equal to that of the experimental spectrum reported by Zulick et al.*

yield will be low.

4.6.2 Role of the converter cross section: Monte Carlo simulations

At this point it would be of interest to make a comparison between the analytical estimates computed in the previous section and the results obtained via Geant4 simulations for the set of considered converter materials. To this purpose, simulations using as an input the analytical form of the experimental ion spectrum measured by Zulick and colleagues have been performed. The thickness of each converter target is equal to the range of the most energetic ions in that material, so as to neutralize the converter thickness factor when evaluating the neutron yield. Their results are shown in Fig.4.14 and 4.15. Moreover, the values of the neutron yield obbtained in the two cases are compared in table 4.5.

Fig.4.14 shows the energy spectrum for all the emitted neutrons and for

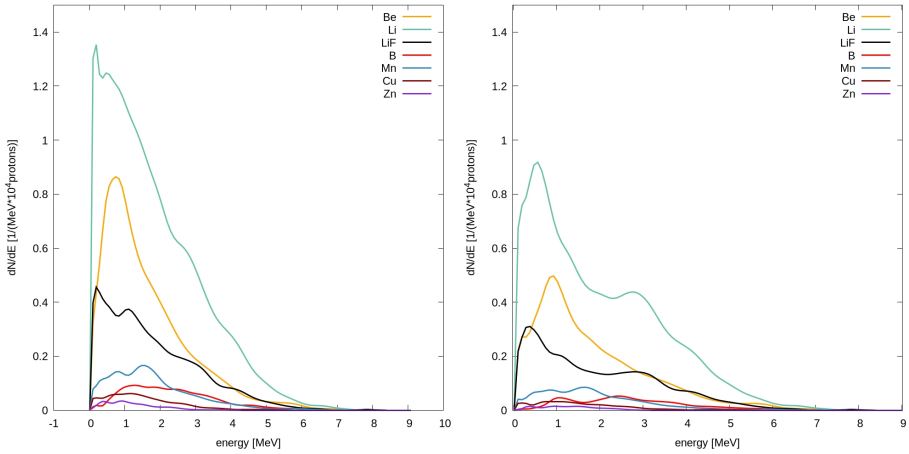

Figure 4.14: *Comparison between the neutron energy spectra of different converter materials. On the left: Energy spectrum of all the emitted neutrons; On the right: Energy spectrum of neutrons emitted in a forward direction in the half-space beyond the converter.*

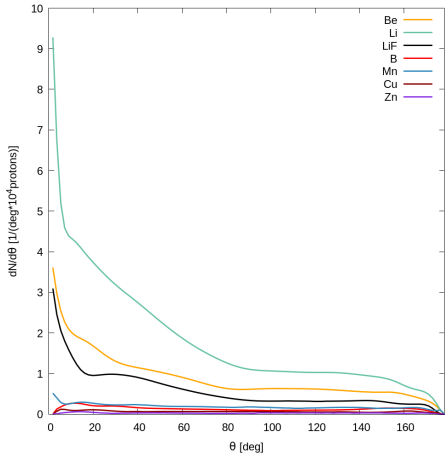

Figure 4.15: *Comparison between the neutron angular spectra of different converter materials.*

Table 4.5: *Comparison between the neutron yield values obtained analytically and numerically for some selected converter materials.*

Element	Analytical yield	Geant4 yield
Beryllium	1.00×10^{-4}	1.68×10^{-4}
Lithium	5.00×10^{-4}	3.43×10^{-4}
Copper	0.23×10^{-4}	0.15×10^{-4}
Managanese	0.50×10^{-4}	0.40×10^{-4}
Zinc	9.47×10^{-6}	5.55×10^{-6}

those emitted in a forward direction in the half-space beyond the converter. In the case of lithium, beryllium and LiF the two spectra are very similar at high energy, therefore indicating that, as expected, the most energetic neutrons are emitted in the forward-direction.
Furthermore, since the (p,n) nuclear reactions for the materials listed in table 4.5 have similar Q-values (ranging from -1.013 MeV for boron to -2.764MeV for Mn), the neutron cutoff energy is similar in all cases.
As regards the angular spectrum of the emitted neutrons (Fig.4.15), neutrons produced on light elements show a high degree of directionality, especially lithium. On the contrary, for medium Z elements the emission is almost isotropic. This is a sign of neutron scattering. Indeed, while medium Z elements have a cross section for elastic scattering which is comparable to the one of light materials, they show a much larger probability of inelastic neutron scattering in the present range of ion energies (see Fig.4.16).

4.6.3 Role of the converter isotopic composition

The second factor affecting the overall neutron yield is the isotopic composition of the employed converter material. The isotopic abundances of the elements considered for the analysis in Fig. 4.13 are reported in table 4.6. For each element the first isotope reported in the line is the most relevant in terms of cross sections for neutron production in the range of ion energies measured in the article.

In order to assess the influence of the isotopic composition of the converter material on the neutron yield, some Geant4 simulations have been performed

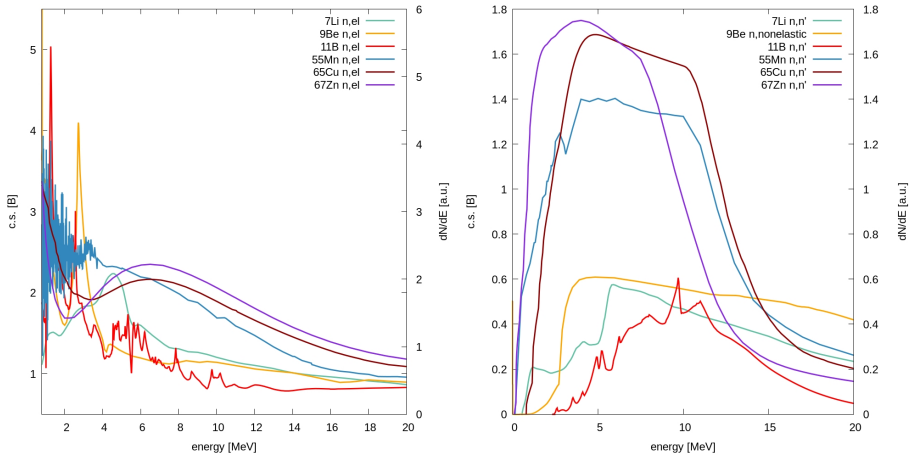

Figure 4.16: *.Cross sections for elastic scattring (on the left) and inelastic scattering (on the right) for different elements.*

Table 4.6: *Isotopic abundances of some selected converter materials.*

Element	Isotopes and relative abundance
Beryllium	^{9}Be=100%, $^{7,10}Be$ in traces
Lithium	^{7}Li=92.41%, ^{6}Li=7.59%
Fluorine	^{19}F=100%
Boron	^{11}B=80%, ^{10}B=20%
Copper	^{65}Cu=30.85%, ^{63}Cu=69.15%
Managanese	^{55}Mn=100%
Zinc	^{67}Zn=4%, ^{64}Zn=49.2%, ^{66}Zn=27.7%, ^{68}Zn=18.5%, ^{70}Zn=0.6%

using converters either characterized by natural isotopic composition or containing for each investigated element only the most effective isotope for neutron production. The thickness of the targets was set equal to 100% of the stopping range of the most energetic ions (10MeV according to Zulick's data). In table 4.7 the results of the simulations are reported.

As expected, the elements whose isotopic composition is dominated by one only isotopic species are paractically insensitive to enrichment: this is the case

Table 4.7: *Comparison between the obtained neutron yield employing the natural and "enriched" version of some selected converter materials.*

Element	Isotope	Natural composition	Enriched composition
Beryllium	^{9}Be	1.73×10^{-4}	1.68×10^{-4}
Lithium	^{7}Li	3.24×10^{-4}	3.43×10^{-4}
LiF	$^{7}Li+^{19}F$	1.09×10^{-4}	1.13×10^{-4}
Boron	^{11}B	2.71×10^{-5}	3.36×10^{-5}
Copper	^{65}Cu	1.50×10^{-5}	2.70×10^{-5}
Managanese	^{55}Mn	3.95×10^{-5}	4.05×10^{-5}
Zinc	^{67}Zn	5.55×10^{-6}	2.19×10^{-5}

of Be, Mn, Li and F (and hence of their compound LiF). For these cases the observed fluctuations between the natural and enriched converter can be related to statistical fluctuations due to the limited number of particles shot in the Monte Carlo simulations. The elements that most benefit from enrichment are, of course, those in which the most effective ion species for neutron production is present in low fractions. This is the case of B and, to a much greater extent, of Zn. Therefore, although theoretically the neutron yield is always enhanced by using converter materials of selected isotopes, the entity of this gain depends heavily on the material being considered and on the energy range of the accelerated ions.

4.6.4 Monte Carlo simulation of a bilayer converter target

As anticipated in section 2.3.1, an experimental work has been reported in the literature in which the performance of a bilayer converter constituted by 1mm of copper on the front side (i.e. the one that "sees" the impinging ions) and 4mm of lithium [15] is tested against that of a monolayer 2cm thick lithium block [15]. The bilayer converter target should exploit the whole incident ion spectrum. Indeed, the thickness of each layer is chosen according to the Bragg peak deposition curve of the accelerated ions and knowing the ion energy for which there is a peak in the (ion,n) cross section for a given material.
The numerical tool for such simulations is the Monte Carlo code Geant4, using as an input an exponential spectrum with cutoff 20MeV and temperature 8 MeV. The TNSA ion spectrum temperature has been evaluated from the data

reported in another paper in which an experiment employing the same laser with very similar parameters is reported [98].
According to experimental results, which are displayed in Fig.4.17, an improvement of a factor 2 in the neutron yield has already been demonstrated using a double layer made up of 4mm of lithium and 1mm of copper instead of a monoelemental 2mm-thick lithium converter. Copper generates neutrons via the ^{63}Cu(p,n)^{63}Zn reaction, where protons are those trasmitted across the first lithium layer. This scheme results in an increase of the neutron yield in the energy range 1-5 MeV. The results obtained by Geant4 in the same energy

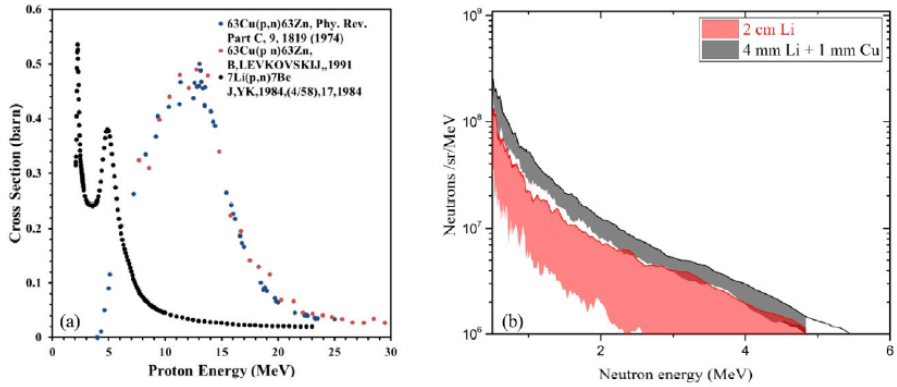

Figure 4.17: *(a) Neutron generation cross sections as a function of proton energies impinging on lithium and copper and (b) measured neutron spectra for the two convertor designs. From [15]*

range are shown in Fig.4.18. As it can be seen, the trend resulting from Geant4 simulations is in contrast with the experimental evidence. Indeed, the Monte Carlo simulation shows a greater neutron yield for lithium alone rather than with the copper foil.
The detrimental effect of copper shown by Geant4 is expected if one considers the analytical calculations resulting in the plot in Fig.4.13, which accounts only for (p,n) reactions on the different materials. Furthermore, it must be noted that the comparison between the two cases is not on even lithium layer thickness and this choice is not motivated by the authors. Experimental values of the cross sections are used by Geant4 for the (p,n) reaction on copper up to 150MeV and on lithium up to 10MeV. Beyond this threshold a theory evaluated TALYS data set is used.

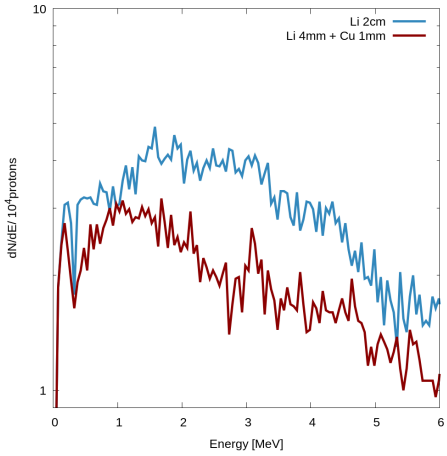

Figure 4.18: *Neutron energy spectrum between 1 and 6 MeV in the two cases tested by Brenner and colleagues.*

Therefore, according to my hypothesis, the observed trend can be attributed either to a moderation and loss of a certain fraction of produced neutrons in the very thick lithium layer or to a neutron multiplication contribution coming from copper, that Geant4 does not wholly simulates. A deeper study of the physics needed in Geant4 to simulate at best this scenario is needed.

Chapter 5

Simulation of a compact laser-driven neutron source

This chapter deals with the design and theoretical investigation of optimized compact laser-driven neutron sources based on a pitcher-catcher scheme. To start with, an overview of the main physical characteristics of compact accelerator- and laser- based neutron sources is given, in order to highlight the differences among the two classes (see section 5.1). Successively, the possible strategies for laser-driven sources optimization will be analysed (see section 5.2). Based on the hitherto-emerged considerations, four different schemes of optimized compact source with realistic laser parameters will be proposed in section 5.3. The performance of such systems has been tested using the Monte Carlo code Geant4: the results will be presented and discussed in section 5.4.

5.1 Comparison between compact neutron sources

In the framework of this thesis work, compact neutron sources have been mentioned in sections 1.3.4 and **??**, where compact accelerator neutron sources (CANS) and compact laser-driven neutron sources have been respectively treated. Despite sharing the adjective "compact" in their names, the systems corresponding to the two cases are extremely diverse.

As discussed in section 1.3.4, CANS produce neutrons with energy less than 100 MeV. They were born in the 1970's in response to the shortfall of neutron beams provided by spallation sources and research nuclear reactors, therefore they were called "compact" to distinguish them from the large neutron facilities such as spallation sources and fission nuclear reactors.
CANS opearate in a pulsed mode with frequencies ranging from some tens to a few hundreds of Hz and can provide ms-long proton bunches with peak intensity of some tens of mA. When a proper converter target is employed, this results in a neutron production of about 10^{11-12} n/s. As regards dimensions, CANS can nowadays be hosted in a bunch of rooms. The simpler design of CANS with respect to large facilities translates into a lower cost, which currently amounts to some tens of million dollars.

On the other hand, as discussed in section 2.3, compact laser-driven neutron sources can reach an even smaller size. This is due to the fact that the wakefield generated by the laser pulse leads to very intense electric fields (of the order of some TV/m), which develope over a length scale of a few μs (2.1). This peculiar feature of the acceleration scheme implies that the size of the overall accelerating system -and hence of the source- is determined by the dimensions of the laser. Therefore, as laser technology progresses, these sources could be produced in smaller and smaller size, eventually leading to the transportability of the source, which would greatly expand the number of users.
Currently, compact laser-driven neutron sources of a few tens of TW in power take up the space of one room. These systems can provide intensities similar to those characterizing large laser systems delivering a lower amount of energy (some J) in a much shorter time (tens of fs). As discussed in detail in section 2.3, besides their reduced size, compact laser-driven neutron sources can be advantageous with respect to CANS. In the first place they can provide potentially larger repetition rates (up to the order of the kHz) and shorter neutron bunch in space ($\sim$1cm at the source) and time (some tens of fs to some ns). Secondly, the generated bunch of neutrons is characterized by high peak intensity and directionality: this is of great advantage for applications. Indeed, current compact laser-driven neutron sources can produce up to 10^{5-7} n/s in the forward direction: this value makes these systems already suitable for applications such as neutron radiography.
Eventually, it should be pointed out that in the framework of compact laser-driven neutron sources, there is great interest in neutron-generating systems employing table-top lasers, which would enlarge the number of users, besides representing a step towards the source portability. The feasibility of neutron

sources based on currently available table-top lasers has been assessed via numerical simulations: the results of such investigation will be presented in section 5.4.

5.2 Optimization of laser-driven neutron sources

To be suitable for a given application, a neutron source must assure that neutrons in a sufficient number and with energy in a well-defined range are delivered on the region that must be irradiated. For this reason an increase in the neutron flux or in the maximum energy usually coincides with an improvement of the source performance. In particular, producing a larger neutron flux is of interest, above all in those applications in which neutron moderation in required. On the other side, a source producing neutrons with a larger maximum energy allows to cover a wider spectrum of applications.
In the particular case of compact laser-driven neutron sources, by definition, the energy transferred to the system and available for neutron generation has an upper limit, beyond which the reduced-size requirement is not respected any more. Therefore, other strategies should be followed in order to enhance the source performance. In the case of a pitcher-cather scheme, because of its modularity, it is possible to operate separately the optimization of the ion acceleration and neutron generation proccesses, applying ameliorative methods tailored to the two cases.

In the first place, as already explained in section 2.1.3, an enhancement in the maximum energy and number of accelerated ions can be obtained making use of carbon nanostructured targets, which consist of an ultralow-density layer (foam) deposited on a μm-thick solid foil. The idea at the basis of this scheme is that, when ionized by the plasma, the foam creates a near-critical plasma layer, which should allow a greater coupling between laser and matter, with consequent enhancement in the efficiency of laser-ion energy conversion. In order to optimize the ion acceleration performance, given a certain set of laser parameters, it is possible to find an optimum in the foam thickness and density.

Another aspect concerning the pitcher is the nature of the accelerated ions. Indeed, it could be of interest to consider the possibility of accelerating deuterons along with protons. Despite the increase in the experimental complexity of target preparation, neutron generation via deuteron-induced reactions has many advantages from a physical point of view. Indeed, as discussed in section 2.2,

deuteron-induced reactions are characterised by a positive Q-value, which enables the production of much more energetic neutrons with respect to the case of protons accelerated to the same energy. This different is large in lithium, for which the Q-values of (p,n) and (d,n) reactions amounts to -1.64 and +15.03 MeV. Furthermore the (d,n) reaction is characterized by a degree of anisotropy increasing with the impinging ion energy. All the aforementioned issues have been discussed extensively in section 2.3.

As concerns the design of an optimized converter, the parameters at play are the converter thikness and material, whose role has been discussed in detail in section 4.6. In general, two aspects must be taken into account. In the first place, in order to maximize the obtained neutron yield, it is necessary to employ a converter thickness equal to the range of the most energetic ions impinging on the converter. Notice that a too thick converter would lead to a decrease in the neutron beam collimation and hence to a reduction in the forward-directed flux. Secondly, it is important to stress that the quality of a converter material can not be established in an absolute way: on the contrary, it should be evaluated only with respect to the specific ion spectrum considered.

Based on the considerations made up to this point, in the next section fuor optimized scenarios of laser-driven neutron sources will be presented.

5.3 Simulated scenarios

In this section four scenarios of compact laser-driven neutron sources in a pitcher-catcher scheme, optimized according to the considerations reported in the previous section, are presented. In particular, the idea is to simulate optimized compact sources with realistic laser parameters using integrated multi-physics simulations. By so doing, it has been possible to test the performances of realistic compact laser-driven sources and to assess whether they can, at least in principle, be employed in applications. Multi-physics simulations are performed following the approach illustrated in section 3.2.1, i.e. using the PIC code PICCANTE to simulate laser-target interaction and the Monte Carlo code Geant4 to study ion conversion into neutrons.
To be more specific about simulations, two source types have been taken into account: a source employing a table-top laser system with power 20 TW and another one employing a more powerful (74 TW), though still compact, device. Furthermore, for both cases the effect of the addition of deuterons to the proton

contaminants layer on the rear of the target has been investigated. This has led to 4 cases being simulated. In all cases the source performance has been enhanced by making use of:

1. A nanostructured target with optimal thickness and density;

2. A converter of a suitable material and optmimal thickness.

The resulting neutron-generating scheme is displayed in Fig. 5.1, while the main data of the four simulated scenarios are reported in table 5.1.

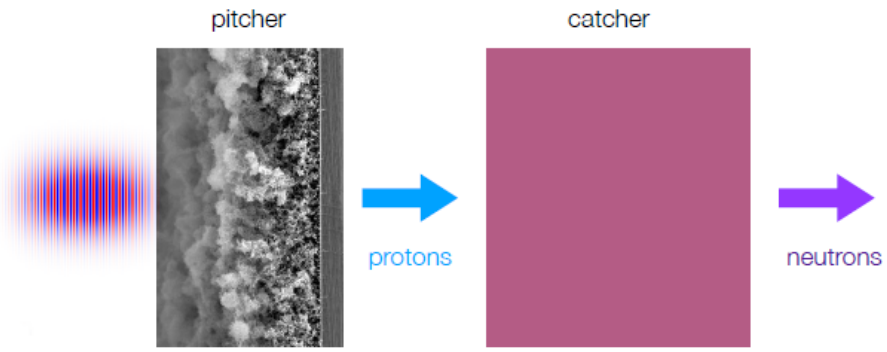

Figure 5.1: *Pitcher-catcher scheme employing an advanced nanostructured converter.*

In all scenarios the accelerated ions originate from a layer of contaminants placed on the rear side of the target. In scenarios 2 and 4, in which both protons and deuterons are accelerated, a layer constituted by protons and deuterons in equal quantity has been employed. The thickness of such layer and the number density of contaminants have been kept constant in all the four cases.
The optimal characteristics of the foam associated to each set of laser parameters have been chosen comparing the results of a number of 2D PIC simulations performed varying the density and thickness. The result of such investigations is shown in Fig. 5.2 for a_0=3 and a_0=11.

[1] a_0 is the so-called "dimensionless" laser parameter, which is proportional to the laser intensity (see section 2.1.)

[2] The foam density is expressed in units of the critical plasma density n_c (see section 2.1 for further information.).

Table 5.1: *Main data of the simulated scenarios.*

		Scenario 1	**Scenario 2**	**Scenario 3**	**Scenario 4**
Laser parameters	λ [μm]	0.8	0.8	0.8	0.8
	τ [fs]	30	30	30	30
	a_0[1]	3	3	11	11
	E [J]	0.6	0.6	2.2	2.2
	P[TW]	20	20	74	74
Foam	Thickness [μm]	4	4	8	8
	Density [n_c][2]	1	1	2	2
	Density [mg/cm^3]	6	6	?	?
Substrate	Thickness [μm]	0.8	0.8	0.8	0.8
	Density [mg/cm^3]	260	260	260	260
Ions		p	p+d	p	p+d

While in the case a_0=3 the most performing foam (thickness 4μm, density 1n_c) has been chosen, with a_0=11 the second best candidate was chosen (i.e. thickness 8μm, density 2n_c). This choice was motivated by the fact that a foam with the best set of parameters (i.e. thickness 8μm, density 1n_c) cannot currently be produced by PLD techniques.

Based on the considerations reported in section 4.6 about the performances of different converter materials and with the aim of maximizing the number of produced neutrons, lithium has been chosen in all the four simulated cases. Since the handling of this material is hard, in the following section some alternatives will be presented, along with an esteem of their impact on the neutron yield. Also the choice of an optimal value for the converter thickness will be discussed in the next section, in light of the energy ion spectrum produced by PIC simulations in each of the four cases.

One final point should be addressed: in PIC simulations only ions with a certain lower energy threshold have been recorded. The selected threshold is equal to 1.85 MeV for protons and 0.5 MeV for deuterons. This strategy is aimed at maximizing the number of neutrons seen in the output of the Monte Carlo code for a given number of ions sampled from the PIC ion energy distribution: indeed, protons with an energy lower than 1.88 MeV do not contribute to the neutron yield because the energy threshold of the (p,n) reaction is equal to 1.88 MeV; as regard deuterons, even if no energy threshold for the (d,n) reaction

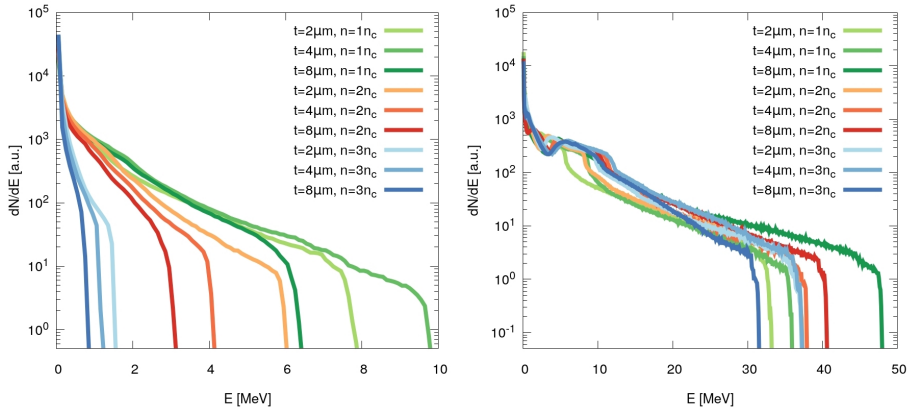

Figure 5.2: *Energy spectra of TNSA-accelerated protons for different density and thickness values obtained using a laser with a_0=3 (on the left) and a_0=11 (on the right).*

on lithium is present, the cross section employed by Geant4 is very low until deuteron energy of about 1 MeV. This latter point will be further discussed in the following section.

5.4 Discussion of results

The results of the PIC simulations performed with the parameters listed in table 5.1 are displayed in Fig. 5.3 and in table 5.2 for the four considered cases.

As it can be seen from Fig. 5.3, in all the simulated cases the upper part of the ion energy spectrum has the typical shape of an energy spectrum of ions accelerated via TNSA, i.e., using a semi-logarithmic scale, a line up to a certain upper cutoff energy.

Furthermore, as expected in TNSA, ions appear to be accelerated proportionally to their charge-to-mass ratio. Indeed, in those scenarios in which both deuterons (q/m=1/2) and protons (q/m=1) are accelerated, the former are accelerated to much lower energies with respect to the latter. This is the reason why, although the same fraction of protons and deuterons is present in the contaminants' layer, the number of accelerated deuterons is slightly lower than that of protons (see table 5.2).

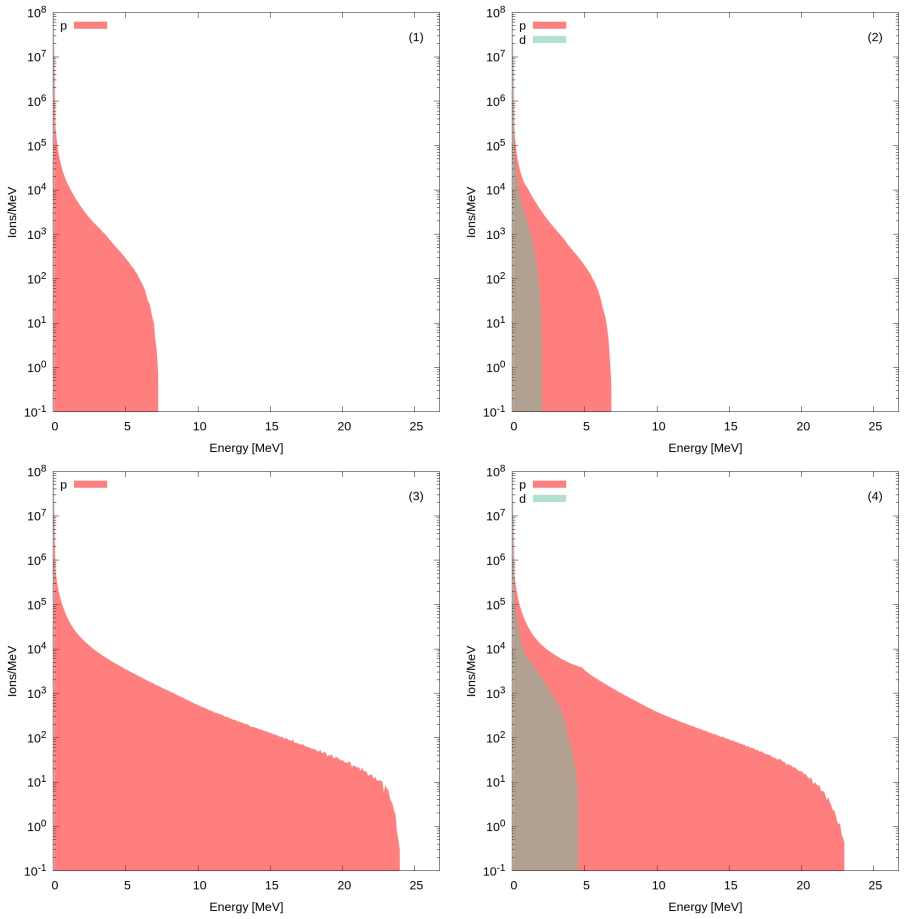

Figure 5.3: *Energy spectra of the accelerated ions resulting from PIC simulations.*

Finally, given a certain a_0, i.e. at fixed laser intensity and wavelength, the presence of deuteron contaminants leads to a decrease in the maximum proton energy. This can be seen if the maximum proton energies in scenarios 1 and 2 or 3 and 4 are compared. Clearly, this is due to the fact that when ions belonging to different species are accelerated, the energy available for acceleration must be shared among the two ion species.

Table 5.2: *Number of the accelerated ions in each scenario.*

	Scenario 1	**Scenario 2**	**Scenario 3**	**Scenario 4**
Protons	9.6×10^9	7.5×10^9	6.7×10^{10}	5.4×10^{10}
Cutoff [MeV]	∼7	∼7	∼24	∼22.5
Deuterons		4.9×10^9		2.0×10^{10}
Cutoff [MeV]		∼2.0		∼4.5

In consideration of the ion energy spectra produced by PIC simulations, it has been possible to choose optimal values for the lithium converter thickness in each of the four considered cases. In order to exploit the whole ion spectrum for neutron generation, it is necessary that all the ions stop inside the converter. Since protons are accelerated to higher energies than deuterons and possess a longer stopping range in matter, the converter thickness has beeen set equal to the range in lithium of the most energetic protons obtained by PIC simulations. The fact that deuterons "see" a converter much thicker than their stopping range is not detrimental in terms of neutron yield, while it could lead to a less collimated neutron bunch (see section 4.6). The main converter data used for Monte Carlo simulations of the four scenarios are listed in table 5.3.

Table 5.3: *Converter data in the simulated scenarios.*

	Scenario 1	**Scenario 2**	**Scenario 3**	**Scenario 4**
Converter thickness [mm]	2	1.43	13.3	11.8

The neutron spectra obtained via Geant4 simulations for the four considered cases are displayed in Fig. 5.4, while the data concerning the neutrons' angular distribution are reported in table 5.4. With reference to Fig. 5.4, notice that, due to technical reasons, apart from in case "Case 1", it hasn't been possible in Monte Carlo simulations to shoot a number of ions sufficient for eliminating the noise in the graphs. In any case, the neutron spectra have been rescaled so as to reproduce on the y axis the value of neutron emission which would have been obtained shooting a nummber of ions equal to that provided from PIC

simulations.

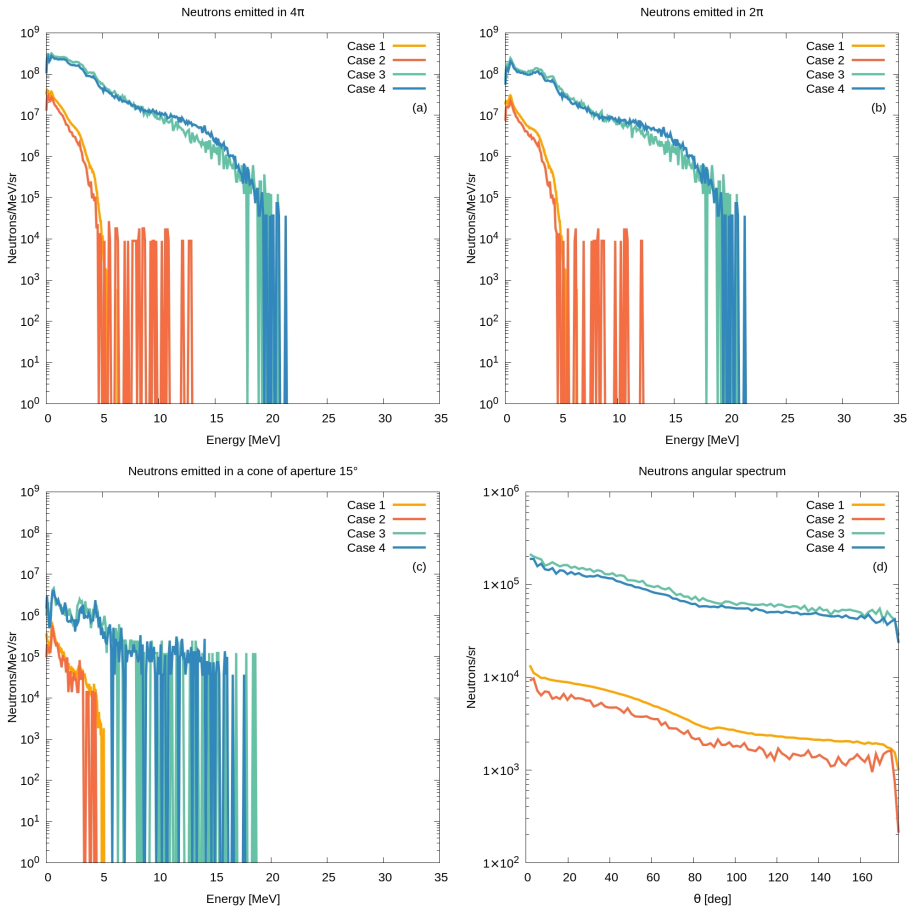

Figure 5.4: *Images (a), (b), (c) show for each scenario the energy spectra of neutrons emitted in a solid angle of 4π, 2π and 0.544 sr, respectively. Image (d) shows the angular spectra of the neutrons obtained by Geant4 simulations.*

In the first place, by comparing the ion and neutron energy spectra for each of the four simulated cases (shown in Fig. 5.4 (a), (b) and (c)), it can be seen that the maximum neutron energy is in all cases compatible with the pro-

Table 5.4: *Number of neutrons emitted in solid angles of 4π and within a cone of aperture 15°, according to Geant4 simulations.*

	$\mathbf{Y}_{tot}$ **[n/sr]**	$\mathbf{Y}_{15deg}$ **[n/sr]**
Scenario 1	2.22×10^5	5.07×10^5
Scenario 2	1.51×10^5	3.75×10^5
Scenario 3	4.66×10^6	8.94×10^6
Scenario 4	4.05×10^6	7.91×10^6

tons' upper cutoff energy and with the Q-value of the exploited reactions, which amounts to -1,644MeV for the (p,n) reaction on lithium and to +15,03MeV for the (d,n) process. Indeed, the relation $E_{max,n}$=$E_{max,ion}$+Q is always satisfied. The large postive Q-value of the (d,n) reaction implies that, despite being less energetic, deuterons produce the most energetic neutrons.
Besides their influence on the neutron maximum energy, deuterons are expected to affect also the number of produced neutrons. This effect can be studied comparing, at fixed laser parameters, the neutron energy spectra obtained simulating the acceleration of one or more ion species. The results of such operation are displayed in Fig. 5.5, where the energy spectra of the overall- and forward-emitted neutrons, are displayed. The neutron emission in an angle ofπ in the two scenarios is reported in table 5.5.

Table 5.5: *ontribution of protons to the neutron emission over a solid angles of 4π in scenarios 2 and 4.*

	Only protons [n/sr]	**Protons + deuterons [n/sr]**
Scenario 2	1.51×10^5	1.51×10^5
Scenario 4	3.62×10^6	4.05×10^6

The values listed in table 5.5 correspond to the integral of the spectra reported in Fig.5.5. As it can be seen, while in the case a_0=11 the presence of deuterons results in a significant increase of the neutrons emitted over 4π (blue lines), the same is not true in the case a_0=3, in which the neutron emission over the same solid angle remains approximately constant and equal to 1.51×10^5n/sr.

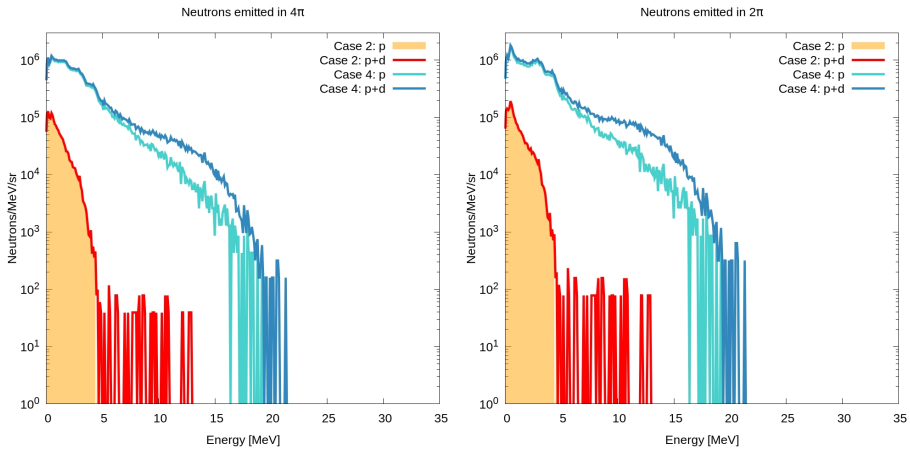

Figure 5.5: *Effect of the presence of deuterium contaminants on the energy spectra of neutrons emitted in a solid angle of 4π (left) and 2π (right).*

Hence, in this latter case it can be concluded that deuterons do not lead to a significant increase in the number of produced neutrons. However, their signature can be seen in the production of neutrons with energies higher than the maximum neutron energy obtained with protons.
The fact that in case a_0=3 deuterons do not significantly contribute to neutron production has been attributed, at least partially, to the (d,n) reaction cross section employed by Geant4 in the energy range of the incident deuterons, i.e. from 0.5 to 2 MeV. Indeed, although the (d,n) reaction is exothermic and therefore has no energy threshold, the the toolkit employs the theory-driven TALYS 2014 cross section, which is zero up to 1 MeV. Below 1 MeV only the data-driven ENDFB-7.1 cross section for the (d,n+α) reaction is considered for neutron production. The trend of the aforementioned cross section data is reported in Fig. 5.6. This feature of TALYS cross sections for deuteron-induced reactions has already been highlighted in section 2.2 and is common to all the considered materials. The effect of this lack of information is particularly serious, especially when laser-driven neutron sources are considered. In fact, the typical exponential shape of the ion spectrum implies that a large number of particles at energy below 1 MeV are not able to react, in constrast to the physics of the reaction.

In order to obtain information on the value of the (d,n) cross section at energies lower than 1 MeV, experimental data have been sought. However, it has been possible to find only two data sets for the (d,n) reaction cross section on lithium. Among these data, only one experimental point for energies below 1 MeV has been found, corresponding to a deuteron energy of 0.91 MeV. The experimental data considered are also reported in Fig. 5.6.
Clearly, the lack of both theoretical and experimental information for (d,n) reactions on lithium at low deuteron energy compromises the reliability of Monte Carlo codes in simulating such scenarios, which are typical in the framework of laser-driven neutron sources. For this reason, it would be significant and also beneficial for simulations to perform experiments aimed at measuring the value of deuteron-induced cross sections at low deuteron energy.
All of this considered, it can be concluded that the presence of an energy cutoff at 0.5 MeV in the PIC ion energy spectra used as input to Geant4 will not lead to a significant loss in terms of number of produced neutrons.

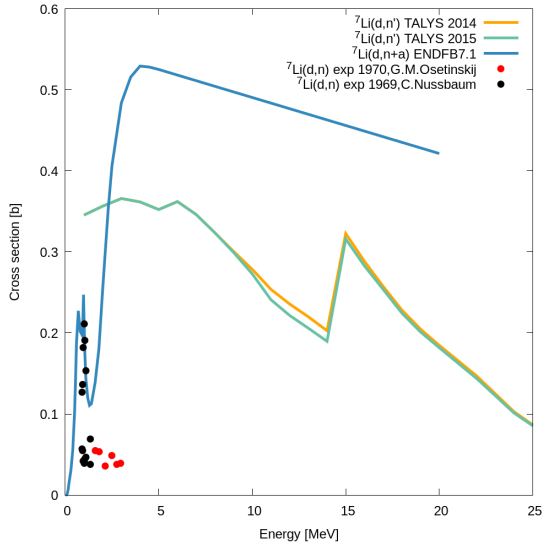

Figure 5.6: *Comparison between the TENDL, ENDFB7.1 and experimental cross section data for the reaction* $^{7}Li(d,n)^{8}Be$.

In order to determine to which extent the zero value of the (d,n) cross section

below 1 MeV affects neutron production, a comparison with experimental data has been performed. In particular, the number of neutrons produced by the (d,n) reaction on lithium predicted by Geant4 in the case with a_0=3 has been compared to experimental data obtained by Zulick and colleagues using laser parameters similar to those employed in scenario 2 [14]. Their results show a neutron flux of 4.6×10^5n/sr in the forward direction. This has been obtained accelerating 2.968×10^{12} deuterons with energies in the range 0.5-2 MeV on a lithium fluoride (LiF) converter. The laser pulse has a duration of 40fs and delivers an energy of 1.1 J on the target. Since Geant4 estimates the neutron yield attributable to deuterons as 8.60×10^{-7}n/d, the corresponding simulated neutron emission in the forward direction would amount to 7.74×10^4n/sr, which is one order of magnitude less than the experimental result. Moreover, LiF has an ion-coversion performance which can be estimated at zero order as 1/2 of that of elemental lithium (see the end of this section for further details.). If this is taken into account, the discrepancy grows. Therefore, it can be concluded that Geant4 heavily underestimates neutron production when low-enegy (d,n) reactions on lithium are involved.

The angular distibution of neutrons obtained by Geant4 simulations is displayed in Fig.5.4(d). As expected, in all the considered cases the neutrons are collimated in the forward direction. In particular, in agreement with what has been said in section 2.2, the highest degree of anisotropy is shown by neutrons produced via (p,n) reactions on lithium. No significant differences in the angular spectra are observed when also deuterons are accelerated. Indeed, even if neutrons tend to be more collimated in the forward direction as the incident deuteron energy grows, the ions of a few MeV considered in our analysis are not energetic enough to significantly influence the overall neutron angular distribution.

In order to assess the performance of the four simulated neutron sources in view of possible applications, the amount of emitted neutrons in the forward direction should be considered. Indeed, a highly beamed neutron flux would be extremely helpful for improving transport capabilities and efficient moderation of the neutrons to thermal and epithermal energies.
According to the data reported in table 5.4 and consistently with the results shown in Fig. 5.4(d), the highest number of emitted neutrons per steradian is registered in scenario 3, over a cone of aperture 15°. This value amounts to 8.94×10^6 n/s with energy up to 22.5 MeV theoretically, even if the low statistics impedes to see counts at an energy higher than 19 MeV. The obtained value

is comparable to the values reported in literature for neutrons obtained from compact lasers [14, 76]. If a sample placed at a distance of 5 cm from the source is considered, together with a laser repetition rate of 10Hz, the neutron flux on it would be equal to $\sim 3.58 \times 10^6 \mathrm{n/cm^2/s}$. This value could be sufficient, at least in principle, for performing fast neutron radiography or for testing materials against SEE (see section 1.2). For performing thermal neutron radiography, a similar flux of thermalized neutrons should be provided after moderation. Since thermalization implies the loss of a fraction of the produced neutrons, the number of produced particles should be increased.

As a final point, some considerations about the choice of lithium as a converter are presented. As extensively explained in section 4.6, the choice of the most suitable converter material in a given scenario depends on which aspect one would like to privilege. For instance, lithium is usually the best material for ion conversion from the point of view of the neutron yield. Conversely, the handling of such material is not straightforward: issues such as low melting point, high reactivity and production of long-lived radioisotopes must be faced (see section 2.2). For this reason lithium is often substituted with materials such as beryllium and lithium fluoride which, though, lead to a lower neutron yield. This decrement can be easily estimated.
As a first approximation, when LiF is used instead of lithium, the neutron yield is reduced by a factor 1/2. Indeed, fluorine has a small cross section for neutron production, so its contribution can be neglected (see section 4.2).
On the other side, beryllium has a non negligible cross section for both (p,n) and (d,n) reactions. In this case, the comparison with lithium can be operated performing, for each material, a convolution between the analytical expression of the ion energy spectrum and the cross sections of the most important ion-induced neutron producing reactions. This analytical approach has been presented in section 3.1 and corresponds to computing integral (3.4) using the aforementioned cross-section values. The results of calculations are listed in table 5.6.

Although beryllium shows a worse performance in all the considered cases, higher yields are obtained when a_0=11 with respect to when a_0=3. This must be attributed to the higher temperature of the ions obtained from PIC simulations in the former case, i.e., graphically, to a slower descent of their energy spectrum. This implies that a greater number of ions will possess high energy values. This is in turn beneficial for the neutron yield because, during their slowing-down, the ions cross a larger portion of material and therefore have a greater probability

Table 5.6: *Neutron yield of beryllium compared to that of lithium, taken as a reference for all the simulated scenarios.*

	Scenario 1	**Scenario 2**	**Scenario 3**	**Scenario 4**
Y_{Be}/Y_{Li}	40%	40%	50%	66%

to react. This effect is shown in Fig. 5.7.

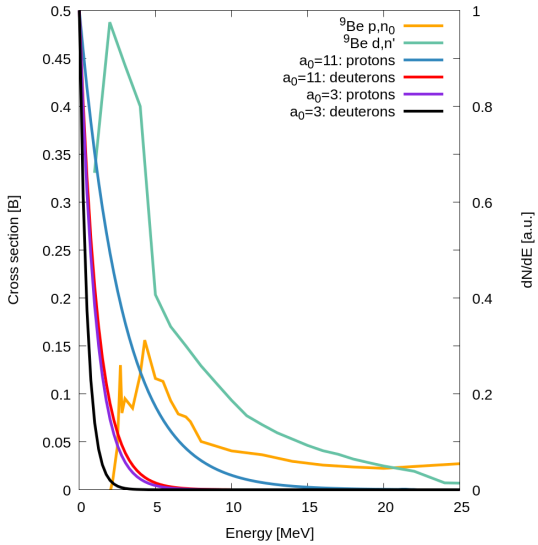

Figure 5.7: *Effect of TNSA ion temperature in determining the neutron yield of (p,n) and (d,n) reactions on ^{9}Be.*

Moreover, the decrement in the neutron yield results attenuated when deuterons, besides protons, are accelerated. This is due to the fact that, according to calculations, beryllium leads to a neutron yield which is slightly higher than lithium when (d,n) reactions are involved. This effect is well visible in scenario 4, but can not be observed in scenario 2 due to their weak contribution to neutron production with respect to protons. If only deuterons are accelerated, beryllium will the best material for ion conversion.

These simple estimates are useful for evaluating at which cost, in terms of neutron yield, a simpler handling of the converter target can be obtained and, therefore, for getting oriented in the choice.

Chapter 6

Conclusion and perspectives

A theoretical investigation aimed at establishing the degree of reliability for the simulation of laser-driven neutron sources (see chapter 4 has been performed. The system under examination relies on a pitcher-catcher scheme for neutron production. In this scheme a super-intense laser pulse impinges on a thin solid target (called *pitcher*), from which ions are accelerated. These latter are made to impinge on a converter material (called *catcher*), where neutrons are generated by (p,n) or (d,n) nuclear reactions. The neutron generation process has been studied by means of theoretical methods, including analytical and numerical techniques (see chapter 3). Among these latter, multi-physics simulations combining particle-in-cell (PIC) methods for the simulation of laser-target interaction and Monte Carlo approaches for studying ion-induced neutron generation have been performed. Besides this, analytical methods have been used for simple estimates of characteristic quantities of the system. The above-described theoretical tools have been employed for performing a benchmark against experimental data properly selected from the literature. Multi-physics simulations have also been employed for the study of an optimized design of compact laser-driven neutron source (see chapter 5).

Theoretical tools prove to be reliable for the simulation of the aforementioned systems only to a certain extent.
On the one side, some key features of the physics of laser-target interaction and neutron generation processes are well captured by simulations. Indeed, using particle-in-cell methods the characteristic exponential form of the ion energy spectrum resulting from TNSA can be reproduced, while Monte Carlo meth-

ods and analytical techniques are capable of reproducing with accuracy the maximum obtainable neutron energy for a given ion energy distribution. On the other side, many criticalities related to their use have emerged during the study.
In the first place, while many papers concerning laser-driven ion acceleration are present in the literature, experimental and theoretical works about laser-driven neutron sources do not come in large numbers. Also for this reason, it has been very difficult to find an article suitable for the benchark. More precisely, there are very few experimental works providing sufficiently rich and precise information about both the accelerated ions and the obtained neutrons. When only limited information is available, the theoretical result depends on the hypotheses adopted for the missing data.
Secondly, the theoretical methods relying on the use of cross sections for nuclear reactions (i.e. the Monte Carlo method and the analytical techniques), were affected by the lack of experimental reliable data over the investigated energy range (from 0 to a few tens of MeV).

More specifically, it could be concluded that:

- Analytical methods prove to be reliable as far as simplified schemes are concerned. Indeed, they are able to correctly predict the maximum energy obtained by a neutron produced by a nuclear reaction, but fail at performing quantitative predictions when phenomena of higher complexity are considered. This is the case of the analytical computation of the neutron yield measured in an experiment, which would require to take into account, besides neutron generation, phenomena such as neutron transportation inside and outside the converter. The complete description of such system would require an enormous increase in the complexity of calculations, which would make analytical methods disadvantageous with respect to numerical tools. Therefore, the accuracy of analytical tools in making predictions depends on how many variables of the real system can be included in a description which is kept simple. As cited above, analytical methods suffer from the lack of reliable values for the cross section of nuclear reactions.

- PIC simulations are considered reliable tools for the simulation of experiments of laser-driven ion acceleration in the range of energies interesting for this work. Indeed, PIC codes have been used also in the field of laser-driven neutron sources for making predictions about experimental results concerning the accelerated ions. However, the limitations imposed on

characteristic quantities of the system by the computational cost of such simulations, combined with the currently limited number of experiments reported in the literature, result in the fact that it is not so straightforward to find an article suitable for a benchamrk.

- As a general concept, the reliability of Monte Carlo methods highly depends on the veridicity of the cross sections employed for calculations. Among the available codes, Geant4 proves to be only partially reliable for simulating the experimental neutron spectra. Indeed, the use of theory-based cross section data in substitution of experiment-based values, can result in significant discrepancies with experimental observations.

Several issues naturally arise as a continuation of the presented work.
For the development of reliable theoretical tools for the simulation of laser-driven neutron sources, experiments aimed at improving the number and quality of cross section data for the nuclear reactions which are of interest for the field are advisable. Furthermore, it may result interesting to design an experiment aimed at testing the perfomance of theoretical methods for the simulation of a laser-based neutron source. In this experimental scenario aspects such as an easy computational reproducibility of the neutron generation mechanism should be privileged, in order to obtain an amount of data large enough to be analysed statistically. In turn, the analysis would be helpful in refining the architecture of the numerical tool. Based on the considerations presented in chapter 3, a high reproducibility of the experiment can be obtained using a compact laser in a pitcher-catcher scheme.
As regards the future development of compact laser-driven neutron sources, higher values of the neutron flux should be reached in order to make them suitable for applications. As illustrated in chapter 5, at a given laser power the neutron flux can be optimized by employing nanostructured pitcher targets and converters of proper material and thickness. However, more advanced schemes may lead to an even better performance. These include the possibility to employ a bilayer converter target, which exploits the whole incident ion spectrum. The thickness of each layer is chosen according to the Bragg peak deposition curve of the accelerated ions and knowing the ion energy for which there is a peak in the (ion,n) cross section for a given material. Improvement of a factor 2 in the neutron yield has already been demonstrated using a double layer made up of 4mm of lithium and 1mm of copper instead of a monoelemental 2mm-thick lithium converter [15].

Based on these ideas, the present work may represent a starting point for future, deeper numerical studies on optimised compact laser-driven neutron sources. Provided that the above-presented criticalities are addressed and solved, multi-physics simulations might become extremely useful tools for the design of novel neutron generation schemes, leading to neutron fluxes sufficient for applications.

Bibliography

[1] B. Sowerby, N. Cutmore, Y. Liu, H. Peng, J. Tickner, Y. Xie, and C. Zong, "Recent developments in fast neutron radiography for the interrogation of air cargo containers," in *IAEA Conference, Vienna*, pp. 4–8, 2009.

[2] A. Buffler, "Contraband detection with fast neutrons," *Radiation Physics and Chemistry*, vol. 71, no. 3-4, pp. 853–861, 2004.

[3] I. Anderson, C. Andreani, J. Carpenter, G. Festa, G. Gorini, C.-K. Loong, and R. Senesi, "Research opportunities with compact accelerator-driven neutron sources," *Physics Reports*, vol. 654, pp. 1–58, 2016.

[4] Y. Arikawa, M. Utsugi, M. Alessio, T. Nagai, Y. Abe, S. Kojima, S. Sakata, H. Inoue, S. Fujioka, Z. Zhang, *et al.*, "High-intensity neutron generation via laser-driven photonuclear reaction," *Plasma and Fusion Research*, vol. 10, pp. 2404003–2404003, 2015.

[5] D. L. Chichester and J. D. Simpson, "Compact accelerator neutron generators," *Industrial Physicist*, vol. 9, no. 6, pp. 22–25, 2004.

[6] A. Formenti, "Intense laser interaction with nanostructured plasmas: a kinetic numerical investigation," Master's thesis, Politecnico di Milano, 2016.

[7] F. Mirani, "Ion beam analysis with laser-driven proton beams," Master's thesis, Politecnico di Milano, Italy, 2017.

[8] M. Borghesi, A. Bigongiari, S. Kar, A. Macchi, L. Romagnani, P. Audebert, J. Fuchs, T. Toncian, O. Willi, S. Bulanov, *et al.*, "Laser-driven proton acceleration: source optimization and radiographic applications," *Plasma Physics and Controlled Fusion*, vol. 50, no. 12, p. 124040, 2008.

[9] I. Prencipe, A. Sgattoni, D. Dellasega, L. Fedeli, L. Cialfi, I. W. Choi, I. J. Kim, K. A. Janulewicz, K. Kakolee, H. W. Lee, *et al.*, "Development of foam-based layered targets for laser-driven ion beam production," *Plasma Physics and Controlled Fusion*, vol. 58, no. 3, p. 034019, 2016.

[10] G. Petrov, D. Higginson, J. Davis, T. B. Petrova, C. McGuffey, B. Qiao, and F. Beg, "Generation of energetic (> 15 mev) neutron beams from proton- and deuteron-driven nuclear reactions using short pulse lasers," *Plasma Physics and Controlled Fusion*, vol. 55, no. 10, p. 105009, 2013.

[11] J. Davis, G. Petrov, T. Petrova, L. Willingale, A. Maksimchuk, and K. Krushelnick, "Neutron production from 7li (d, xn) nuclear fusion reactions driven by high-intensity laser–target interactions," *Plasma Physics and Controlled Fusion*, vol. 52, no. 4, p. 045015, 2010.

[12] Y. Yamagata, K. Hirota, J. Ju, S. Wang, S.-y. Morita, J.-i. Kato, Y. Otake, A. Taketani, Y. Seki, M. Yamada, *et al.*, "Development of a neutron generating target for compact neutron sources using low energy proton beams," *Journal of Radioanalytical and Nuclear Chemistry*, vol. 305, no. 3, pp. 787–794, 2015.

[13] D. Higginson, J. McNaney, D. Swift, T. Bartal, D. Hey, R. Kodama, S. Le Pape, A. Mackinnon, D. Mariscal, H. Nakamura, *et al.*, "Laser generated neutron source for neutron resonance spectroscopy," *Physics of plasmas*, vol. 17, no. 10, p. 100701, 2010.

[14] C. Zulick, F. Dollar, V. Chvykov, J. Davis, G. Kalinchenko, A. Maksimchuk, G. Petrov, A. Raymond, A. Thomas, L. Willingale, *et al.*, "Energetic neutron beams generated from femtosecond laser plasma interactions," *Applied Physics Letters*, vol. 102, no. 12, p. 124101, 2013.

[15] C. Brenner, S. Mirfayzi, D. Rusby, C. Armstrong, A. Alejo, L. Wilson, R. Clarke, H. Ahmed, N. Butler, D. Haddock, *et al.*, "Laser-driven x-ray and neutron source development for industrial applications of plasma accelerators," *Plasma Physics and Controlled Fusion*, vol. 58, no. 1, p. 014039, 2015.

[16] D. Chichester, J. Simpson, and M. Lemchak, "Advanced compact accelerator neutron generator technology for active neutron interrogation field work," *Journal of Radioanalytical and Nuclear Chemistry*, vol. 271, no. 3, pp. 629–637, 2007.

[17] R. Avagyan, R. Avetisyan, V. Ivanyan, and I. Kerobyan, "Study of low energy neutron beam formation based on geant4 simulations," *Nuclear Instruments and Methods in Physics Research Section B: Beam Interactions with Materials and Atoms*, vol. 402, pp. 247–250, 2017.

[18] D. Strickland and G. Mourou, "Compression of amplified chirped optical pulses," *Optics communications*, vol. 55, no. 6, pp. 447–449, 1985.

[19] H. Abele, "The neutron. its properties and basic interactions," *Progress in Particle and Nuclear Physics*, vol. 60, no. 1, pp. 1–81, 2008.

[20] W. Pauli, *Das Jahr 1932 Die Entdeckung des Neutrons*. 0, 1985.

[21] E. Rutherford, "Bakerian lecture: Nuclear constitution of atoms," *Proceedings of the Royal Society of London A: Mathematical, Physical and Engineering Sciences*, vol. 97, no. 686, pp. 374–400, 1920.

[22] G. F. Knoll, *Radiation detection and measurement*. John Wiley & Sons, 2010.

[23] A. Favalli, N. Guler, D. Henzlova, K. Falk, S. Croft, D. C. Gautier, K. D. Ianakiev, M. Iliev, S. Palaniyappan, M. Roth, *et al.*, "Experimental observation of beta-delayed neutrons from 9li as a way to study short-pulse laser-driven deuteron production," *0*, 2016.

[24] R. F. Barth, J. A. Coderre, M. G. H. Vicente, and T. E. Blue, "Boron neutron capture therapy of cancer: current status and future prospects," *Clinical Cancer Research*, vol. 11, no. 11, pp. 3987–4002, 2005.

[25] G. Zaccai, "How soft is a protein? a protein dynamics force constant measured by neutron scattering," *Science*, vol. 288, no. 5471, pp. 1604–1607, 2000.

[26] R. Hertzog and R. Plasek, "Neutron-excited gamma-ray spectrometry for well logging," *IEEE Transactions on Nuclear Science*, vol. 26, no. 1, pp. 1558–1567, 1979.

[27] J. Hartman and A. Barzilov, "Combined photon–neutron radiography for nondestructive analysis of materials," *Journal of Radioanalytical and Nuclear Chemistry*, vol. 307, no. 3, pp. 2307–2312, 2016.

[28] W. Kockelmann, A. Kirfel, S. Siano, and C. Frost, "Illuminating the past: the neutron as a tool in archaeology," *Physics education*, vol. 39, no. 2, p. 155, 2004.

[29] A. V. Prokofiev, J. Blomgren, S. P. Platt, R. Nolte, S. Rottger, and A. N. Smirnov, "Anita—a new neutron facility for accelerated see testing at the svedberg laboratory," in *Reliability Physics Symposium, 2009 IEEE International*, pp. 929–935, IEEE, 2009.

[30] L. K. Mansur, A. Rowcliffe, R. Nanstad, S. Zinkle, W. Corwin, and R. Stoller, "Materials needs for fusion, generation iv fission reactors and spallation neutron sources–similarities and differences," *Journal of Nuclear Materials*, vol. 329, pp. 166–172, 2004.

[31] L. Perkins, B. Logan, M. Rosen, M. Perry, T. D. de la Rubia, N. Ghoniem, T. Ditmire, P. Springer, and S. Wilks, "The investigation of high intensity laser driven micro neutron sources for fusion materials research at high fluence," *Nuclear fusion*, vol. 40, no. 1, p. 1, 2000.

[32] T. Gnäupel-Herold, "Techniques for neutron stress determination with high spatial resolution," *Journal of Nondestructive Evaluation*, vol. 28, no. 3-4, p. 149, 2009.

[33] K. H. Lieser, *Nuclear and radiochemistry: fundamentals and applications*. John Wiley & Sons, 2008.

[34] K. Randle, "The applications of fast neutron activation analysis (fnaa) at birmingham," *Nuclear Instruments and Methods in Physics Research Section B: Beam Interactions with Materials and Atoms*, vol. 24, pp. 1010–1013, 1987.

[35] D. Brune and B. Bivered, "Epithermal neutron activation analysis of elements present in trace quantities in biological materials," *Analytica chimica acta*, vol. 85, no. 2, pp. 411–414, 1976.

[36] J.-L. Ma, C. Carasco, B. Perot, E. Mauerhofer, J. Kettler, and A. Havenith, "Prompt gamma neutron activation analysis of toxic elements in radioactive waste packages," *Applied Radiation and Isotopes*, vol. 70, no. 7, pp. 1261–1263, 2012.

[37] P. Zhang, F. Wittmann, T. Zhao, and E. Lehmann, "Neutron imaging of water penetration into cracked steel reinforced concrete," *Physica B: Condensed Matter*, vol. 405, no. 7, pp. 1866–1871, 2010.

[38] F. De Beer, M. Coetzer, D. Fendeis, and A. D. C. E. Silva, "Neutron radiography and other nde tests of main rotor helicopter blades," *Applied radiation and isotopes*, vol. 61, no. 4, pp. 609–616, 2004.

[39] S. M. Khan, P. A. Polski, C. E. Robbins, B. B. Boubli, R. H. Doney, R. Redman, P. Morvan, T. Gozani, J. Bartko, and D. Syme, "Proceedings of the first international symposium on explosive detection technology," tech. rep., FEDERAL AVIATION ADMINISTRATION TECHNICAL CENTER ATLANTIC CITY NJ, 1992.

[40] T. Gozani, "Novel applications of fast neutron interrogation methods," *Nuclear Instruments and Methods in Physics Research Section A: Accelerators, Spectrometers, Detectors and Associated Equipment*, vol. 353, no. 1-3, pp. 635–640, 1994.

[41] J. Eberhardt, S. Rainey, R. Stevens, B. Sowerby, and J. Tickner, "Fast neutron radiography scanner for the detection of contraband in air cargo containers," *Applied Radiation and Isotopes*, vol. 63, no. 2, pp. 179–188, 2005.

[42] C. E. Moss, M. W. Brener, C. L. Hollas, and W. L. Myers, "Portable active interrogation system," *Nuclear Instruments and Methods in Physics Research Section B: Beam Interactions with Materials and Atoms*, vol. 241, no. 1-4, pp. 793–797, 2005.

[43] D. Norman, J. Jones, W. Yoon, K. Haskell, J. Sterbentz, J. Zabriskie, A. Hunt, F. Harmon, and M. Kinlaw, "Inspection applications with higher electron beam energies," *Nuclear Instruments and Methods in Physics Research Section B: Beam Interactions with Materials and Atoms*, vol. 241, no. 1-4, pp. 787–792, 2005.

[44] J. M. Hall, S. Asztalos, P. Biltoft, J. Church, M.-A. Descalle, T. Luu, D. Manatt, G. Mauger, E. Norman, D. Petersen, *et al.*, "The nuclear car wash: Neutron interrogation of cargo containers to detect hidden snm," *Nuclear Instruments and Methods in Physics Research Section B: Beam Interactions with Materials and Atoms*, vol. 261, no. 1-2, pp. 337–340, 2007.

[45] A. Favalli, H.-C. Mehner, J.-M. Crochemore, and B. Pedersen, "Pulsed neutron facility for research in illicit trafficking and nuclear safeguards," *IEEE transactions on Nuclear Science*, vol. 56, no. 3, pp. 1292–1296, 2009.

[46] G. F. Knoll, *Radiation detection and measurement*. John Wiley & Sons, 2010.

[47] B. Blau, K. Clausen, S. Gvasaliya, M. Janoschek, S. Janssen, L. Keller, B. Roessli, J. Schefer, P. Tregenna-Piggott, W. Wagner, *et al.*, "The swiss spallation neutron source sinq at paul scherrer institut," *0*, 2009.

[48] G. Baldwin and G. Klaiber, "Photo-fission in heavy elements," *Physical Review*, vol. 71, no. 1, p. 3, 1947.

[49] "Fast neutron generator, enea laboratories, frascati." `http://www.fusione.enea.it/LABORATORIES/Tec/FNG.html.en`. Accessed: 15-08-2018.

[50] I. A. E. A. (IAEA), "Development opportunities for small and medium scale accelerator driven neutron sources," *Proceedings of a technical meeting (IAEA-TECDOC–1439)*, 2005.

[51] V. Veksler, "The principle of coherent acceleration of charged particles," *The Soviet Journal of Atomic Energy*, vol. 2, no. 5, pp. 525–528, 1957.

[52] A. Macchi, M. Borghesi, and M. Passoni, "Ion acceleration by superintense laser-plasma interaction," *Reviews of Modern Physics*, vol. 85, no. 2, p. 751, 2013.

[53] L. Cialfi, L. Fedeli, and M. Passoni, "Electron heating in subpicosecond laser interaction with overdense and near-critical plasmas," *Physical Review E*, vol. 94, no. 5, p. 053201, 2016.

[54] C. Perego, A. Zani, D. Batani, and M. Passoni, "Extensive comparison among target normal sheath acceleration theoretical models," *Nuclear Instruments and Methods in Physics Research Section A: Accelerators, Spectrometers, Detectors and Associated Equipment*, vol. 653, no. 1, pp. 89–93, 2011.

[55] A. Henig, S. Steinke, M. Schnürer, T. Sokollik, R. Hörlein, D. Kiefer, D. Jung, J. Schreiber, B. Hegelich, X. Yan, *et al.*, "Radiation-pressure acceleration of ion beams driven by circularly polarized laser pulses," *Physical Review Letters*, vol. 103, no. 24, p. 245003, 2009.

[56] I. J. Kim, K. H. Pae, C. M. Kim, H. T. Kim, J. H. Sung, S. K. Lee, T. J. Yu, I. W. Choi, C.-L. Lee, K. H. Nam, *et al.*, "Transition of proton energy scaling using an ultrathin target irradiated by linearly polarized femtosecond laser pulses," *Physical review letters*, vol. 111, no. 16, p. 165003, 2013.

[57] S. Buffechoux, J. Psikal, M. Nakatsutsumi, L. Romagnani, A. Andreev, K. Zeil, M. Amin, P. Antici, T. Burris-Mog, A. Compant-La-Fontaine, *et al.*, "Hot electrons transverse refluxing in ultraintense laser-solid interactions," *Physical review letters*, vol. 105, no. 1, p. 015005, 2010.

[58] D. Margarone, O. Klimo, I. Kim, J. Prokuupek, J. Limpouch, T. Jeong, T. Mocek, J. Pvsikal, H. Kim, J. Provska, *et al.*, "Laser-driven proton acceleration enhancement by nanostructured foils," *Physical review letters*, vol. 109, no. 23, p. 234801, 2012.

[59] T. Ceccotti, V. Floquet, A. Sgattoni, A. Bigongiari, O. Klimo, M. Raynaud, C. Riconda, A. Heron, F. Baffigi, L. Labate, *et al.*, "Evidence of resonant surface-wave excitation in the relativistic regime through measurements of proton acceleration from grating targets," *Physical review letters*, vol. 111, no. 18, p. 185001, 2013.

[60] J. Bin, W. Ma, H. Wang, M. Streeter, C. Kreuzer, D. Kiefer, M. Yeung, S. Cousens, P. Foster, B. Dromey, *et al.*, "Ion acceleration using relativistic pulse shaping in near-critical-density plasmas," *Physical review letters*, vol. 115, no. 6, p. 064801, 2015.

[61] A. Zani, D. Dellasega, V. Russo, and M. Passoni, "Ultra-low density carbon foams produced by pulsed laser deposition," *Carbon*, vol. 56, pp. 358–365, 2013.

[62] M. Passoni, A. Zani, A. Sgattoni, D. Dellasega, A. Macchi, I. Prencipe, V. Floquet, P. Martin, T. Liseykina, and T. Ceccotti, "Energetic ions at moderate laser intensities using foam-based multi-layered targets," *Plasma Physics and Controlled Fusion*, vol. 56, no. 4, p. 045001, 2014.

[63] J. Davis and G. Petrov, "Angular distribution of neutrons from high-intensity laser–target interactions," *Plasma Physics and Controlled Fusion*, vol. 50, no. 6, p. 065016, 2008.

[64] A. Alejo, A. Green, H. Ahmed, A. Robinson, M. Cerchez, R. Clarke, D. Doria, S. Dorkings, J. Fernandez, P. McKenna, *et al.*, "Numerical study of neutron beam divergence in a beam-fusion scenario employing laser driven ions," *Nuclear Instruments and Methods in Physics Research Section A: Accelerators, Spectrometers, Detectors and Associated Equipment*, vol. 829, pp. 176–180, 2016.

[65] S. Kar, A. Green, H. Ahmed, A. Alejo, A. Robinson, M. Cerchez, R. Clarke, D. Doria, S. Dorkings, J. Fernandez, *et al.*, "Beamed neutron emission driven by laser accelerated light ions," *New Journal of Physics*, vol. 18, no. 5, p. 053002, 2016.

[66] B. Bayanov, V. Belov, V. Kindyuk, E. Oparin, and S. Taskaev, "Lithium neutron producing target for binp accelerator-based neutron source," *Applied Radiation and Isotopes*, vol. 61, no. 5, pp. 817–821, 2004.

[67] S. Halfon, A. Arenshtam, D. Kijel, M. Paul, L. Weissman, D. Berkovits, I. Eliyahu, G. Feinberg, A. Kreisel, I. Mardor, *et al.*, "Demonstration of a high-intensity neutron source based on a liquid-lithium target for accelerator based boron neutron capture therapy," *Applied Radiation and Isotopes*, vol. 106, pp. 57–62, 2015.

[68] C. Willis, J. Lenz, and D. Swenson, "High-power lithium target for accelerator-based bnct," *Proceedings of LINAC08*, pp. 223–225, 2008.

[69] "Lithium fluoride, safety data sheet." `http://www.espimetals.com/index.php/msds/644-lithium-fluoride`. Accessed: 15-08-2018.

[70] G. Randers-Pehrson and D. Brenner, "A practical target system for accelerator-based bnct which may effectively double the dose rate," *Medical physics*, vol. 25, no. 6, pp. 894–896, 1998.

[71] P. Norreys, A. Fews, F. Beg, A. Bell, A. Dangor, P. Lee, M. Nelson, H. Schmidt, M. Tatarakis, and M. Cable, "Neutron production from picosecond laser irradiation of deuterated targets at intensities of," *Plasma physics and controlled fusion*, vol. 40, no. 2, p. 175, 1998.

[72] J. Hah, G. Petrov, J. Nees, Z.-H. He, M. Hammig, K. Krushelnick, and A. Thomas, "High repetition-rate neutron generation by several-mj, 35 fs pulses interacting with free-flowing d2o," *Applied Physics Letters*, vol. 109, no. 14, p. 144102, 2016.

[73] J. Hah, J. Nees, M. Hammig, K. Krushelnick, and A. Thomas, "Characterization of a high repetition-rate laser-driven short-pulsed neutron source," *Plasma Physics and Controlled Fusion*, vol. 60, no. 5, p. 054011, 2018.

[74] "Hercules 300 tw laser." `https://cuos.engin.umich.edu/researchgroups/hfs/facilities/hercules-petawatt-laser/`. Accessed: 15-08-2018.

[75] "The relativistic lambda cubed laser." `https://cuos.engin.umich.edu/researchgroups/hfs/facilities/lambdacubed/`. Accessed: 15-08-2018.

[76] A. Maksimchuk, A. Raymond, F. Yu, G. Petrov, F. Dollar, L. Willingale, C. Zulick, J. Davis, and K. Krushelnick, "Dominant deuteron acceleration with a high-intensity laser for isotope production and neutron generation," *Applied Physics Letters*, vol. 102, no. 19, p. 191117, 2013.

[77] L. Willingale, G. Petrov, A. Maksimchuk, J. Davis, R. Freeman, A. Joglekar, T. Matsuoka, C. Murphy, V. Ovchinnikov, A. Thomas, *et al.*, "Comparison of bulk and pitcher-catcher targets for laser-driven neutron production," *Physics of Plasmas*, vol. 18, no. 8, p. 083106, 2011.

[78] A. Alejo, S. Mirfayzi, S. Kar, M. Borghesi, H. Ahmed, A. Green, *et al.*, "Recent advances in laser-driven neutron sources," *Nuovo Cim.*, vol. 38, p. 188, 2016.

[79] I. Pomerantz, E. Mccary, A. R. Meadows, A. Arefiev, A. C. Bernstein, C. Chester, J. Cortez, M. E. Donovan, G. Dyer, E. W. Gaul, *et al.*, "Ultrashort pulsed neutron source," *Physical review letters*, vol. 113, no. 18, p. 184801, 2014.

[80] M. Roth, D. Jung, K. Falk, N. Guler, O. Deppert, M. Devlin, A. Favalli, J. Fernandez, D. Gautier, M. Geissel, *et al.*, "A bright neutron source driven by relativistic transparency of solids," in *Journal of Physics: Conference Series*, vol. 688, p. 012094, IOP Publishing, 2016.

[81] N. Guler, P. Volegov, A. Favalli, F. E. Merrill, K. Falk, D. Jung, J. L. Tybo, C. H. Wilde, S. Croft, C. Danly, *et al.*, "Neutron imaging with the short-pulse laser driven neutron source at the trident laser facility," *Journal of Applied Physics*, vol. 120, no. 15, p. 154901, 2016.

[82] J. Yang, P. McKenna, K. Ledingham, T. McCanny, L. Robson, S. Shimizu, R. Singhal, M. Wei, K. Krushelnick, R. Clarke, *et al.*, "Neutron production by fast protons from ultraintense laser-plasma interactions," *Journal of applied physics*, vol. 96, no. 11, pp. 6912–6918, 2004.

[83] T. Žagar, J. Galy, J. Magill, and M. Kellett, "Laser-generated nanosecond pulsed neutron sources: scaling from vulcan to table-top," *New Journal of Physics*, vol. 7, no. 1, p. 253, 2005.

[84] P. McKenna, K. Ledingham, S. Shimizu, J. Yang, L. Robson, T. McCanny, J. Galy, J. Magill, R. Clarke, D. Neely, *et al.*, "Broad energy spectrum of laser-accelerated protons for spallation-related physics," *Physical review letters*, vol. 94, no. 8, p. 084801, 2005.

[85] D. Gupta and H. Suk, "Energetic electron beam generation by laser-plasma interaction and its application for neutron production," *Journal of applied physics*, vol. 101, no. 11, p. 114908, 2007.

[86] X. Jiao, J. Shaw, T. Wang, X. Wang, H. Tsai, P. Poth, I. Pomerantz, L. Labun, T. Toncian, M. Downer, *et al.*, "A tabletop, ultrashort pulse photoneutron source driven by electrons from laser wakefield acceleration," *Matter and Radiation at Extremes*, vol. 2, no. 6, pp. 296–302, 2017.

[87] G. Petrov, L. Willingale, J. Davis, T. Petrova, A. Maksimchuk, and K. Krushelnick, "The impact of contaminants on laser-driven light ion acceleration," *Physics of Plasmas*, vol. 17, no. 10, p. 103111, 2010.

[88] S. Kisyov, S. Lalkovski, D. Ivanova, N. Mărginean, D. Bucurescu, G. Căta-Danil, I. Căta-Danil, D. Deleanu, D. Ghiţă, T. Glodariu, *et al.*, "Structure of low-lying positive-parity states in 99, 101, 103 ru from in-beam fast-timing measurements.," *Bulgarian Journal of Physics*, vol. 42, no. 4, 2015.

[89] S. Mirfayzi, A. Alejo, H. Ahmed, D. Raspino, S. Ansell, L. Wilson, C. Armstrong, N. Butler, R. Clarke, A. Higginson, *et al.*, "Experimental demonstration of a compact epithermal neutron source based on a high power laser," *Applied Physics Letters*, vol. 111, no. 4, p. 044101, 2017.

[90] C. Toupin, E. Lefebvre, and G. Bonnaud, "Neutron emission from a deuterated solid target irradiated by an ultraintense laser pulse," *Physics of Plasmas*, vol. 8, no. 3, pp. 1011–1021, 2001.

[91] G. Petrov, D. Higginson, J. Davis, T. B. Petrova, J. McNaney, C. McGuffey, B. Qiao, and F. Beg, "Generation of high-energy ($>$ 15 mev) neutrons using short pulse high intensity lasers," *Physics of Plasmas*, vol. 19, no. 9, p. 093106, 2012.

[92] S. Agostinelli, J. Allison, K. a. Amako, J. Apostolakis, H. Araujo, P. Arce, M. Asai, D. Axen, S. Banerjee, G. . Barrand, *et al.*, "Geant4-a simulation toolkit," *Nuclear instruments and methods in physics research section A: Accelerators, Spectrometers, Detectors and Associated Equipment*, vol. 506, no. 3, pp. 250–303, 2003.

[93] G. Collaboration, "Geant4 user's guide for application developers," *Accessible from the GEANT4 web page [1] Version geant4*, vol. 9, 2012.

[94] G. Collaboration *et al.*, "Physics reference manual," *Version: geant4*, vol. 10, no. 9, 2016.

[95] S. Agostinelli, J. Allison, K. a. Amako, J. Apostolakis, H. Araujo, P. Arce, M. Asai, D. Axen, S. Banerjee, G. . Barrand, *et al.*, "Geant4—a simulation toolkit," *Nuclear instruments and methods in physics research section A: Accelerators, Spectrometers, Detectors and Associated Equipment*, vol. 506, no. 3, pp. 250–303, 2003.

[96] "The relativistic lambda cubed laser." `https://www-nds.iaea.org/exfor/endf.html`. Accessed: 23-08-2018.

[97] "The relativistic lambda cubed laser." `http://www.talys.eu/home/`. Accessed: 23-08-2018.

[98] K. Lancaster, S. Karsch, H. Habara, F. Beg, E. Clark, R. Freeman, M. Key, J. King, R. Kodama, K. Krushelnick, *et al.*, "Characterization of 7 li (p, n) 7 be neutron yields from laser produced ion beams for fast neutron radiography," in *Physics of plasmas*, vol. 11, pp. 3404–3408, AIP, 2004.